Integrated Photonic Studies of Silicon Meandering Distributed Feedback Structures: A Model System for Biological Ligands

by

Muhammad Rehan Chaudhry

A Dissertation Submitted to the
Graduate School of Science and Engineering
in Partial Fulfillment of the Requirements for
the Degree of
Doctor of Philosophy
in
Biomedical Sciences and Engineering

KOÇ
UNIVERSITY

September 2019

Koç University

Graduate School of Sciences and Engineering

This is to certify that I have examined this copy of a doctoral dissertation by

Muhammad Rehan Chaudhry

and have found that it is complete and satisfactory in all respects,

and that any and all revisions required by the final

examining committee has been made.

Committee Members:

Prof. Dr. Ali Serpengüzel (Advisor)

Prof. Dr. Özgür Müstecaplıoğlu

Assoc. Prof. Dr. Erdem Alaca

Prof. Dr. Arda Deniz Yalçınkaya

Assoc. Prof. Dr. Ahmet Öncü

Date: 05-09-2019

ABSTRACT

Integrated photonics structures such as ring resonators, distributed Bragg reflectors (DBRs), Mach-Zehnder interferometers (MZIs), as well as their cascaded versions have been extensively studied and successfully tested for the biosensing of samples such as viruses, protein biomarkers, deoxyribonucleic acid (DNA), and microribonucleic acid (microRNA). We propose novel silicon-on-insulator (SOI) meandering distributed feedback (MDFB), antisymmetric MDFB (AMDFB), and symmetric MDFB (SMDFB) structures for biosensing applications. A single transverse electrically (TE) polarized silicon waveguide is used to design these monolithic structures in contrast with ring resonators, where a bus waveguide is necessary to couple with the rings. The base structure is a meandering loop mirror (MLM). Three identical MLMs are serially connected to form an MDFB structure, which shows spectral mode splitting in its spectral response. The AMDFB structure has four interlaced identical MLMs. AMDFB spectra shows spectral mode splitting at a coupling constant of $C = 0.09$ and electromagnetic induced transparency (EIT)-like peaks from $0.27 < C < 0.51$. The SMDFB structure has five interlaced identical MLMs. SMDFB spectra shows spectral mode splitting with Fano resonance, when $C = 0.24$; and EIT-like peaks, when $0.78 < C < 0.94$. The SMDFB structure's experimental spectrum with Fano lineshape shows an extinction ratio of 26 dBm and a slope ratio of 368 dBm/nm. The intrinsic limit of detection of a resonant sensor can be expressed as λ/QS, where λ is the free space wavelength, Q is the Q-factor of the

resonator, and S is the sensitivity. The spectrally split peaks of MDFB structures, and the EIT-like peaks in AMDFB and SMDFB structures show Q-factors on the order of 50000; so that at λ = 1550 nm, and S = 50 nm/RIU the theoretical intrinsic limit of our silicon photonic structures is on the order of 0.0006 [RIU], without taking into consideration the biomolecule absorption at 1550 nm. In addition to the existing integrated photonics structures, our novel monolithic SOI based photonic structures show promise for biosensing applications.

ÖZET

Halka çınlaçları, dağıtılmış Bragg yansıtıcıları (DBY), Mach-Zehnder girişimölçerleri (MZG) ile bunların ardışık bağlanmış sürümleri gibi tümleşik fotonik yapılar virüs, protein, biyoimleyici, deoksiribonükleik asit (DNA), ve mikroribonükleik asit (mikroRNA) gibi örneklerin biyoalgılanması yaygın olarak çalışılmış, ve başarıyla denenmiştir. Biz biyoalgılama uygulamaları için yeni bir tür yalıtkan-üzeri-silisyum (YÜS) kıvrımlı dağıtılmış geribildirim (KDG), antisimetrik KDG (AKDG), ile simetrik KDG (SKDG) yapılarını öneriyoruz. Bağdaşmak için taşıyıcı dalgakılavuzu gerektiren halka çınlaçlarının tersine, bu tektaş yapıları tasarlamak için bir enine elektrik (EE) kutuplu silisyum dalgakılavuzu kullanılmıştır. Bu tasarımların yapıtaşı kıvrımlı halka yansıtıcıdır (KHY). İzgesel kip ayrımı gösteren, KDG yapısını oluşturmak için 3 tane KHY ardışık olarak kullanılmıştır. AKDG yapısı için 4 tane içiçe geçmiş KHY kullanılmıştır. AKDG yapısı izgesinde, $C = 0.09$ bağlaşım katsayısı için izgesel kip ayrımı; $0.27 < C < 0.51$ için elektromanyetik irkiltilmiş saydamlık (EIS)-benzeri tepeler görülmüştür. SKDG yapısı 5 tane içiçe geçmiş KHY kullanılmıştır. SKDG izgesi, $C = 0.24$ için kip ayrımlı Fano çınlaması; $0.78 < C < 0.94$ için elektromanyetik irkiltilmiş saydamlık (EIS)-benzeri tepeler gösterir. SKDG yapısının Fano çizgibiçimli deneysel izgesi 26 dBm sönümleme oranı ve 368 dBm/nm eğim oranı gösterir. Bir çınlaç algılayıcının öz algılama sınırı λ/QS olarak gösterilebilir; burada λ boş uzay dalgaboyu, Q çınlacın nitelik katsayısı, S duyarlılıktır. KDG yapısının izgesel ayrılmış tepeleri ile, AKDG, ve SKDG yapılarının elektromanyetik irkiltilmiş saydamlık (EIS)-benzeri tepeleri $Q = 50000$

düzeyinde nitelik katsayısı gösterir; öyle ki 1550 nm dalgaboyundaki biyomolekül soğurması katılmadığında, λ = 1550 nm dalgaboyunda, S = 50 nm/RIU duyarlılık değerinde, silisyum fotonik yapılarımızın kuramsal öz sınırı 0.0006 [RIU] olarak bulunur. Var olan tümleşik fotonik devre yapılarına ek olarak, bizim sunduğumuz yeni tektaş yalıtkan-üzeri-silisyum (YÜS) fotonik yapılar biyoalgılama uygulamalarında ümit vermektedir.

ACKNOWLEDGEMENTS

I would like to express my gratitude to my supervisor, Prof. Dr. Ali Serpengüzel for providing me opportunity to begin research in his group at Koç University Microphotonics Research Laboratory (KUMRL) and for his constant guidance, understanding, and patience during my PhD degree study in Koç University. I would also like to thank my committee members Prof. Dr. Özgür Müstecaplıoğlu and Assoc. Prof. Dr. Erdem Alaca for their reading of my thesis, and their constructive comments. I would like to thank my external committee members Prof. Dr. Arda Deniz Yalçınkaya and Assoc. Prof. Dr. Ahmet Öncü for reviewing this thesis.

I would also like to thank research group members, namely Dr. Ulaş Sabahattin Gökay, Syed Sultan Shah Bukhari, Dr. Muhammad Zakwan, Mustafa Mert Bayer, Nurperi Yavuz, Suat Kurt, and Hakkı Burak Pekin for their help in brainstorming sessions and moral boosting. I am also thankful to Farhan Azeem for reviewing and suggesting positive changes in this thesis.

I would also like to acknowledge Prof. Dr. Lukas Chrostowski and Hossam Shoman of University of British Columbia, Richard Bojko at the University of Washington, and Cameron Horvath at Applied Nanotools Inc. for their valuable contributions in the education, training, manufacturing, and measurement of the integrated photonic structures.

I would also like to thank the Society of Photooptical Instrumentation Engineers (SPIE). And finally, I would thank Pakistan Higher Education Commission (HEC) for all the financial support, which made this study a reality.

To my parents

Table of Contents

List of Tables

List of Figures

NOMENCLATURE

c	Speed of light in vacuum
C	Coupling constant
k	Propagation vector
R	Radius
λ	Wavelength of light in vacuum
n_{eff}	Effective index
n_g	Group index
β	Propagation constant
α	Propagation loss
E	Electric field
H	Magnetic field
D	Electric displacement
B	Magnetic induction
κ	Cross-coupling constant
t	Self-coupling constant
Q	Quality factor
LOD	Limit of detection
S	Sensitivity
$\Delta\lambda_{3dB}$	Full-width half maximum
m	Mode number
$\Delta\lambda$	Free spectral range

Chapter 1 Introduction

1.1 Integrated Photonics in Biomedical Sensing

Timely diagnostic results are very crucial for the progress in healthcare. The diagnostic tests performed on the human body fluids mainly blood and urine, are termed as in-vitro diagnostics (IVDs). Such IVDs involve sample to be taken from the patient body and analyzed with expensive equipment at state-of-the-art examination centers or hospitals by highly trained staff, which involves consumption of many hours of time and involve high costs. Point-of-care (POC) diagnostics, which are sub-category of IVDs, can be performed anywhere at patients home or at hospital, save time, lower financial costs and produce early results. POC diagnostics can be done with both small handheld portable and usual large devices. The POC diagnostic tests are normally done for glucose monitoring, pregnancy test, and also for fatal diseases, as HIV. The global market share of rapid POC testing is expected to increase by 9 billion USD during 2019-2023 [1]. By improvements in POC diagnostics, the complete ecosystem of health care facility will improve. The performance of POCTs is still similar to laboratory- based diagnostics as POCTs are optimized to be handled easily and produce fast results. There is lot of work going on to increase the performance of POCTs.

Integrated photonics has shown lot of growth in the last decade, especially silicon photonics. The silicon-on-insulator (SOI) technology is compatibility with already established complementary metal-oxide semiconductor (CMOS) facility, which

allows the reduction of fabrication cost and makes silicon photonics structures good candidate for POC. Currently, most of the silicon photonics biosensors are based on disk and ring resonators. The motivation behind my research is to design, simulate, and analyze novel silicon photonic structures, with high quality factors to be used as biosensors.

1.1.1 Biosensors

The field of biosensors has been showing growth with more than 22000 research articles published in last five years as shown in figure 1.1. Biosensors are an essential part of diagnostics setup. Biosensors can sense the attachment of specific biomolecule and can give information about its presence or of perturbation in the surroundings by change in the output signal. Biosensors can have different output signals in the form of fluorescence, color change, or electric signal.

The earliest research ideas of practical biosensors, using electrodes to monitor blood oxygen tension was published in 1956, [2] and electro-mechanical sensing system comprising of electrodes for continuous monitoring of glucose was published in 1962, [3] which laid the foundations for modern biosensing platforms. With progress in biosensors due to improvement in manufacturing techniques, diagnostics, such as glucose sensing, have a growing market of more than USD 13 billion per year [4].

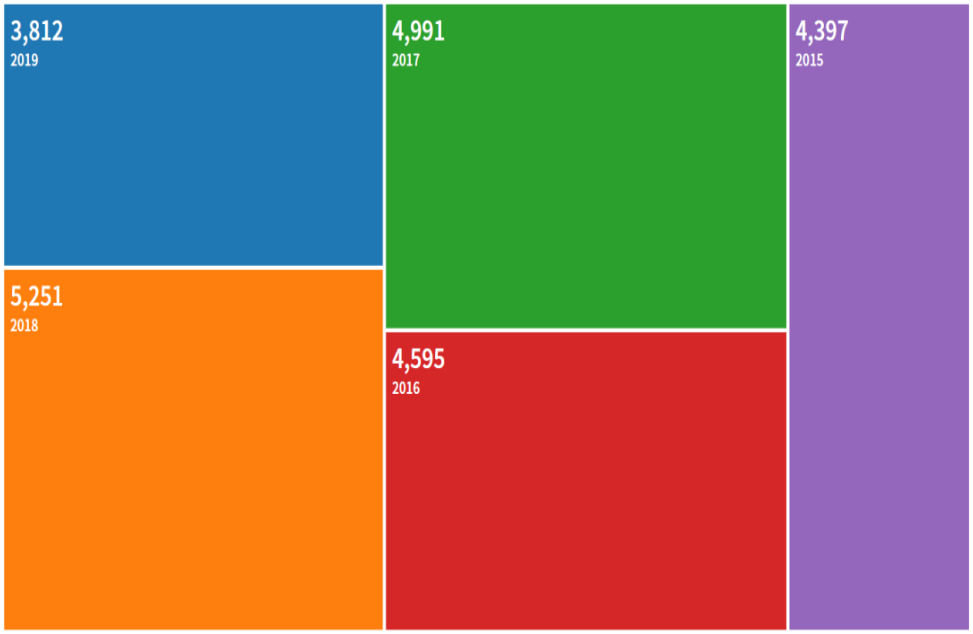

Figure 1-1 Tree map of research articles count per year against keyword "biosensor" for last five years from web of science.

Biosensors are generally categorized into two categories: (a) label-based biosensors, and (b) label-free biosensors. Label-based biosensors have an additional molecule, which is chemically or temporarily attached to the target. Most common labeling methods are fluorescent, molecular, and enzyme labeling; and can achieve very low detection limits [5]. Label-free biosensors use the properties of the biomolecule, e.g., sensing the change in refractive index (RI), or molecular weight; and send an output signal.

1.2 Silicon Photonics

Photonic integrated circuits (PICs) are gathering strong interest, as they are low cost, low power, compact, and high-volume is possible due to the compatibility with already matured complementary metal oxide semiconductor (CMOS) manufacturing

foundries [6-7], and its ability to integrate large number of photonic integrated circuits (PICs) on single chip for applications ranging from telecommunication [8] to medicine, and life sciences [9]. Due to the improvement in fabrication facilities, low-loss waveguides [10] and uniform structures on silicon-on-insulator (SOI) is now possible, which led to the fabrication of microresonators, with low insertion loss, and of different types such as microrings [11-12], microdisks [13], as well as Bragg grating, [14] and photonic crystal [15] based resonators.

These photonic structures exhibit resonances with Lorentzian [16-17] and Fano lineshapes [18-19]. Fano lineshape is preferred due to the low switching power and higher extinction ratio (ER), when compared with the Lorentzian lineshape [20]. The Fano lineshape is generated, when a resonance is not in phase (Lorentzian), nor out of phase (inverse Lorentzian) with a background signal [21-22]. The split of the Fano lineshape resonances is due to the lifting of the degeneracy, due to the mutual coupling of these Fano lineshape resonances. The electromagnetically induced transparency (EIT)-like lineshape is generated, when two degenerate resonances are coupled to each other, resulting in maximum transparency for ring resonators, [23] and meandering waveguides.

Electromagnetic induced transparency (EIT) phenomenon has gained lot of interest due to its potential applications in slow and fast light propagation [24], optical filtering [25], quantum computing applications [26], quantum information processing [27], high-sensitivity biochemical sensing [28], and non-linear optics [29]. EIT is an atomic phenomenon [30], which occurs due to quantum level interactions of light with

atoms and as a result light passes through the medium rather being absorbed by the atoms [31-32]. EIT-like phenomenon can also occur in photonic resonator structures due to coherent interference of the coupled resonators [33]. Various photonic structures have demonstrated classical all-optical analogies to EIT-like spectral behavior, i.e., microrings setup with coherent interference between two indirectly coupled microring resonators [34], whispering-gallery mode (WGM) resonators [35-36], photonic crystal waveguides and microcavities [37-38], as well as plasmonic structures and metamaterials [39-40]. Conventional resonances of regular ring and disk resonators result in Lorentzian lineshapes [41-42]. Novel photonic structures are needed to achieve Fano lineshapes [43] and the EIT-like spectral responses [44]. EIT-like spectral responses are also studied in conventional photonic structures [45] for applications in and slow light propagation [46].

Meandering waveguide (MW) resonators offer Lorentzian lineshapes by connecting two meandering loop mirrors (MLMs) through a silicon waveguide [47]. MW offers diversity in a sense that, resonators can be designed by coupling or connecting MW structures together. Self-coupled optical waveguide (SCOW) resonators have been realized by connecting two MW structures exhibiting EIT-like phenomenon [48]. Distributed MW (DMW) active devices with four coupling points have been presented with a focus on EIT-like phenomenon [49].

1.2.1 Silicon Photonics Biosensors

Silicon photonic structures are designed to operate in near-infrared region. The light is coupled to the silicon nanowires, named as waveguides, through optical fibers using

grating couplers (GCs) or side coupling. The coupled light is not concentrated in the center of waveguide and some percentage of light's electric field travels outside the waveguide, which is termed as evanescent field. When a biomolecule is attached to the waveguide, evanescent wave senses the change in refractive index of the environment, which shifts the resonance wavelength of the resonator. There are number of figure of merits (FOMs) related to performance of biosensor.

1.2.1.1 Figure of merits (FOMs)

1.2.1.1.1 Sensitivity

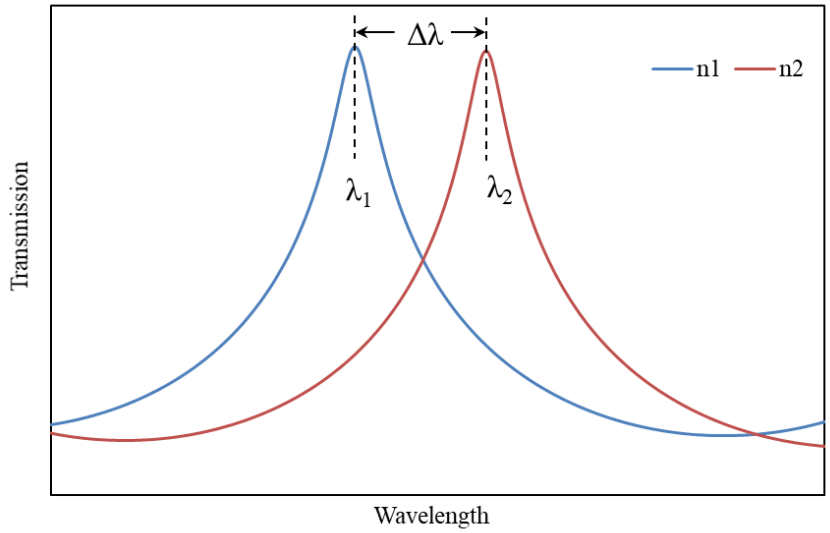

Figure 1-2 The shift in the resonance wavelength of the resonant structure with the change in the refractive index of cladding.

Sensitivity of silicon photonics resonant structure is defined as the shift in the resonance wavelength with the change in refractive index and is given by:

$$S = \frac{\Delta\lambda}{\Delta n} \quad (1\text{-}1),$$

where $\Delta\lambda$ is the shift in the resonator resonance wavelength, and Δn the change in refractive index. The resonant structure sensitivity can be measured by considering the change in the refractive index of entire cladding termed as bulk sensing, or by measuring the change in the refractive index due to change in the thickness of biomolecule layer termed as surface sensing.

1.2.1.2 Quality Factor

Quality factor (Q-factor) of resonant structure gives information about the photon lifetime and can be approximated as:

$$Q \approx \frac{\lambda}{\Delta\lambda_{3dB}} \quad (1\text{-}2),$$

where λ is the resonance wavelength, and $\Delta\lambda_{3dB}$ the full-width half maximum (FWHM). Higher Q-factors are required for better limit of detection (LOD) of the sensor.

1.2.1.3 Limit of Detection

Limit of detection (LOD) of sensor is defined as the minimum perturbation (e.g., change in refractive index) in the surroundings to cause a wavelength shift in the spectral response, that can be measured by the detecting instrumentation. Integrated photonics resonator LOD can be expressed in /RIU as [50-51]:

$$LOD = \frac{\lambda}{Q.S} \quad (1\text{-}3),$$

where λ is the resonance wavelength of resonator, Q the quality-factor of resonator, and S the sensitivity of resonator.

1.3 Silicon Photonics Structures as Biosensors

In the MZI structure, the input light is divided in a 50:50 ratio to travel along two paths, and is then combined at the output. The MZI with this configuration is called a balanced MZI (BMZI), as shown in Figure 1.3(a). If there is difference in lengths of the two paths ΔL, then the MZI is called as an unbalanced MZI (UMZI). BMZI is used as sensor as one of the arm remains clad, and at the other arm the cladding is removed, for a biomolecule layer to be detected, to be attached. This attachment of biomolecule layer changes the effective index n_{eff} of the sensing waveguide, and causes a change in the optical path length, due to which constructive or destructive interference is observed in the spectral response. A POC system with TE polarized MZI structures to detect multiplexed micro-RNAs in human urine sample has been demonstrated with a sensitivity of < 1fmol / μL [52]. Ring or disk resonators are most popular silicon photonics structures. Schematics of single bus, double bus ring, and racetrack resonators are shown in Figure 1.4. Incident light travels through the waveguide, and is coupled to the ring or disk through evanescent coupling. The resonant condition of the ring resonator can be expressed as:

$$\lambda = \frac{2\pi R n_{eff}}{m} \quad (1\text{-}4),$$

where λ is the resonant wavelength, R the radius of the ring or disk, n_{eff} the effective index of ring or disk, and m the integer mode order. The ring resonator-based biosensor has been demonstrated with a bulk sensitivity of 57 nm/RIU and 222 nm /RIU for TE and TM polarization, respectively [53].

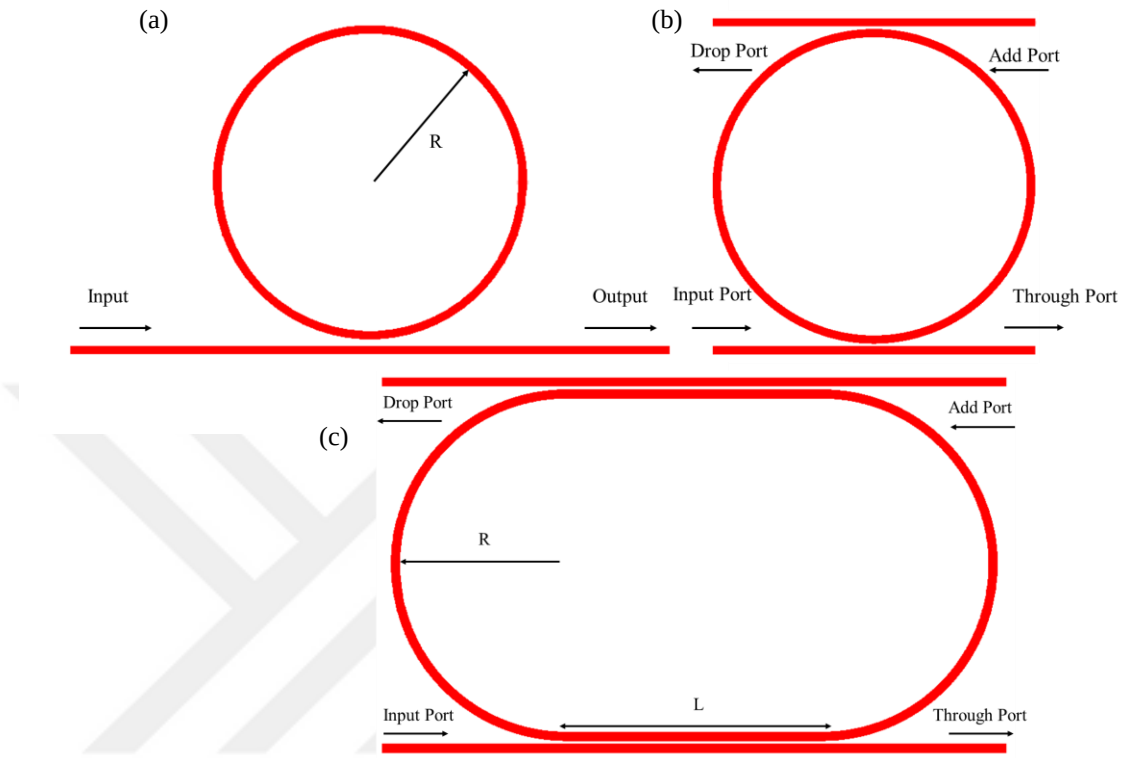

Figure 1-3 Schematic of (a) single, (b) double bus ring, and (c) racetrack resonator.

The racetrack resonator with Si waveguide dimensions of 500 nm x 220 nm has also demonstrated bulk sensitivity of 70 nm/RIU and detection limit of 10^{-5} RIU [54]. We can observe that, the resonators designed for TM polarization shows higher sensitivity than the TE polarized ring resonator.

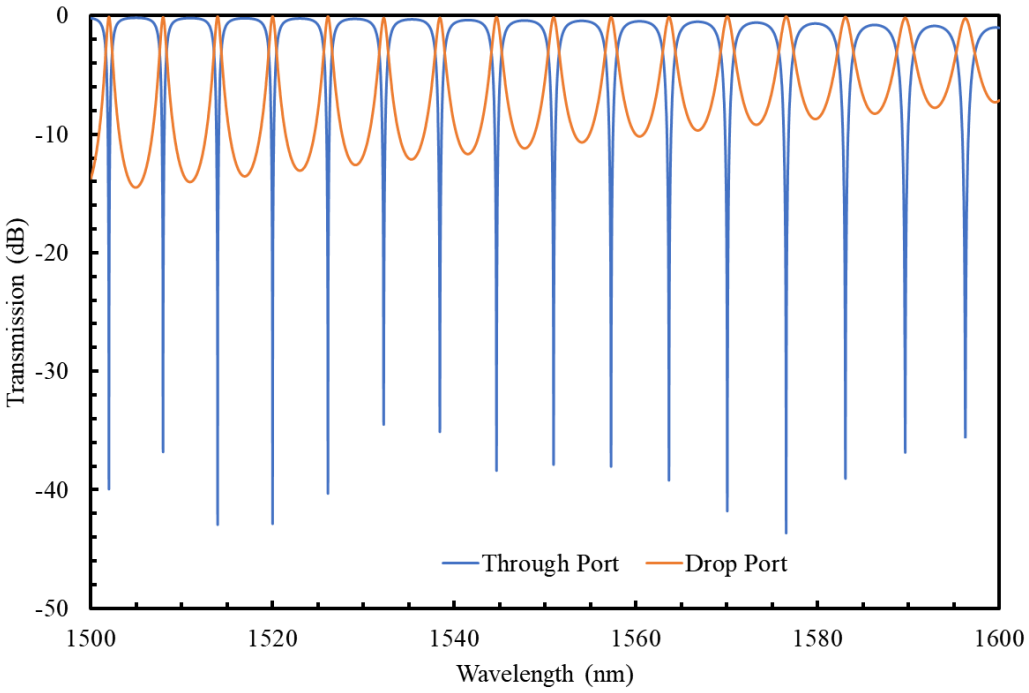

Figure 1-4 Simulated spectral response of racetrack resonator through and add port with radius of curvature R = 10 µm, and coupling length L = 15 µm.

Different approaches are also investigated to improve sensitivity and detection limit. Porous silicon ring resonator with a radius of 10 µm and dimensions of 1200 nm width and 600 nm height has demonstrated a Q-factor of 10000, bulk sensitivity of 380 nm/RIU [55]. Racetrack resonator having footprint of 13 µm x 10 µm designed for TE polarized slot waveguides with a slot region of 100 nm has demonstrated a bulk sensitivity of 298 nm/RIU and a detection limit of 4.2×10^{-5} [56]. Thin racetrack resonators with a waveguide height of 150 nm and a radius of 40 µm designed for TM polarization have demonstrated a bulk sensitivity of 270 nm/RIU, a Q-factor of 4500, and a detection limit of 1.2×10^{-3} RIU [57]. Ring resonators designed with subwavelength gratings have also been studied and demonstrate a bulk sensitivity of 490 nm/RIU, a Q-factor of 7000, and a detection limit of 2×10^{-6} RIU for a ring

diameter of 30 μm [58]. Ring and disk resonators are extensively used in integrated photonics. The motivation behind this thesis is to design, simulate, fabricate, and analyze novel integrated photonics structures with primary application as biosensors.

1.4 Thesis Structure

Thesis is divided into five chapters. The first chapter is comprised of an introduction about the general biosensors and integrated photonics biosensors available in the literature. Chapter 2 gives us insight on design techniques, basic components as waveguides, and directional couplers. The fabrication process and the experimental setup are also discussed in brief. Chapter 3 tells about the base structure meandering loop mirror (MLM), and how we can combine different MLMs to design different photonic structures. We have discussed MLM, antisymmetric meandering resonator (AMR), symmetric meandering resonator (SMR) structures in brief, and meandering resonator (MR), meandering distributed feedback (MDFB), antisymmetric MDFB (AMDFB), and symmetric MDFB (SMDFB) structures in detail. Different spectral shapes such as Lorentzian lineshapes, mode splitting, EIT-like, and Fano lineshapes are observed with Q-factors on the order of 50000, and high extinction ratios (ERs). Chapter 4 is on the study of silicon meandering distributed feedback structures as a model system for biological ligands. Chapter 5 concludes the thesis and gives some information regarding the future work.

Chapter 2 Design, Simulation, Manufacturing, and Measurement

2.1 Design

Waveguides are the used to guide light through the integrated photonics lightwave circuits. There are different types of waveguides available in the literature, to design photonic structures. Figure 2.1 shows different waveguide types, i.e., (a) ridge, (b) strip, (c) slot, and (d) sub-wavelength grating (SWG) waveguides.

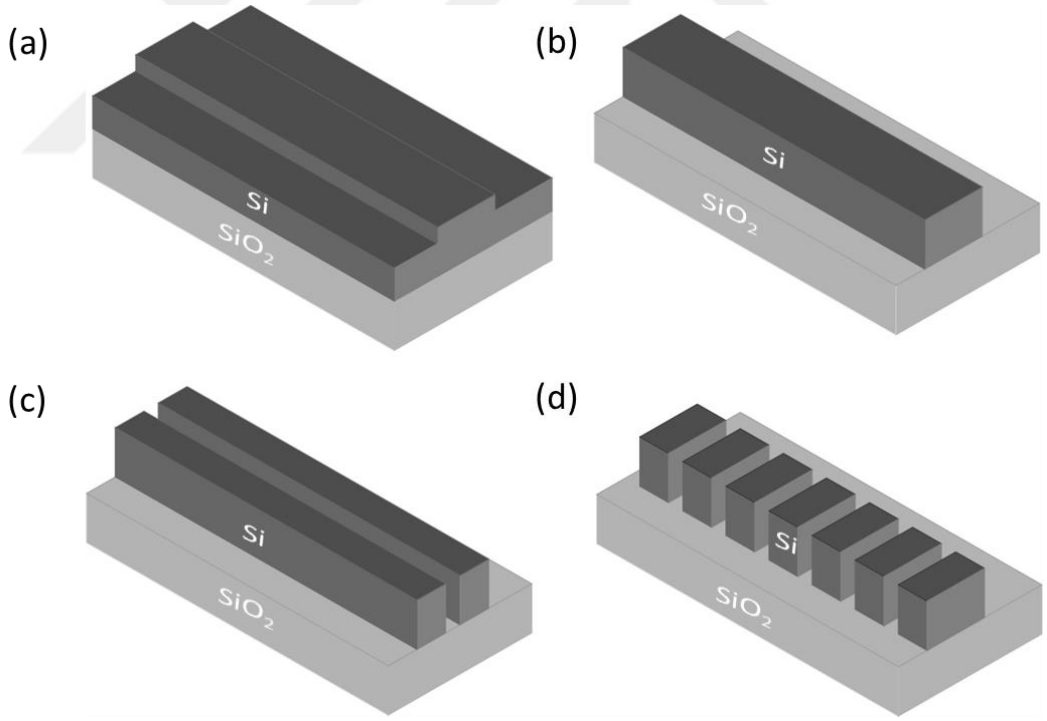

Figure 2-1 (a) ridge, (b) strip, (c) slot, and (d) sub-wavelength grating (SWG) waveguides.

We have designed our structures for SOI technology, as shown in Figure 2.2. The basic design components of our structures are silicon straight waveguides, bent waveguides, and coupling regions. For the design and simulation of the integrated silicon structures, we used photonic software package Mode (Lumerical Solutions Inc.) for optimizing the straight and bend waveguide parameters, FDTD (Lumerical Solutions Inc.) to obtain the s-parameters of the straight waveguide, bent waveguides, and directional couplers. The individual components' s-parameters are then imported, and assembled in Interconnect (Lumerical Solutions Inc.) to observe the response of the complete structure, and obtain the transmission spectra. The optimized structures are then transferred to a layout package (KLayout) for control of the semiconductor processing equipment.

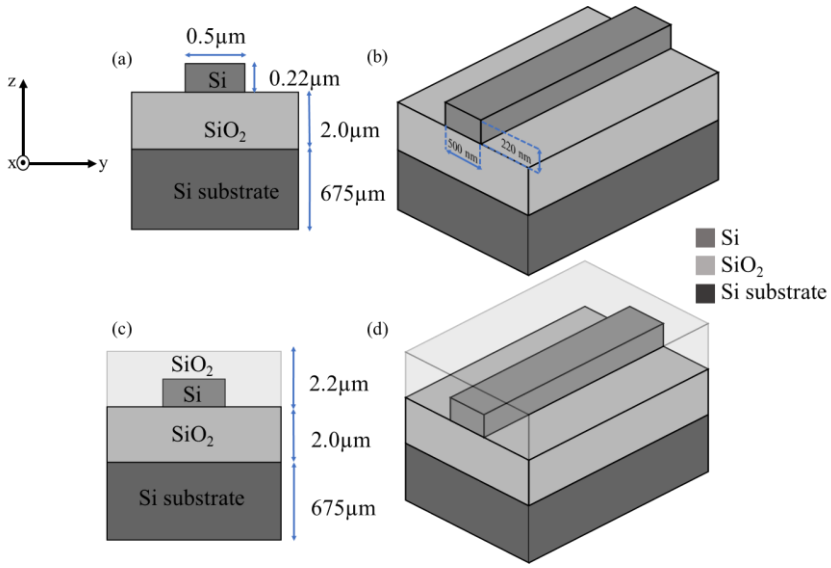

Figure 2-2(a) cross-sectional, (b)lateral , (c) cross-sectional after oxidation and (d) lateral after oxidation, schematic of SOI waveguide.

For the design and simulation of the integrated silicon structures, we used photonic software package Mode (Lumerical Solutions Inc.) for optimizing the straight and bend waveguide parameters, FDTD (Lumerical Solutions Inc.) to obtain the s-parameters of the straight waveguide, bend waveguides, and directional couplers. The individual components s-parameters are then imported, and assembled in Interconnect (Lumerical Solutions Inc.) to observe the response of the complete structure, and obtain the transmission spectra. The optimized structures are then transferred to a layout package (KLayout) for control of the semiconductor processing equipment.

2.1.1 Silicon Waveguides

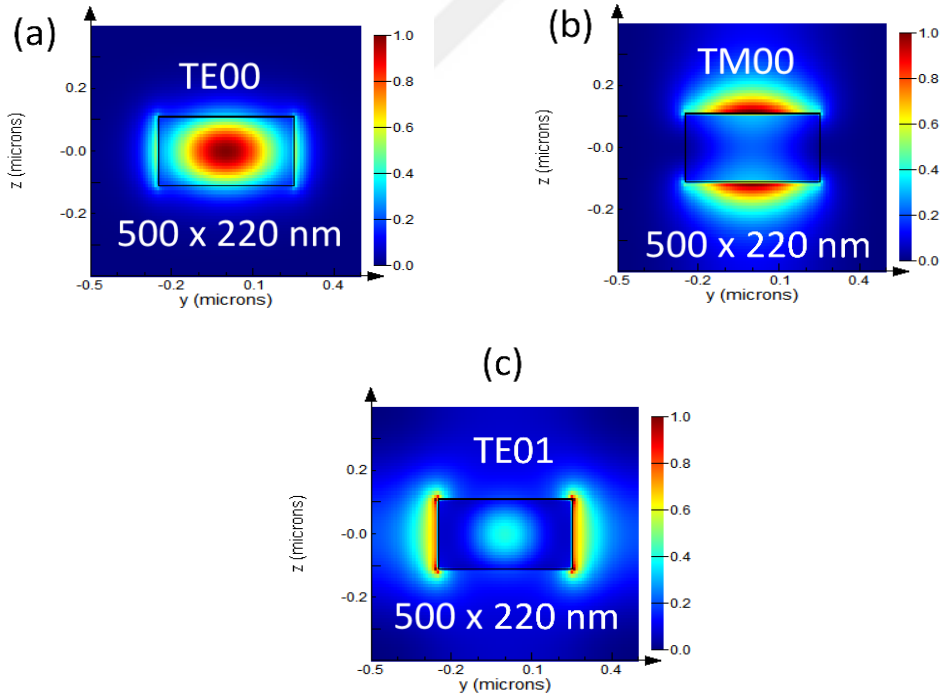

Figure 2-3 (a) TE_{00}, (b) TM_{00}, and (c) TE_{01} mode profiles of 500 nm x 220 nm silicon waveguide.

We have used channel silicon waveguides with dimensions of 500 nm x 220 nm in all our designs, as shown in Figure 2.2. Rib waveguides are mostly used to design active

devices and have a slab height of 90 to 120 nm along the silicon waveguide core to the end of the oxide layer. The mode profiles of three modes supported by silicon waveguide with dimensions of 500 nm x 220 nm are shown in Figure 2.3.

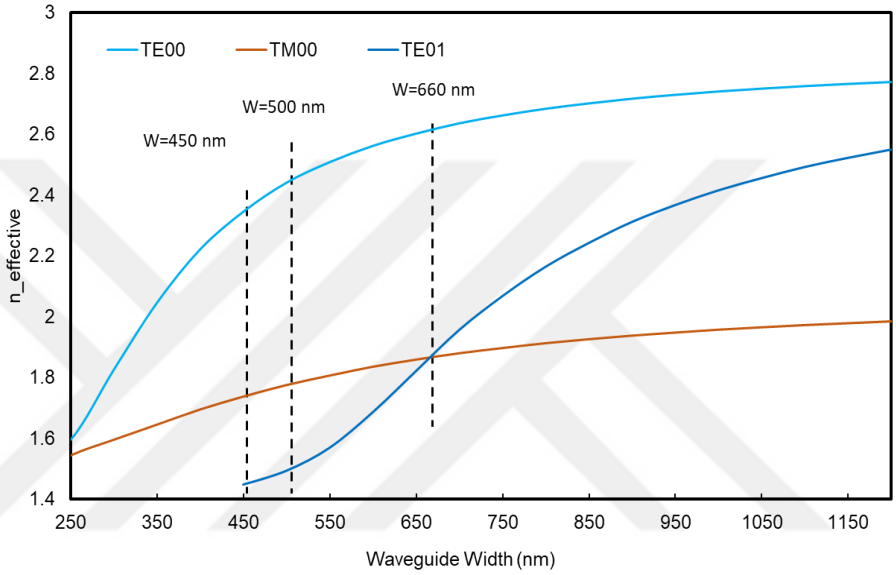

Figure 2-4 Effective index of TE_{00}, TE_{01}, and TM_{00} mode at Si waveguide with fixed height of 220 nm and different widths at 1550 nm.

The silicon waveguide effective index with a height of 220 nm and different widths is plotted in Figure 2.4. We can observe waveguide supports single TE mode till a width of 450 nm, and the waveguide is not strictly single mode at a width of 500 nm and the mode is therefore called quasi-TE mode. For sensing applications, the top oxide cladding is removed and the silicon waveguide is exposed for a biomolecule layer to be detected. The silicon waveguide for bulk and surface sensing is shown in Figure 2.5 and 2.6, respectively.

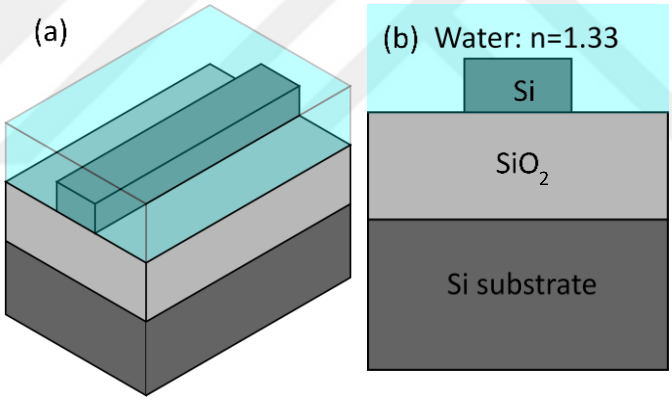

Figure 2-5 (a) Lateral and (b) cross-sectional schematic of bulk sensing geometry.

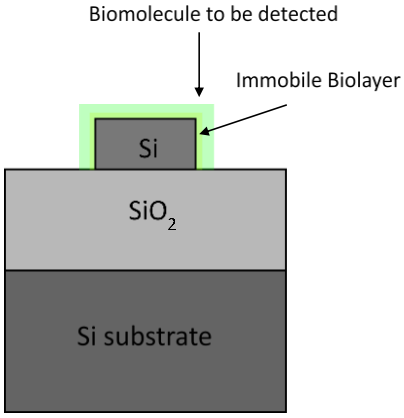

Figure 2-6 Cross-sectional schematic of surface sensing geometry.

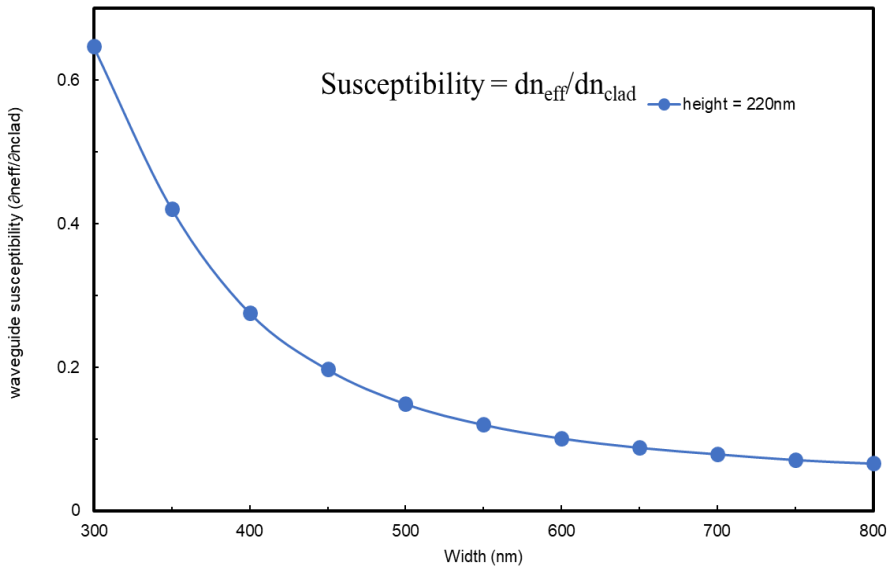

Figure 2-7 Silicon waveguide susceptibility for the quasi-TE mode with a height = 220nm and different widths.

The bulk sensitivity of the waveguide can be written as $(\frac{\partial n_{eff}}{\partial n_{clad}})$, i.e., the change in effective index w.r.t the change in the cladding index; and the surface sensitivity can be expressed as $(\frac{\partial n_{eff}}{\partial d})$ i.e., the change in effective index w.r.t the change in the layer thickness [59]. The silicon waveguide bulk susceptibility for the TE mode is plotted in Figure 2.7 using Lumerical Mode package. The waveguide height is fixed at 220 nm and the width is varied from 300 nm to 800 nm. The waveguide susceptibility decreases with the increase in width at h = 220 nm. Similarly, the bulk susceptibility of the Si waveguide for TM mode is plotted in Figure 2.8 with h = 220nm and width

varied from 300 to 600 nm. The susceptibility value for TM mode is higher than the one for the TE mode. The simulated Si waveguide response is plotted in Figure 2.9, which shows a propagation loss of -3 dB/cm.

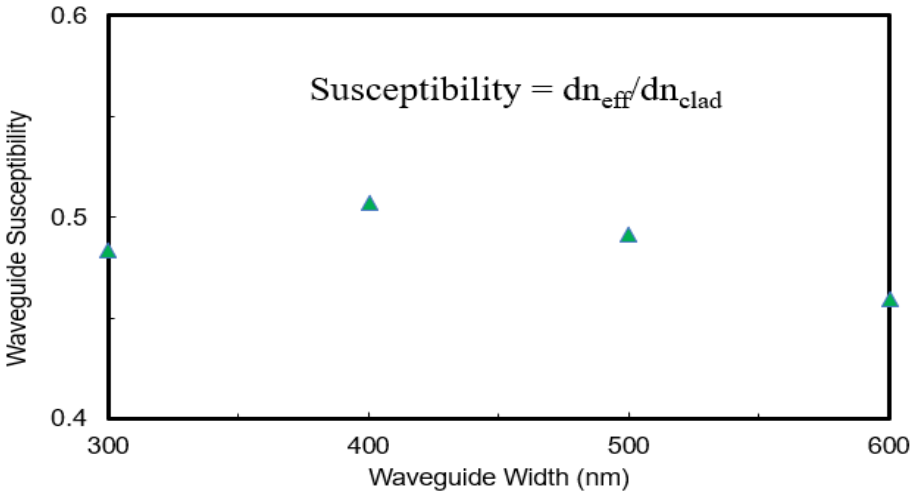

Figure 2-8 Silicon waveguide susceptibility for the quasi-TM mode with height = 220nm and different widths.

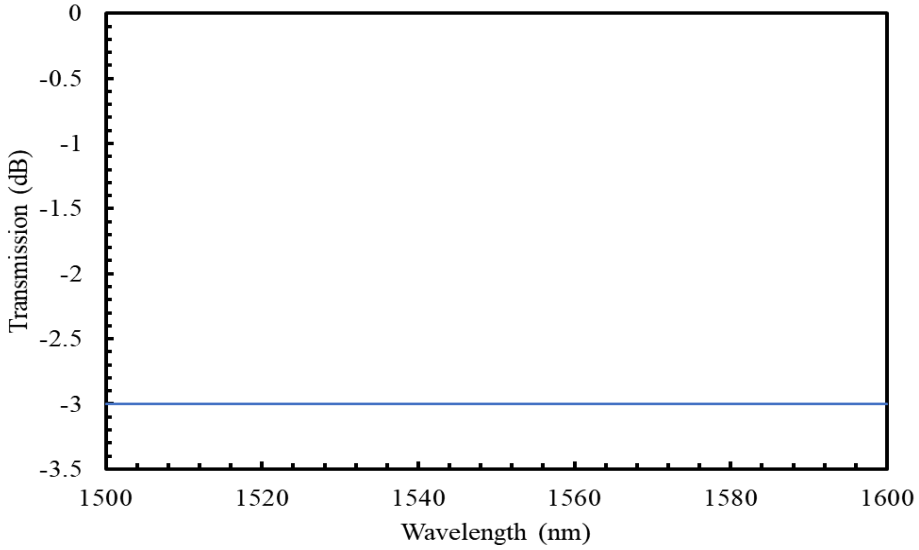

Figure 2-9 Loss of TE polarized silicon waveguide used in the simulations.

2.2 Waveguide Bends

Silicon photonics structures are designed with waveguide bends of 10 µm. The 3D-FDTD simulated loss of the waveguide bend is around -0.0047 dB, as shown in Fig. 2.10.

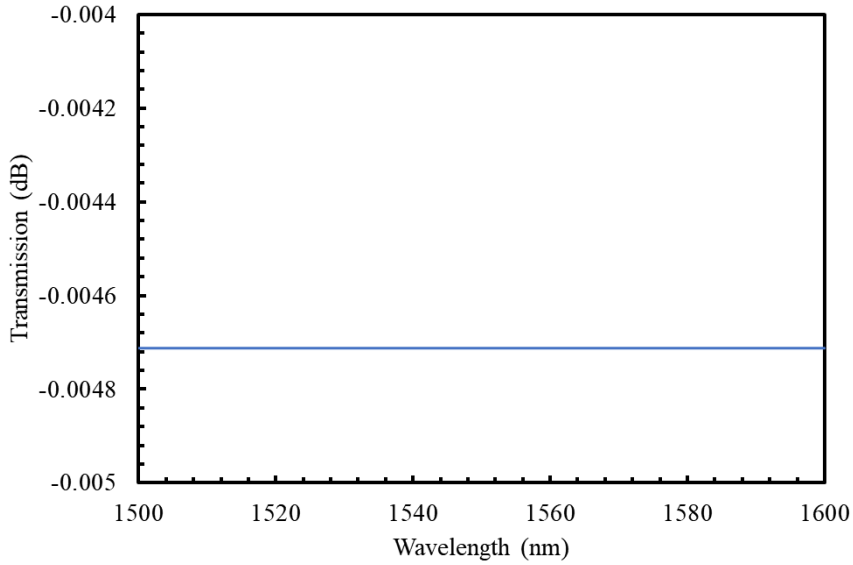

Figure 2-10: Loss of TE polarized Si waveguide bends with R = 10µm, used in the simulations.

2.2.1 Directional Couplers

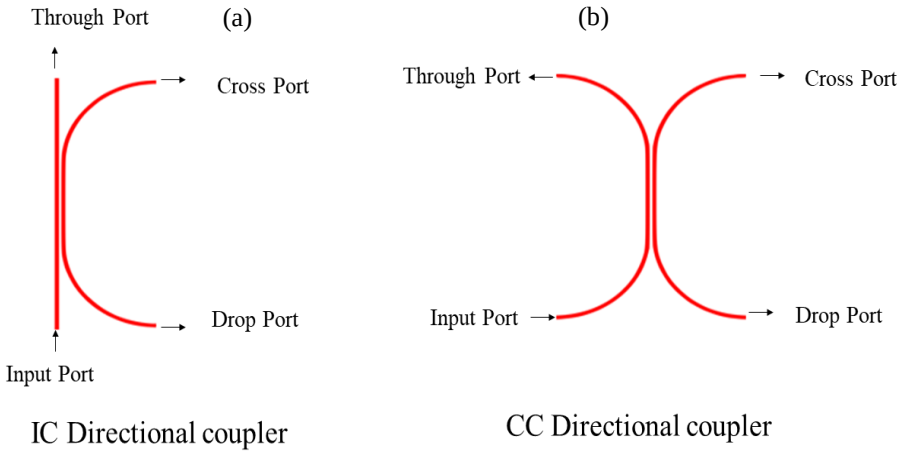

Figure 2-11 :Schematic of (a) the IC and (b) the CC directional coupler.

We used two types of directional couplers (DCs) to design our structures, IC and CC couplers, as shown in Figure 2.11 (a) and (b), respectively. The DC's bends are 10 μm; waveguide dimensions are 500 nm x 220 nm, and the gap between the Si waveguides in the coupling region is kept constant at 200 nm. The coupling constant C values for IC and CC couplers at 1550 nm are provided in Table 1. The coupling constant C values for IC and CC couplers as function of wavelength are plotted in Figure 2.12 and Figure 2.13, respectively. As, the coupling L_c increases form 10 μm to 20 μm in Figures 2.12 and 2.13 (a-k), the 3 dB coupling point moves towards lower wavelengths. The coupling constant values for particular L_c also change with the wavelength, and are not constant in the wavelength range shown.

Table 2-1 Coupling constants for the IC and CC directional couplers (DCs) shown in Figure 2.10 (a) and (b) at 1550 nm.

DC coupling length L_c (μm)	IC coupling constant	CC coupling constant
5	0.01	0.09
10	0.25	0.24
12	0.32	0.31
14	0.4	0.39
15	0.44	0.43
16	0.48	0.47
18	0.56	0.55
20	0.64	0.63
25	0.83	0.81
30	0.93	0.94
35	0.98	0.99

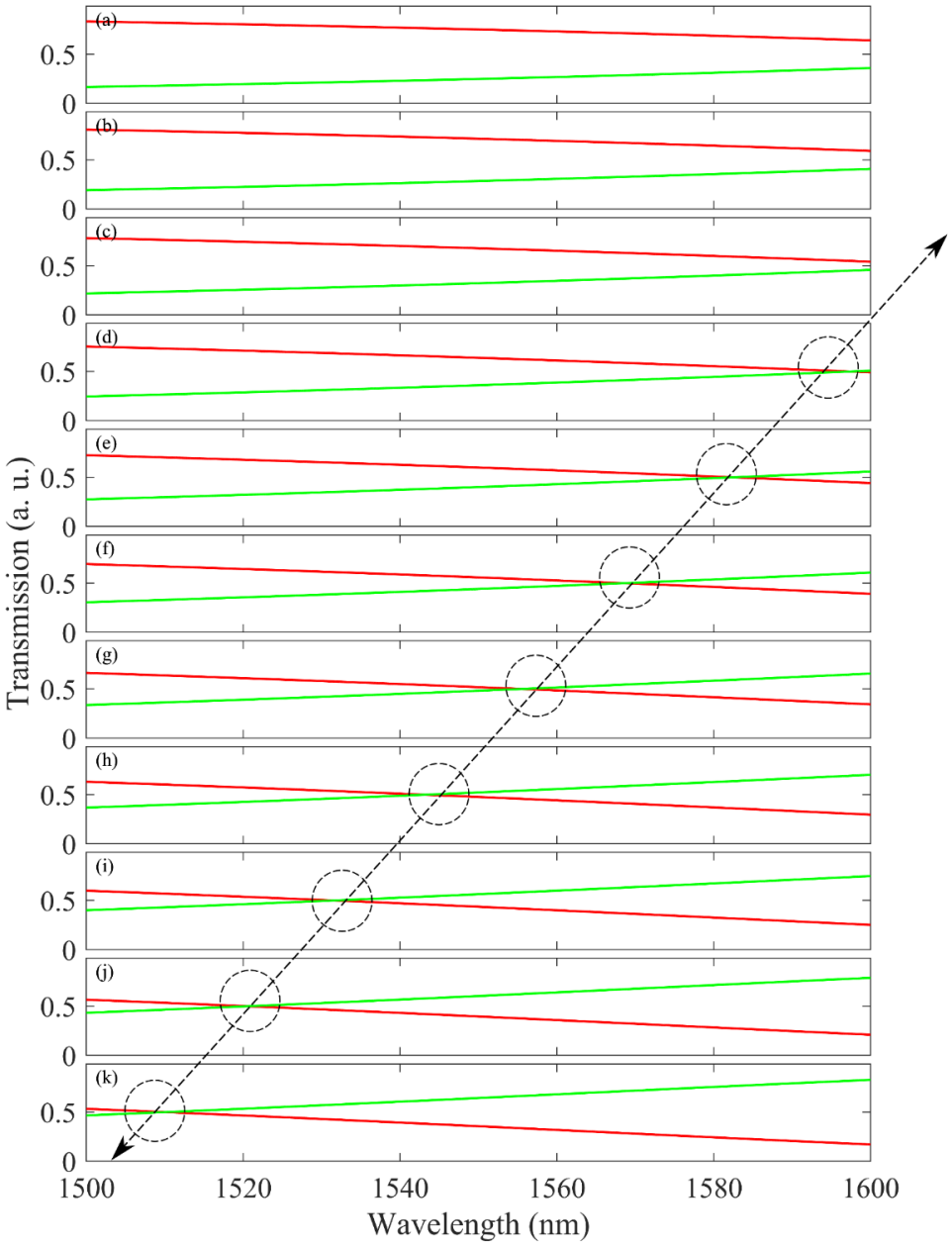

Figure 2-12 (a-k) IC coupler transmission spectra of the cross port (green) and through port (red) as the length of coupling region L_c increases from 10μm to 20 μm.

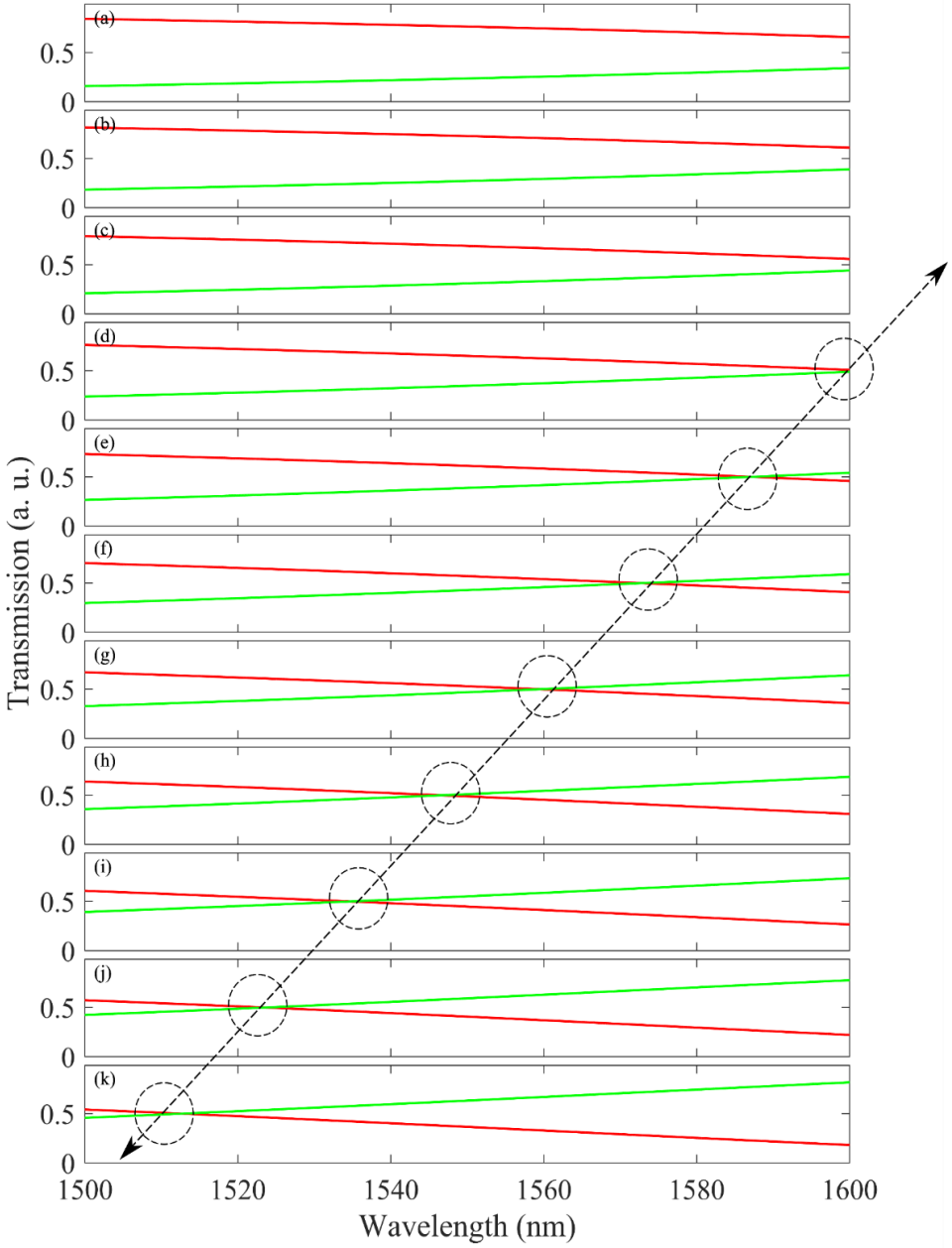

Figure 2-13 (a-k) CC coupler transmission spectra of the cross port (green) and through port (red) as the as length of coupling region L_c increases from 10μm to 20 μm.

2.2.2 Grating Couplers

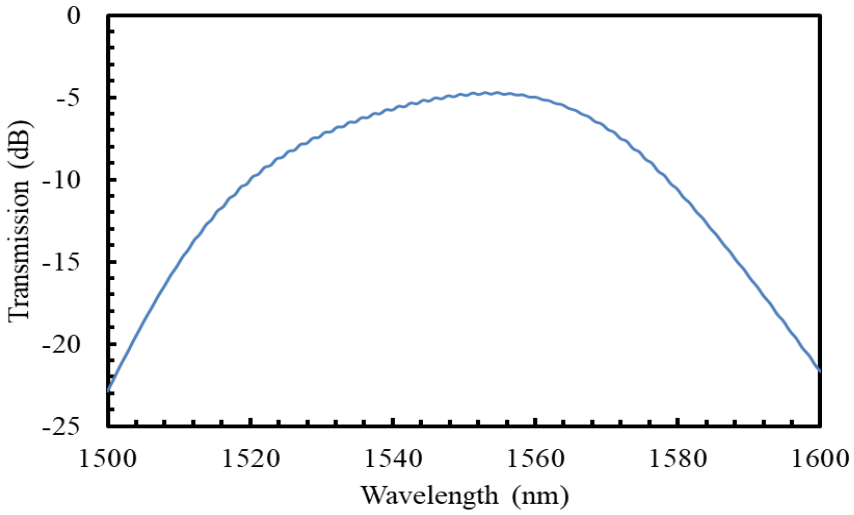

Figure 2-14 Simulated TE GC response.

In order to couple light into the structures, we used the optimized subwavelength grating coupler (GC). For the TE_{00} mode, the GC has a 593 nm grating period, a 237 nm grating width, and a 74 nm subwavelength grating width [63]. The simulated response of the GC with two 10 μm bends and a 127 μm Si waveguide is shown in Figure 2.14. The simulated response shows an insertion loss of -5 dB around 1550 nm. The structures are fabricated at Applied Nanotools (ANT) and University of Washington Nanofabrication Facility (UWNF). The experimental transmission spectra from both facilities are shown in Figure 2.15 and Figure 2.16.

UWNF GC insertion loss is around -15 dB. Also the center of minimum insertion loss is not constant. The ANT GC experimentally measured spectral response is shown in Figure 2.17. and the insertion loss is around -20 dB, which is more than UW GC

insertion loss, but the response is more stable. The SEM image of the structures connected with the GC is shown in Figure 2.17.

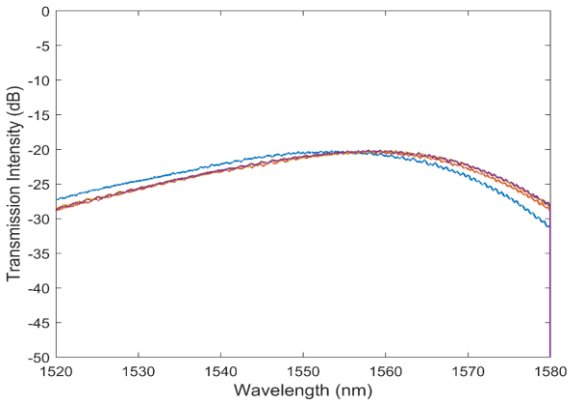

Figure 2-15 ANT GC experimentally measured transmission spectra.

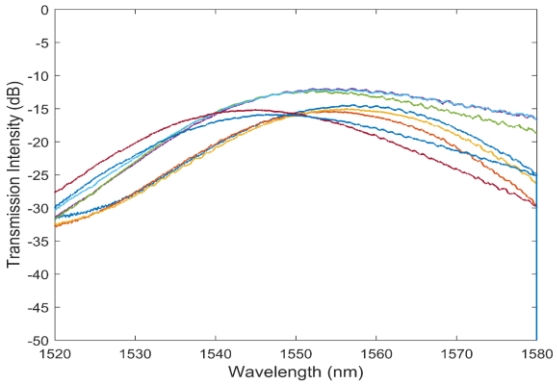

Figure 2-16 UWNF GC experimentally measured transmission spectra.

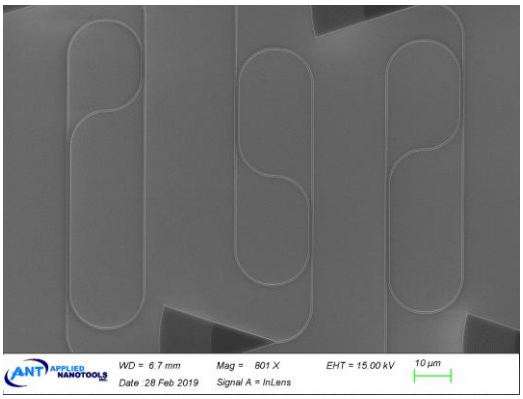

Figure 2-17 The SEM of the antisymmetric meandering resonator (AMR) structures connected with GC.

2.3 Experimental Setup

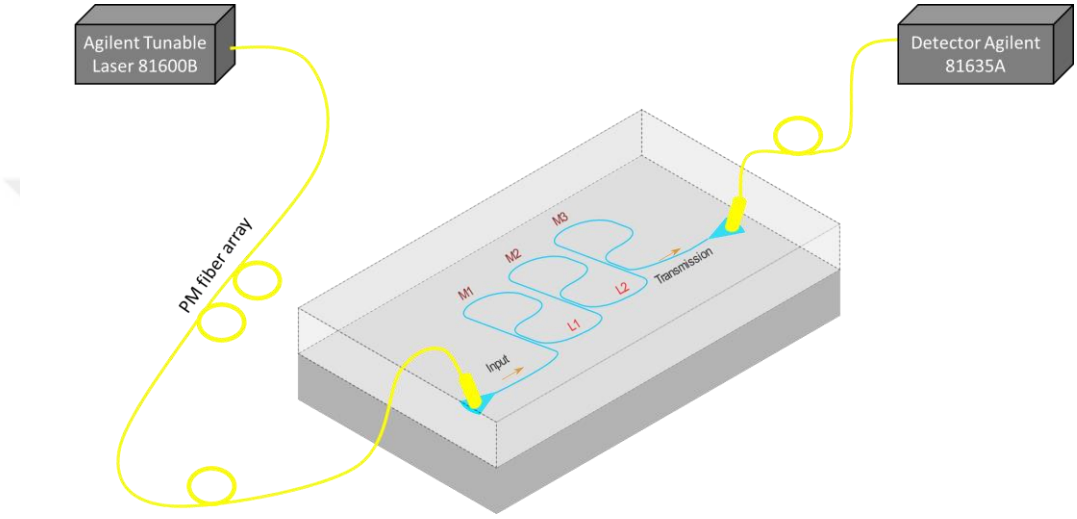

Figure 2-18 Schematic of the experimental setup.

For the experimental transmission spectral measurements a custom-built automated test setup [60], controlled with a Python automated-control software [61], is used. A tunable laser (Agilent 81600B) is used as the light source to measure the transmission spectra with a wavelength sweeping step of 10 pm from 1520 nm to 1580 nm. TE polarization light is coupled in and out of the photonic structures using a single mode polarization maintaining fiber (PMF) array [62], through grating couplers (GCs) [63]. At the outputs, optical power sensors (Agilent 81635A) are used for detecting the transmitted light. A schematic of experimental setup is presented in Figure 2.18. The experimentally measured transmission spectra are presented together with the numerically calculated transmission spectra in the next chapter.

2.4 Fabrication

We used the direct write EBL system of University of Washington Nanofabrication Facility (UWNF) [64] and Applied Nanotools Inc. (ANT) [65] fabrication services for the realization of the structures. At UWNF, the user input is the total area of the pattern to be written, which can be determined using KLayout or Calibre (Mentor Graphics), and the data preparation is performed by the BEAMER (Genisys GmbH) software [66].

The propagation loss is 4 dB/cm for the fabricated strip waveguides, with a width of 500 nm and a height of 220 nm, for the TE polarized light from UWNF process the scattering due to sidewall roughness has the major percentage in this loss [64-67]. Similar waveguides, fabricated with the ANT process, have a propagation loss of 1.5 dB/cm for TE polarized light [65].

The structures are fabricated using an SOI substrate, and the thickness of buried oxide (BOX) layer is 2 μm. Electron beam lithography (EBL) and reactive ion etching (RIE) are used to draw the silicon waveguides. We designed the structure using straight silicon waveguides of 220 nm height and 500 nm width. The bend waveguides have a radii of 10 μm. The resulting structure is then covered by a 2.2 μm-thick SiO_2 cladding layer, which is formed by depositing oxide all around the structures.

2.4.1 ANT Fabrication Process

The photonic devices were fabricated using the NanoSOI MPW fabrication process by Applied Nanotools Inc. [65], which is based on direct-write 100 keV electron beam

lithography technology. Silicon-on-insulator (SOI) wafers of 200 mm diameter, 220 nm device thickness, and 2 μm buffer oxide thickness are used as the base material for the fabrication. The wafer was prediced into square substrates with dimensions of 25 mm x 25 mm, and lines were scribed into the substrate backsides to facilitate easy separation into smaller chips once the fabrication was complete. After an initial wafer cleaning using piranha solution (3:1 H2SO4:H2O2) for 15 minutes and water/IPA rinse, hydrogen silsesquioxane (HSQ) resist was spin-coated onto the substrate, and heated to evaporate the solvent. The photonic devices were patterned using a Raith EBPG 5000+ electron beam instrument using a raster step size of 5 nm. The exposure dosage of the design was corrected for proximity effects, that result from the backscatter of electrons from exposure of nearby features. Shape writing order was optimized for efficient patterning and minimal beam drift. After the e-beam exposure and subsequent development with a tetramethylammonium sulfate (TMAH) solution, the devices were inspected optically for residues and/or defects. The chips were then mounted on a 4” handle wafer and underwent an anisotropic ICP-RIE etch process using chlorine, after qualification of the etch rate. The resist was removed from the surface of the devices using a 10:1 buffer oxide wet etch, and the devices were inspected using a scanning electron microscope (SEM) to verify patterning and etch quality. A 2.2 μm oxide cladding was deposited using a plasma-enhanced chemical vapor deposition (PECVD) process based on tetraethyl orthosilicate (TEOS) at 300 ºC. Reflectrometry measurements were performed throughout the process to verify the device layer, buffer oxide and cladding thicknesses before delivery.

Chapter 3 Integrated Silicon Photonics Structures proposed for Biosensing

3.1 Meandering Loop Mirror

The basic element of our structures is meandering loop mirror (MLM). MLM has one DC, the through port and the cross port of that DC are joined to form a loop mirror, as shown in Figure 3.1(a). The mathematically analyzed transmittance of the MLM as a function of coupling constant, C is plotted in Figure 3.1(b). For a single MLM, when there is no coupling at the DC, i.e., C = 0, the input follows a CW path, and a maximum transmission is observed. When the coupling at the DC is maximum, i.e., C = 1, the input follows a CCW path and again a maximum transmission is observed. When C is between 0 and 1 at the DC, the input follows both CW and CCW paths. The minimum transmission is observed, when C = 0.5 at the DC.

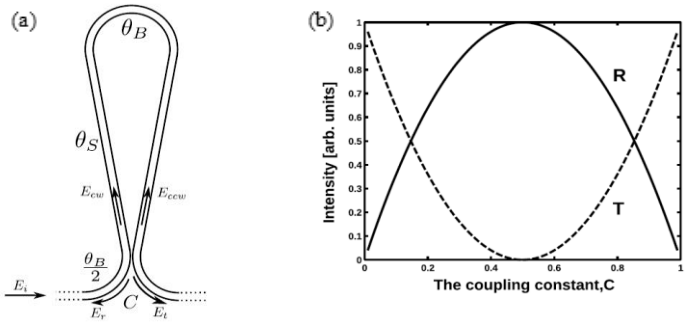

Figure 3-1 (a) The proposed MLM design, and (b) the mathematically calculated transmittance and reflactance response. [107]

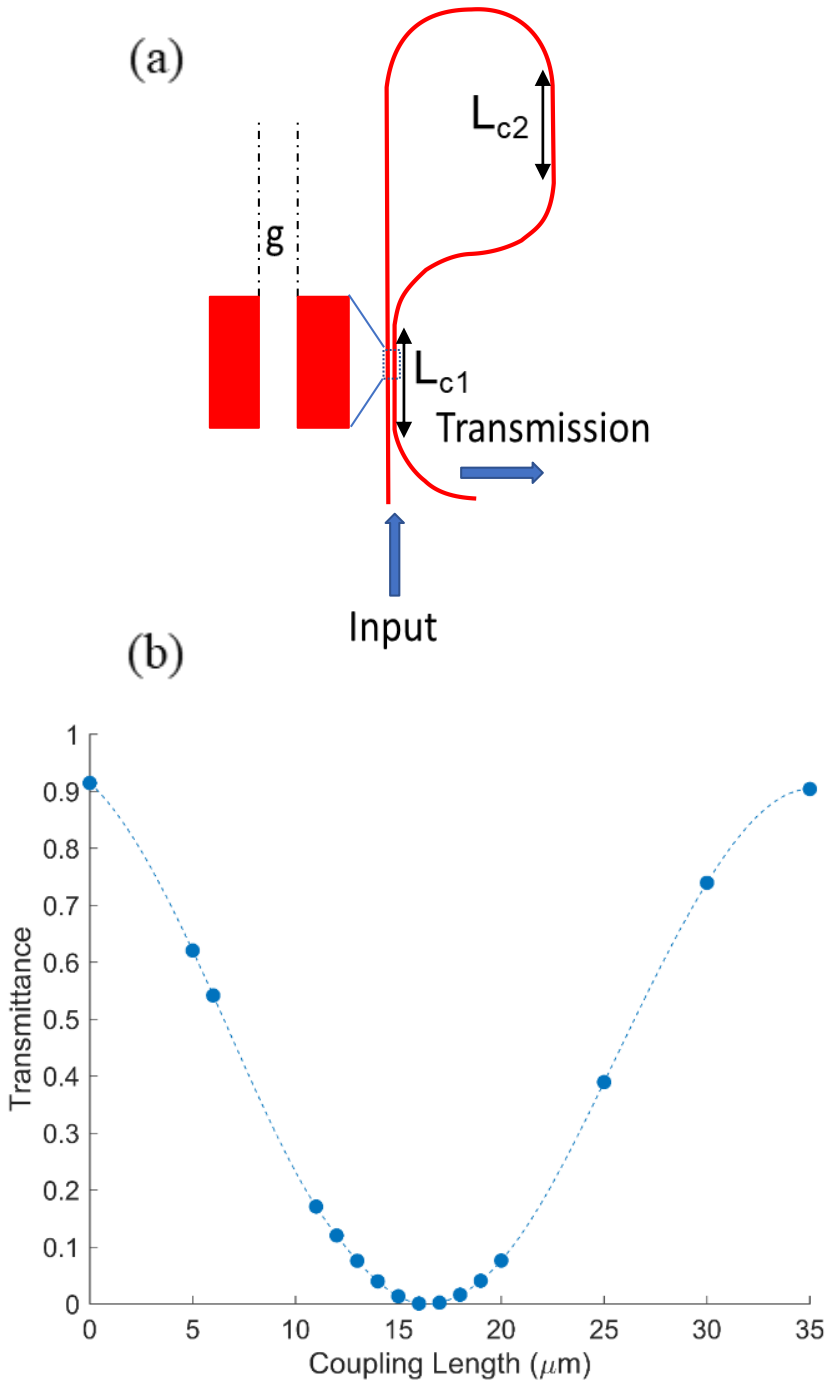

Figure 3-2 : (a) Schematic of the MLM design and (b) the transmittance of the MLM as a function of the coupling length L_c.

The schematic of the physical design of the MLM with the Si waveguide and the DC is shown in Figure 3.2 (a). Si waveguide dimensions are 500 nm x 220 nm. The gap 'g' between two waveguides in DC region is 200 nm, and is kept the same in all the designs. The coupling length L_c is the length of the Si waveguides in DC region. The waveguide bends radius of curvature is R = 10 µm. The L_c is varied to change the coupling constant C in the DC. The 3D FDTD transmittance of MLM structure as a function of L_c is plotted in Figure 3.2(b). The ML M transmittance is minimum around L_c = 16 µm and is maximum, when L_c = 0 or 35 µm.

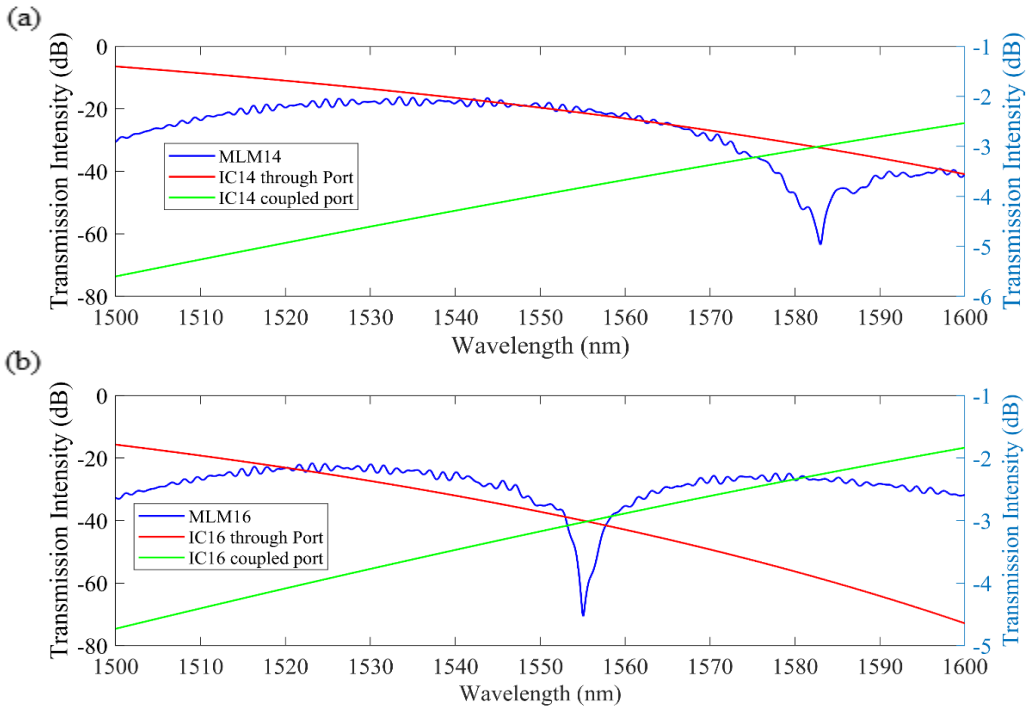

Figure 3-3 3D-FDTD simulated response of the MLM with (a) L_c = 14 µm and (b) L_c = 16 µm.

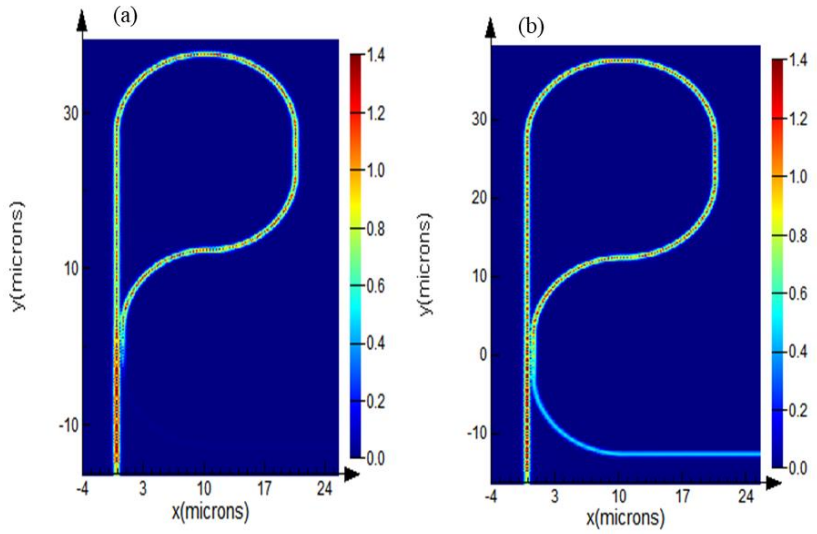

Figure 3-4 Electric field distribution, when the MLM has (a) a dip and (b) a peak in the transmission.

3D FDTD simulated response of MLM with L_c = 14 µm and L_c = 16 µm are plotted in Figure 3.3 (a) and (b), respectively. MLM transmission intensity is plotted on left y-axis and DC transmission intensity on right y-axis. MLM shows a dip, when the DC has 3 dB coupling, and this dip moves towards the lower wavelength as L_c increases. Figure 3-4 shows the electric field distribution, when the MLM has (a) a dip and (b) a peak in the transmission.

3.2 Meandering Resonator

Two MLMs can be connected together to create a meandering resonator (MR). The MR resonator shows Lorentzian peaks in the transmission spectrum and the peaks have high Q-factors near the 3dB coupling point. The MR schematic with two MLM's connected together is shown in Figure 3.5.

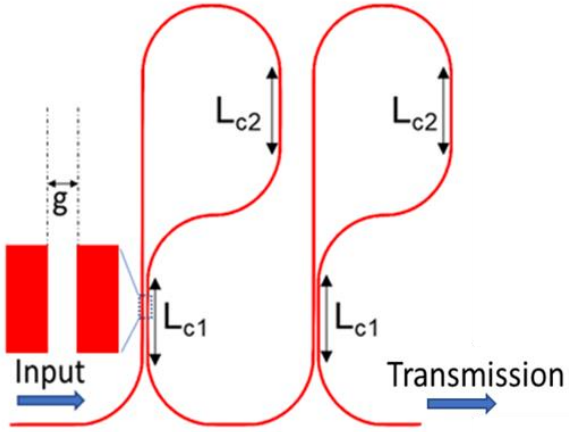

Figure 3-5 Schematic of the MR structure.

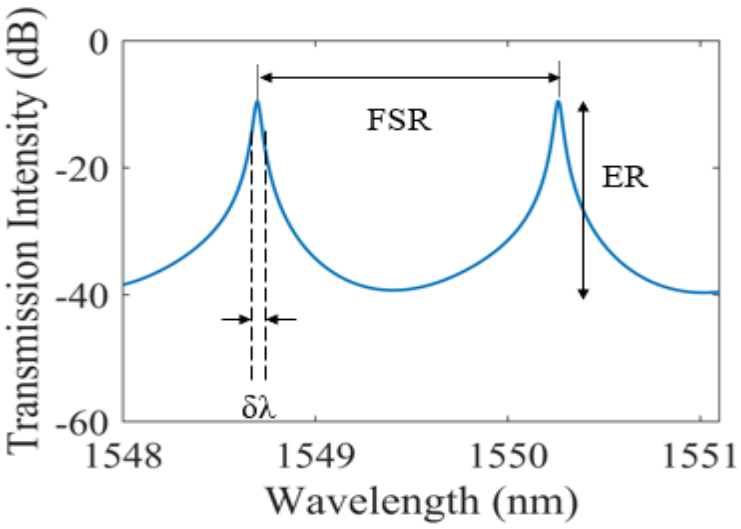

Figure 3-6 3D FDTD simulated transmission spectral response of the MR structure.

The transmission spectral behavior of the MR shows Lorentzian peaks, as shown in Figure 3.6. The distance between the peaks is termed as the free spectral range (FSR) and can be calculated as:

$$FSR = \Delta\lambda = \frac{\lambda^2}{L.n_g} \tag{3.1}$$

The Q-factor has been defined already, and the ER gives the difference between the maximum and the minimum of the transmission. The 3D FDTD simulated spectral response of MR structure, as L_c increases from 10 µm to 20 µm, is shown in Figure 3.7, and is compared with the MDFB in the next section.

3.3 Antisymmetric Meandering Resonator

The antisymmetric meandering resonator has two DCs as shown in schematic and SEM image in Figure 3.8. The spectral response show peak at resonance wavelengths and Q-factor of peaks increase as L_c is increased from 10µm to 20µm. 3D FDTD simulated and experimental results are plotted for AMR structure with L_c=10 µm in Figure 3.9 (a) and (b) respectively. 3D FDTD simulated transmission and reflection, and (b) experimentally spectral response for AMR structure with L_c=10 µm and L_c=20 µm, which corresponds to C values of 0.24 and 0.64, are plotted in figure 3.9 and 3.10, respectively. We can observe the peaks in the spectral response gets sharper as C increases and this trend is observed in both simulations and experimental results.

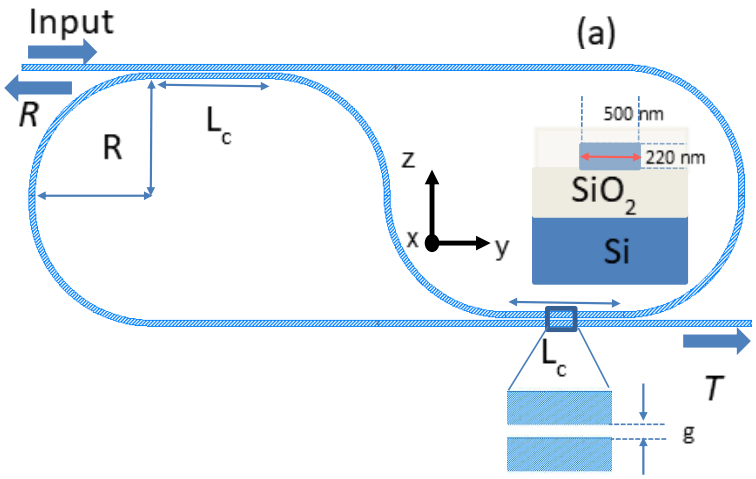

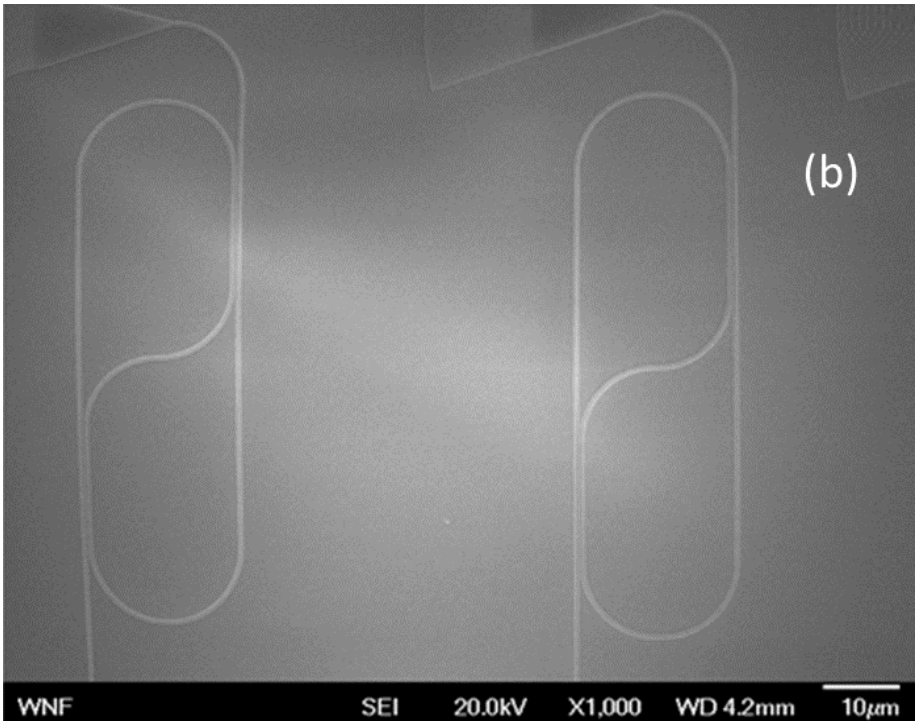

Figure 3-7 (a) The schematic and (b) the SEM image of the antisymmetric meandering resonator.

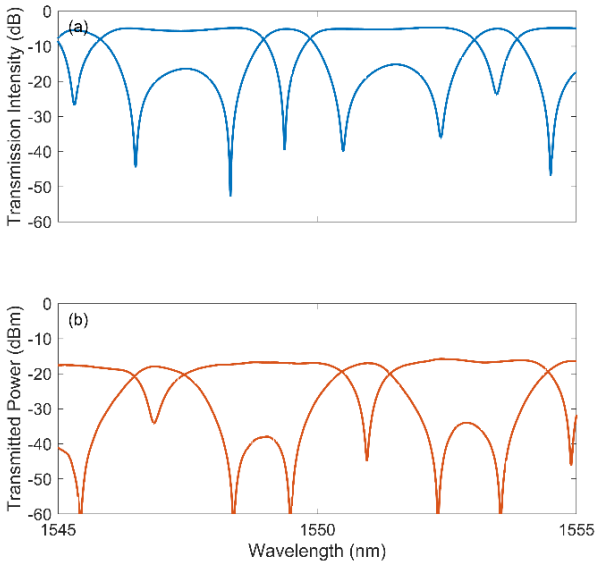

Figure 3-8 (a) 3D FDTD simulated, and (b) experimental transmission (high ER) and reflection (low ER) spectra for the AMR structure with L_c = 10 µm.

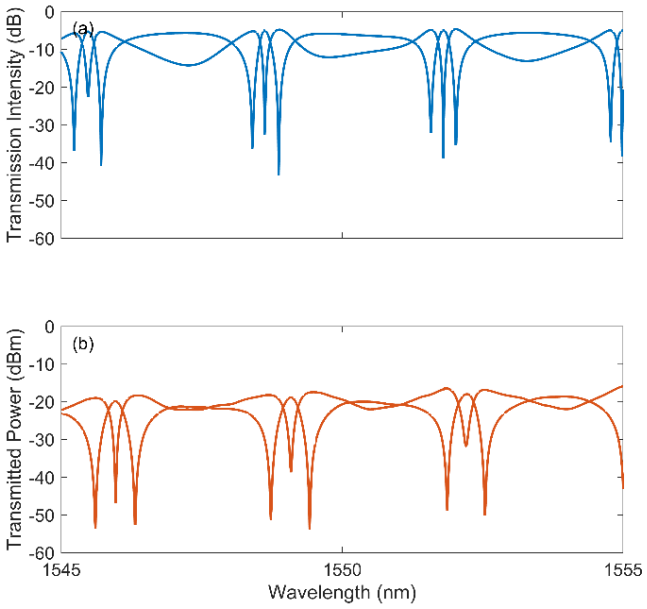

Figure 3-9 (a) 3D FDTD simulated, and (b) experimental transmission (high ER) and reflection (low ER) spectra for the AMR structure with L_c = 20 µm.

3.4 Symmetric Meandering Resonator

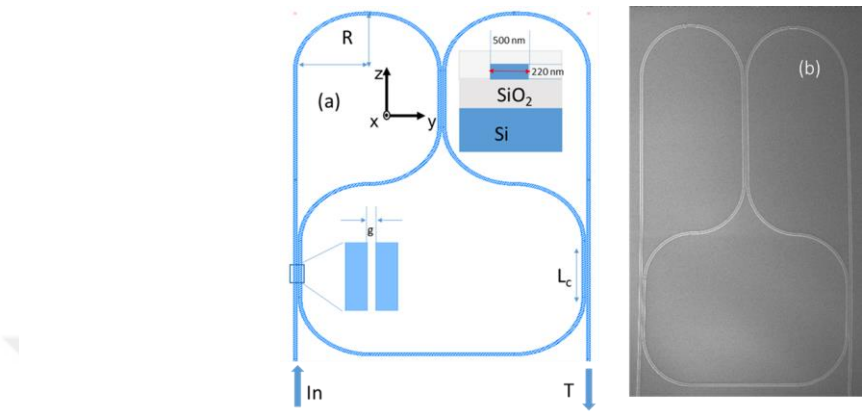

Figure 3-10 : (a) The schematic and (b) the SEM image of the symmetric meandering resonator.

The symmetric meandering resonator has three coupling regions, as shown in Figure 3.10. The spectral response has Fano-lineshapes with mode splitting, when all directional couplers have $L_c = 12\mu m$, which is evident in both 3D FDTD simulations and experimental measurements shown in Figure 3.11 (a) and (b), respectively.

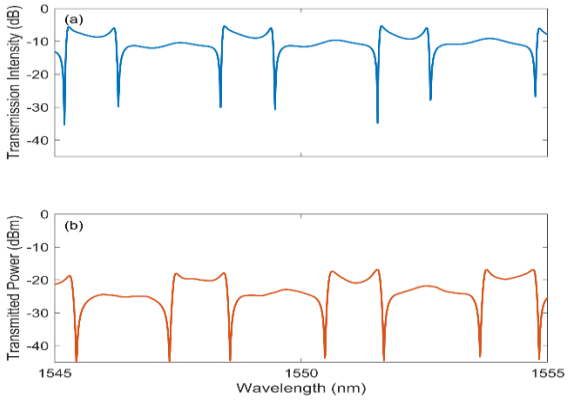

Figure 3-11 (a) 3D FDTD simulated and (b) experimental transmission spectrum for the SMR structure with $L_c = 12\mu m$

3.5 Meandering Distributed Feedback Structure

In this section, we propose a meandering distributed feedback (MDFB) photonic structure formed by joining three MLM structures in series, exhibiting spectral mode splitting of the meandering resonators (MRs) in the transmission spectrum towards the application as a temperature sensor.

The MR structure is the analog of a FP cavity and MDFB structure can be thought as a two-stage FP cavity. The output from the first stage has a Lorentzian lineshape, which is fed to the second stage of the MDFB. The three-mirror FP cavity has been theoretically analyzed [68-69], and experimentally demonstrated [70]. The minimum of the 3 mirror MDFB structure (the analog of the three mirror FP cavity) also has a lower transmission minimum than the MR (the analog of the two mirror FP cavity) as expected [18], due to a better spectral definition.

Mode splitting has also been observed in many SOI-based optical circuits, such as microrings, by fabricating gratings on the sidewalls [71-72], by using ring resonator with feedback coupled waveguide [73], and by coupling microrings [74]. Mode splitting in photonic crystal (PC) SOI slabs has been analyzed [75], and experimentally observed [76]. Mode splitting in SOI can also be utilized for nanoparticle chemical sensing [77].

Spectral mode splitting in SOI with Sagnac loop mirrors has been experimentally demonstrated [78], however the device footprint was large. We are proposing spectral mode splitting in a meandering waveguide SOI structure, that is tunable, easy to fabricate, and with a small footprint, as compared to microrings and PC slabs.

An ambient temperature sensor based on a meandering distributed feedback (MDFB) lightwave structure was formed by cascading three MLMs. This structure can also be used for integrated photonics applications such as optical filtering.

3.5.1 Design and Simulation of The Meandering Distributed Feedback Structure

The schematic and a scanning electron microscope (SEM) image of the MDFB structure are shown in Fig. 3.12(a) and (b), respectively. The MDFB structure consists of three MLMs. The MLM consists of a directional coupler (DC) bent onto itself. The gap of the DC is g = 200nm, the length of the straight waveguide between the MLMs are $L_1 = L_2 = 5$ μm, the radius of curvature of the loops are R = 10 μm, and the coupling and extension lengths are L_{c1} = 22 μm, respectively.

The first and third MLMs are coupled to the input and output waveguides, respectively. The input laser enters the MDFB structure through the left bottom waveguide with direction labeled as ‘Input’ and the output power was measured through the right bottom waveguide with direction labeled as ‘Transmission’.

The MLM has 100% transmittance, when C = 0 (100% clockwise (CW) propagation) or 1 (100% counterclockwise (CCW) propagation), and has 100% reflectance for C = 0.5. CW and CCW electromagnetic fields co-propagate in the MLM for other values of C.

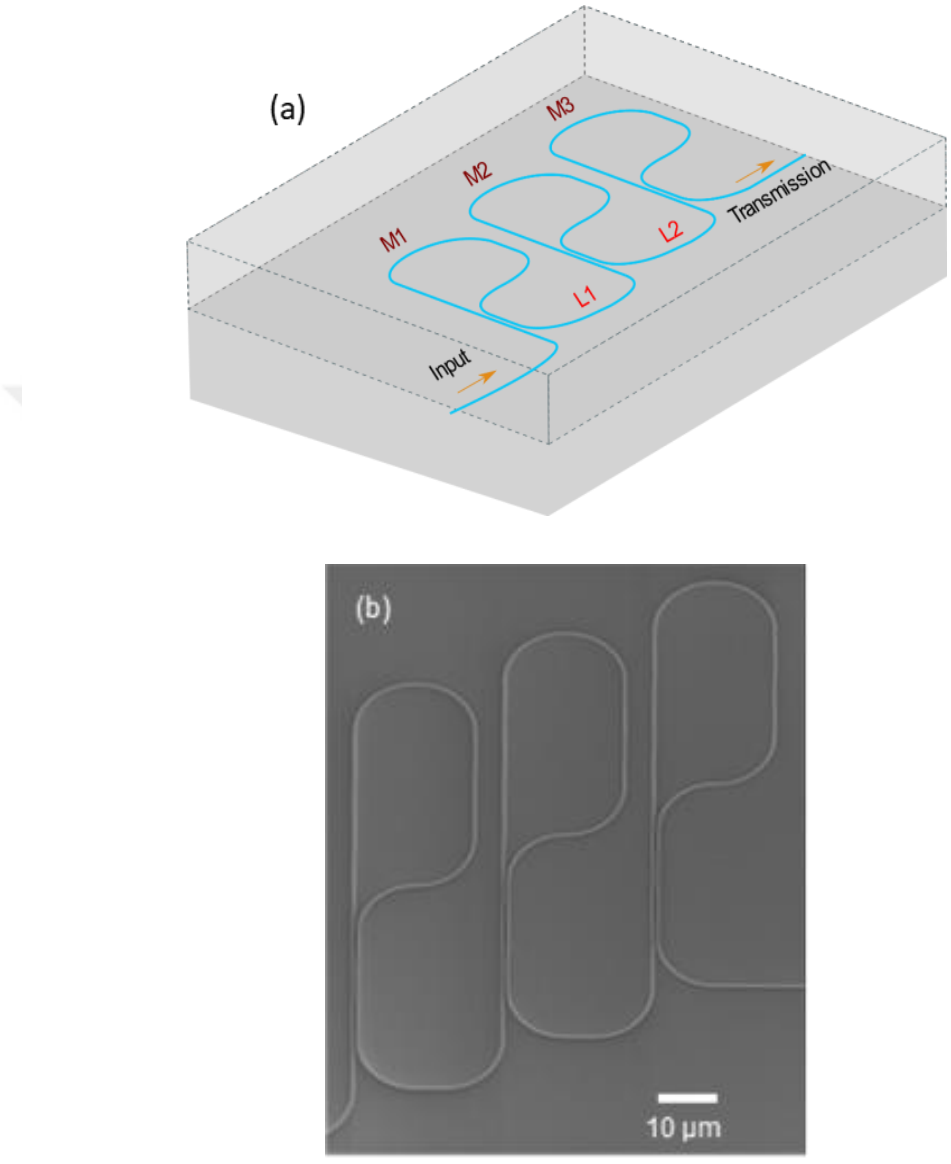

Figure 3-12 (a) The schematic, and (b) the SEM of the MDFB with 3 MLMs. The gap is g = 200 nm, the separation between the MLMs are L_1=L_2=5 µm, the radius of curvature R = 10 µm, and the coupling length is L_{c1} = 22 µm.

The numerically calculated transmittance at a wavelength of 1500 nm of the MLM structure with R = 10 µm and g = 200 nm as a function of coupling length L_c is shown in Fig. 3.13. MLM behaves as perfect mirror, when L_c is around 15 µm and

transmittance increases when L_c is 0 µm or 35 µm. This effect of single MLM is also evident in MR and MDFB resonators.

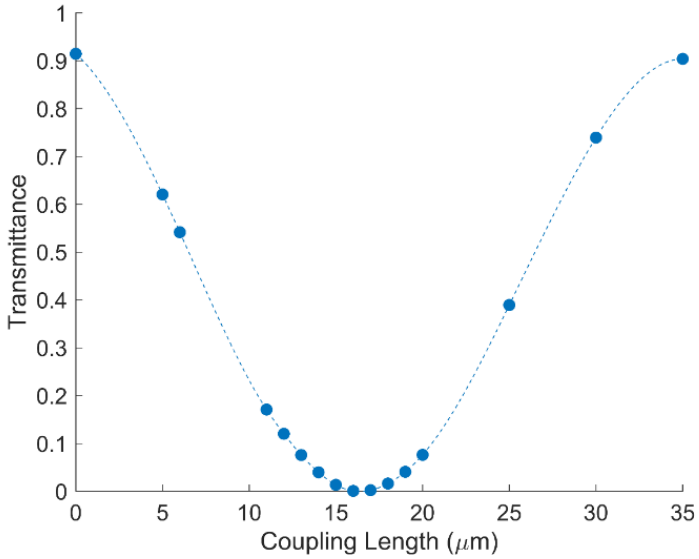

Figure 3-13 The numerically simulated transmittance of an MLM as function of coupling length at 1500 nm. MLM behaves as perfect mirror, when L_c is around 15 µm and transmittance increases when L_c is 0 µm or 35 µm. This effect of single MLM is also evident in MR and MDFB resonators.

MLM transmission and reflection functions can be expressed as [79]:

$$t_{MLM} = (t^2 - \kappa^2)a_1 e^{-j\beta l_1} \quad (3\text{-}1),$$

and,

$$r_{MLM} = 2jt\kappa a_1 e^{-j\beta l_1} \quad (3\text{-}2),$$

where t is the directional coupler (DC) waveguide self-coupling coefficient of the MLM, κ the DC waveguide coupling coefficient of the MLM, $a_1 = e^{\frac{-\alpha l_1}{2}}$ the MLM loss coefficient, $\beta = \frac{2\pi n_g}{\lambda}$ the propagation constant, and l_1 the length of the MLM.

The field transmission and reflection function of MR structure, which consists of two identical MLMs can be mathematically written as [79]:

$$t_{MR} = \frac{t_{MLM}^2 a_2 e^{-j\beta L_1}}{1 - r_{MLM}^2 a_2^2 e^{-2j\beta L_1}} \quad (3\text{-}3),$$

and,

$$r_{MR} = \frac{r_{MLM} + (t_{MLM}^2 - r_{MLM}^2) r_{MLM} a_2 e^{-j\beta L_1}}{1 - r_{MLM}^2 a_2^2 e^{-2j\beta L_1}} \quad (3\text{-}4),$$

where, L_1 is the waveguide length between the two MLMs, and $a_2 = e^{\frac{-\alpha L_1}{2}}$ the loss coefficient associated with the waveguide between the two MLMs.

Similarly, the transmission field function of the MDFB structure, which consists of identical three MLMs, and the same distance between the MLMs can be written as [78]:

$$t_{MDFB} = \frac{t_{MR}\, t_{MLM} a_2 e^{-j\beta L_2}}{1 - r_{MR} r_{MLM} a_2^2 e^{-2j\beta L_2}} \quad (3\text{-}5).$$

L_1 and L_2 are the silicon waveguide lengths connecting the two MLMs, which are identical in our designs. By selecting $t = 0.87$ ($t^2 + \kappa^2 = 1$, for a lossless resonator), $n_g = 4.2$, $l_1 = 124$ μm, $L_1 = 36.4$ μm, $\alpha = 69$ /m for a propagation loss of 3 dB/cm, we can plot MR and MDFB transmission intensity using Eq. (3.1) – (3.5), as shown in Figure 3.14.

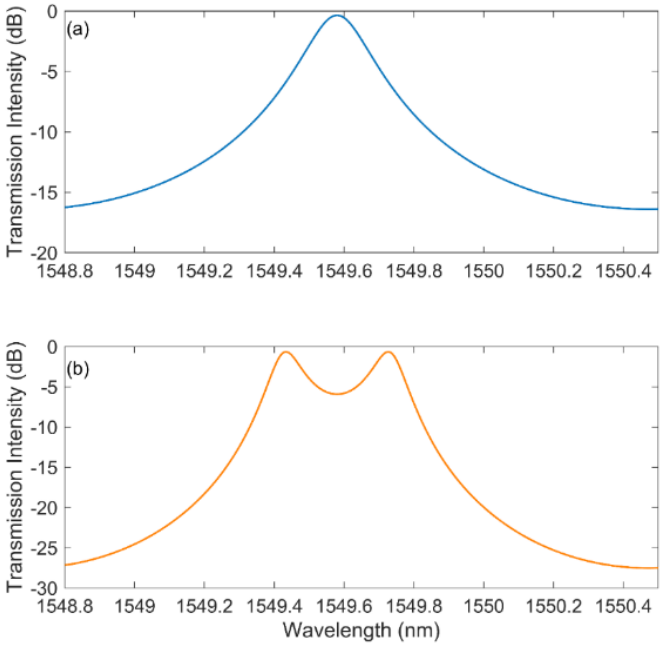

Figure 3-14 Transmission intensity of (a) MR and (b) MDFB structure using Eq. (3.1) – (3.5). MR structure consisting of two MLMs has one resonant peak in one FSR and MDFB structure consisting of three MLMs exhibiting mode splitting due to coupling of two resonances.

MR (formed by connecting two identical MLM's) structure has a peak at the resonance wavelength, and when we put one more MLM to make MDFB structure, two MR resonators are coupled and, in the transmission, there are two peaks as the resonances push one another. The Q-factor of the single peak of the MR is 8×10^3, which increases to 15×10^3, when the peaks split in the MDFB. We can also observe that, the overall extinction ratio of transmission spectrum increases for the MDFB, as shown in Figure 3.14 (a) and (b), which also makes the MDFB a better resonator than the MR. This increase in the extinction ratio (ER) is due to the increased mutual coupling of the resonators, and has been studied in coupled ring resonators [71-80].

The spectral responses of the MR and MDFB structure are also analyzed using the transfer matrix method (TMM) [107], and 3D FDTD simulations are further performed to verify the analytical model. 3D FDTD simulations of the straight waveguides, bent waveguides, and DCs were also performed with the FDTD suite (Lumerical Solutions, Inc.). The s-parameters of the individual components were imported to Interconnect (Lumerical Solutions, Inc.) to observe the response of complete structure. A 500 nm-wide and 220 nm-high silicon (n_{Si} = 3.48) waveguide is covered by silicon dioxide (n_{SiO2} = 1.44) cladding on all sides. The directional coupler's coupling length L_c remains identical for all MLM's and is varied from 10 μm to 15 μm. The directional coupler's coupling gap is 200 nm for all structures. The bending waveguides have 10 μm bending radius for all the structures investigated in this study. The scope of this research is to study and design symmetric structures, so the coupling length (L_c) in all the individual MLM, which is also the unit cell of MDFB, is kept same for one structure and is varied in different structure. 3D FDTD simulated results of MR and MDFB structures from L_c = 10 μm to L_c = 15 μm are plotted in Figure 3.15 (a-f) and (g-l), respectively. Simulations results also have grating couplers response, which add a -5 dB insertion loss. As expected from the numerical calculation plot in Figure 3.14, we can observe Lorentzian peaks in the MR spectral transmission, and split peaks in the MDFB spectral transmission. As the Lc increases, and the coupling increases, the MR peaks become sharper.

The insertion loss also increases with Lc and λ, as coupling also depends on λ, and around Lc = 15μm the transmittance of single MLM is very low as shown in Figure 3.13, and is also evident in Figure 3.15.

The MR spectral response show a single peak and MDFB spectral response has mode splitting. The MR peaks become sharper as L_c increases. MDFB peaks also become sharp and split distance is also reduced as L_c increases. The insertion loss also increases as the coupling approaches nearer to 3-dB coupling point.

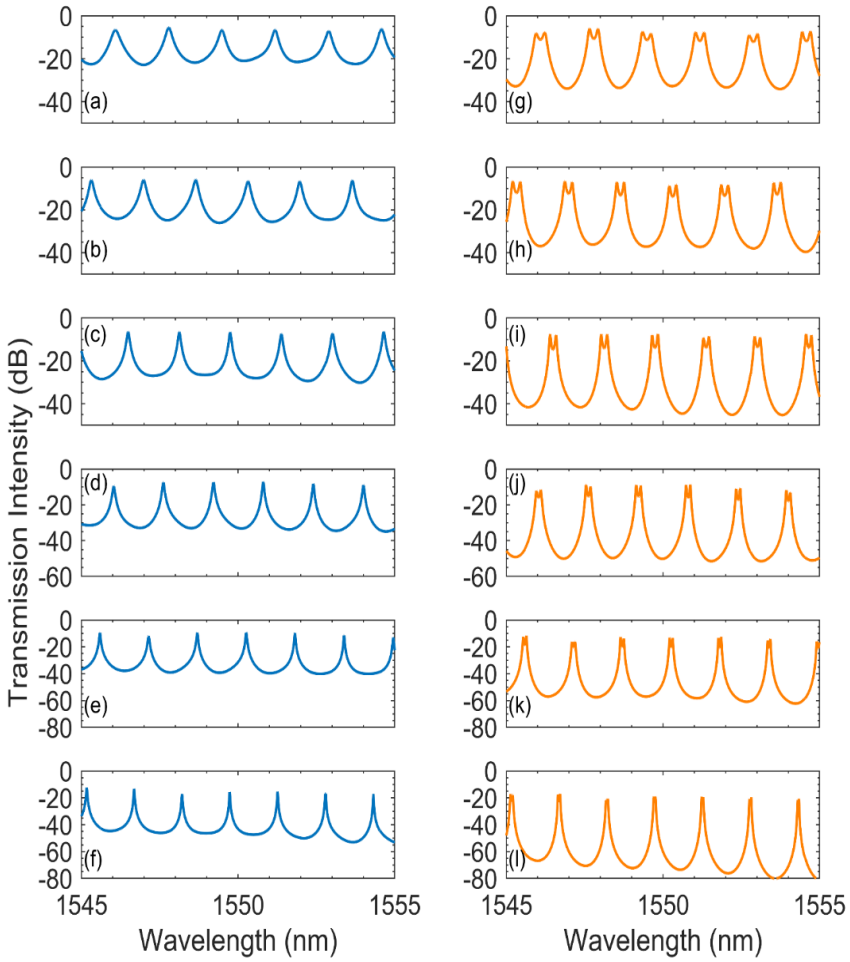

Figure 3-15 The 3D FDTD simulation of the transmission spectra of (a-f) the MR and (g-l) the MDFB from Lc = 10µm to Lc = 15µm.

Fig. 3.16 (a-f) and (g-l) shows the experimentally measured transmission spectra of a two stage MLM (MR) and a three stage MLM (MDFB) with an increase in L_c from

10 μm to 15 μm. Fig. 3.16(e) and (k) show the experimental transmittance spectra of the MR and the MDFB with L_c = 14 μm. The MR shows an ER of 22 dB and a Q-factor of 3.0 x 10^4, while the MDFB shows an overall ER of 35 dB and a Q-factor around 4.0 x 10^4.

Fig. 3.16 (f) and (l) show the experimental transmittance spectra of MR and MDFB with L_c = 15 μm. The MR shows an ER of 24 dB and a Q-factor of 4.0 x 10^4, while the MDFB shows overall an ER of 36 dB and a Q-factor around 5.0 x 10^4. As, observed in the simulations, the Q-factor of the MR and the MDFB also increases as the coupling increases by increasing L_c in the experimental measurements. The insertion loss also increases and the distance between the split peaks reduce for the MDFB, by increasing L_c as the coupling approaches 3-dB point.

Table 3.1 summarizes the FSR comparison of the numerically simulated and experimentally measured transmission spectra of the MR and the MDFB structures, with coupling lengths of Lc = 10, 11, 12, 13, 14, and 15 μm, showing good agreement with each other. We can observe that, the FSR of teh MR and the MDFB for specific coupling lengths are identical. The FSR of the MR is given by the expression, FSR = $\Delta\lambda = \lambda^2/n_gL$, where λ is the vacuum wavelength, n_g the group index (n_g = 4.2 at 1550 nm for 500 nm x 220 nm strip waveguide with SiO_2 cladding), and L the roundtrip length of the resonator. In the MDFB, the two MRs are coupled to each other [81]. The MDFB totals lengths are 341 μm, 347 μm, 353 μm, 359 μm, 365 μm and 371 μm for L_c =10, 11, 12, 13, 14, and 15 μm, respectively.

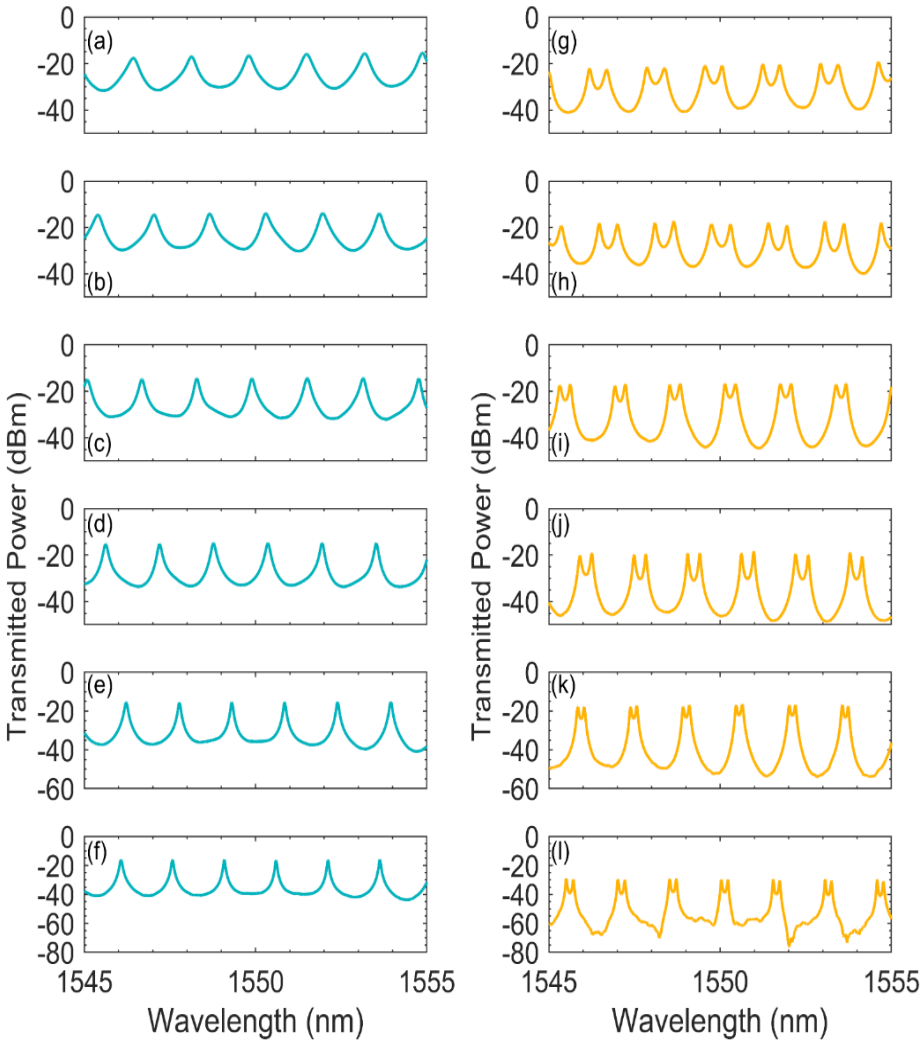

Figure 3-16 Experimental transmission spectrum of (a-f) the MR and (g-l) the MDFB structure with Lc = 10μm to 15 μm. The MDFB show better overall ER than the MR, which is required for sensing applications. The Q-factor of the MDFB is also higher than the MR, that will lead to a better limit of detection (LOD).

Table 3-1 The FSR comparison of the MRs and the MDFBs with coupling lengths of 10, 12, 13, 14, and 15 μm.

FSR (nm)	MR		MDFB	
L_{c1} (μm)	simulation (nm)	measurement (nm)	simulation (nm)	measurement (nm)
10	1.69	1.68	1.69	1.69
11	1.66	1.67	1.66	1.66
12	1.63	1.63	1.63	1.62
13	1.6	1.59	1.59	1.58
14	1.56	1.55	1.56	1.55
15	1.52	1.52	1.52	1.51

The Q-factor and the ER values of the MR and the MDFB structures are provided in Table 3.2 and 3.3, respectively. We can deduce that the MDFB has better Q-factor and ER values, which make the MDFB a better filter than the MR. The Q-factor is better, resulting in a better dynamic range, which will lead to better limit of detection (LOD).

Table 3-2 The Q-factor comparison of the MRs and the MDFBs with coupling lengths of 10, 11, 12, 13, 14, and 15 μm.

Q-factor	MR		MDFB	
L_{c1} (μm)	simulation	measurement	simulation	measurement
10	9×10^3	7×10^3	1.4×10^4	1.4×10^4
11	1.3×10^4	1.0×10^4	2.0×10^4	2.0×10^4
12	2.0×10^4	1.5×10^4	3.0×10^4	2.6×10^4
13	3.0×10^4	2.0×10^4	4.0×10^4	3.0×10^4
14	4.0×10^4	3.0×10^4	5.0×10^4	4.0×10^4
15	6.0×10^4	4.0×10^4	7.0×10^4	5.0×10^4

Table 3-3 ER comparison of MRs and MDFBs with coupling lengths of 10, 11, 12, 13, 14, and 15 μm.

ER (dB)	MR		MDFB	
L_{c1} (μm)	simulation	measurement	simulation	measurement
10	15	13	26	21
11	18	15	30	21
12	20	17	34	27
13	26	18	40	29
14	28	22	44	35
15	29	24	50	36

3.5.2 Ambient Temperature Sensing With The MDFB

Thermo-optic coefficient (TOC) of Si (change in the refractive index of silicon with temperature) dn/dT = 1.86 x 10-4 K-1 [82]. This property of silicon has been utilized

to fabricate integrated thermo-optic switches [83] and thermally tunable modulators [84]. SiO2 TOC is $dn/dT = 10^{-5}$ K^{-1} [85], which is very low compared to Si. Temperature variations affect the TE mode more than the TM mode, as the TE mode is more confined in the channel buried waveguide core. Temperature variation effects have been studied in different photonic structures. Temperature sensitivity of $S = 77$ pm.K^{-1} has been observed in ring resonator coupled to a waveguide with dimensions of 610 nm x 220 nm supporting TE polarization [86]. A higher temperature sensitivity of $S = 293.9$ pm.K^{-1} has been reported with cascaded ring resonator structure with two ring resonators, the first ring has waveguide dimensions of 350 x 210 nm and second ring has waveguide dimensions of 450 x 210 nm [35].

The empirical formula to calculate the temperature sensitivity of the SOI structure is given by $S = d\lambda/dT = (\lambda/ng)(dneff/dT)$, where neff is the effective index of waveguide, and dneff/dT the variation of the effective index with temperature [87]. For our structures, the measurements are performed at two pairs of two different ambient temperatures (23 °C and 30 °C) and (25 °C and 35 °C) to study the effect of temperature change on the transmission spectra of the structures. For a temperature increase of 7 K and 10 K, the MR and the MDFB resonance peaks shift to higher wavelengths with a red shift of 0.48 nm and 0.69 nm with a sensitivity of a 69 pm·K^{-1}.

Fig. 3.17(a) and (b) at (25 °C and 35 °C), as well as Fig. 3.19(a) and (b) at (25 °C and 35 °C) show the experimentally measured transmission spectra of MR and MDFB with coupling lengths of $L_c = 12$ µm and 13 µm, respectively.

Fig. 3.18(a) and (b) at (23 °C and 30 °C), as well as Fig. 3.20(a) and (b) at (23 °C and 30 °C) show the experimentally measured transmission spectra of MR and MDFB with a coupling length L_c = 14 μm and 15 μm, respectively.

The dneff/dT of the channel buried waveguide (500 nm x 220 nm) has been calculated using FDTD solver (Lumerical Solutions, Inc.) to be 1.98×10^{-4} K^{-1} [88], which corresponds to a sensitivity of S = 73 pm·K^{-1}, which is in good agreement with the experimental value of S = 69 pm·K^{-1} measured from the transmittance spectra. Both MR and MDFB have same temperature sensitivity due to same design parameters, however MDFB has a better Q-factor and ER values as compared with the MR.

The limit of detection analysis can also be applied to temperature sensors. and for a resonator with a $Q = 10^6$ and a sensitivity of S = 80 pm·K^{-1}, the thermal limit of detection (LOD) is comparable to thermistors. The relation to calculate the thermal limit of detection sensor is LOD = λ/ (Q.S) where, λ is the operating wavelength, Q the Q-factor of the resonator, and S the sensitivity of resonator. For a sensitivity of S = 69 pm.K^{-1}, an operating wavelenth of λ = 1550 nm, and quality factors $Q = 4x10^4$ for MR and $Q = 5x10^4$ MDFB with Lc = 15 μm (from Table 2), we can observe improvement in LOD from 0.7 K to 0.5 K.

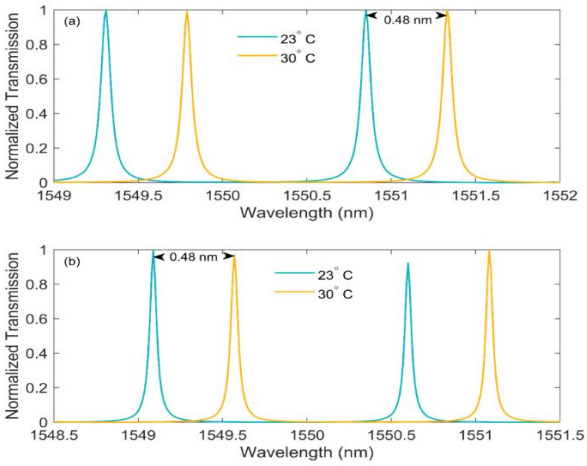

Figure 3-17 Experimentally measured MR spectrum of (a) L_c = 14 µm and (b) L_c = 15 µm at 23 ºC and 30 ºC.

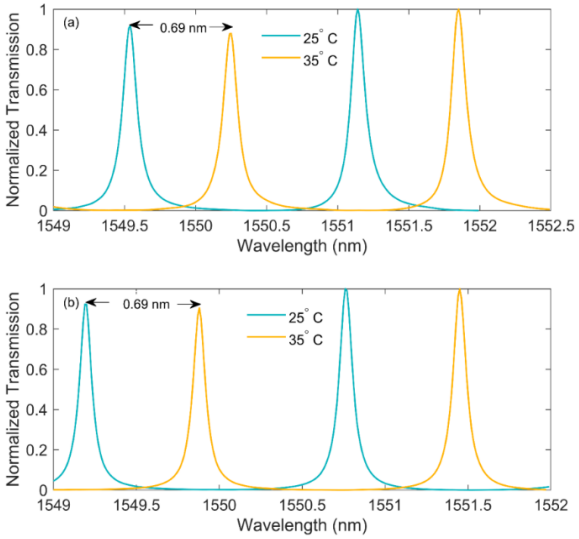

Figure 3-18 Experimentally measured MR spectrum of (a) L_c = 12 µm and (b) L_c = 13 µm at 25 ºC and 35 ºC.

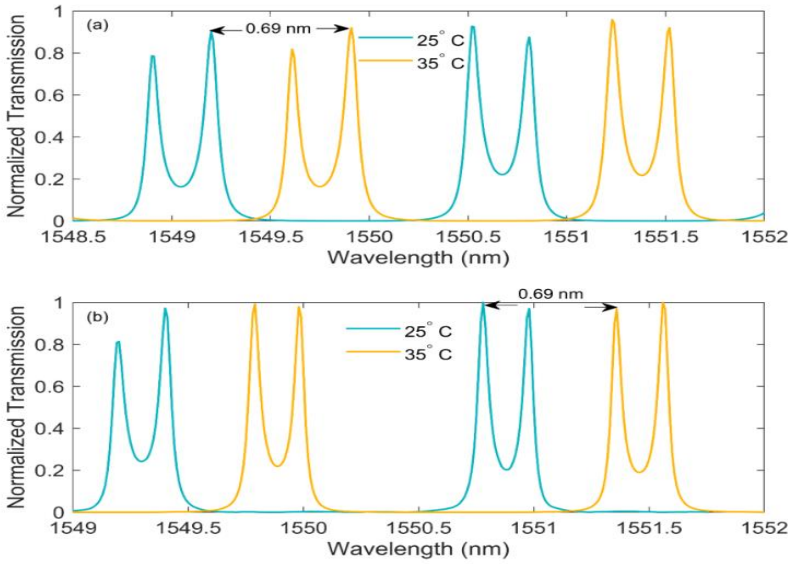

Figure 3-19 Experimentally measured MDFB spectrum of (a) L_c = 12 µm and (b) L_c=13µm at 25 ^oC and 35 ^oC

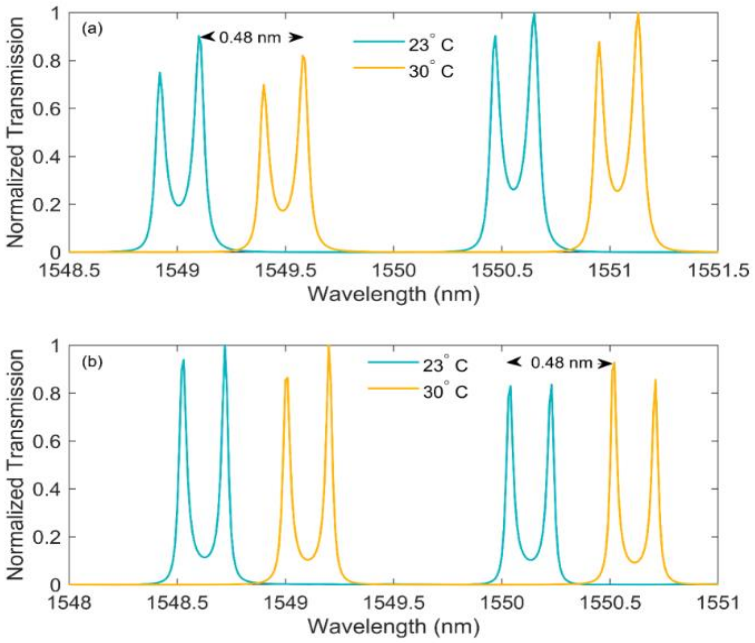

Figure 3-20 Experimentally measured MDFB spectrum of (a) L_c = 14 µm and (b) L_c=15µm at 23 ^oC and 30 ^oC.

3.6 Antisymmetric Meandering Distributed Feedback Lightwave Circuits

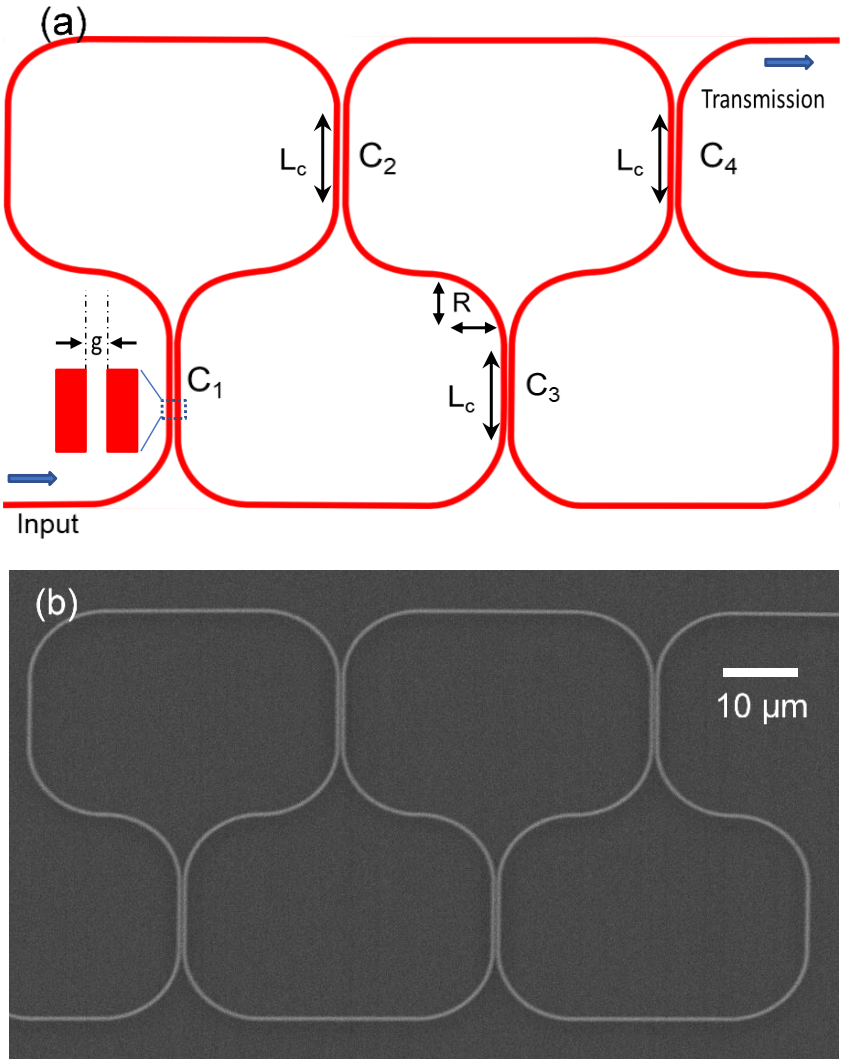

Figure 3-21 (a) Schematic and (b) SEM of the AMDFB structure with four directional couplers. There are four identical DCs which are named C1-C4. The gap 'g' between two Si waveguides with length Lc in DCs is 200 nm. The bending radius of curvature 'R' is 10 µm. . SEM image of AMDFB structure with Lc = 10 µm is presented here.

Electromagnetic induced transparency (EIT) phenomenon has gained lot of interest due to its potential applications in slow and fast light propagation [89] , optical filtering [90], quantum computing applications [91], high-sensitivity biochemical sensing [92] and non-linear optics [93]. EIT is an atomic phenomenon [94], which occurs due to quantum level interactions of light with atoms and as a result light passes through the medium rather being absorbed by the atoms [95-96]. EIT-like phenomenon can also occur in photonic resonator structures due to coherent interference of the coupled resonators [97]. Various photonic structures have demonstrated classical all-optical analogies to EIT-like spectral behavior, i.e., microrings setup with coherent interference between two indirectly coupled microring resonators [98] , whispering-gallery mode resonators [99-100], photonic crystal waveguides and microcavities [101-102], as well as plasmonic structures and metamaterials [103].

EIT phenomenon has also been studied in monolithic meandering waveguide (MW) silicon-on-insulator (SOI) structures. The reported quality(Q)-factor and extinction ratio (ER) of EIT-like peaks in MW SOI structures with four directional couplers (DCs) are 7.6×10^3 and 28 dB, respectively [104] and in a MW resonator consisting of two MW structures with two DCs, values are 2.8×10^4 and 29 dB, respectively [105].

Here, we present a MW structure, which has four DCs with optimized EIT-like spectral responses. One meandering loop mirror (MLM) and antisymmetric meandering resonator (AMR) are connected to form an AMDFB structure [106]. EIT-like spectral response with high Q-factor on the order of 4.5×10^4 has been studied in a

MW SOI structure with four DCs. In the start, we discuss the design parameters of AMDFB structure and the SOI fabrication process.

In the next section, we compare the numerically simulated and experimentally measured spectral responses. We have discussed the spectral response of structures with DC coupling constants C values of $0.09 < C < 0.51$. The C value is adjusted by changing the DC coupling length Lc. Mode splitting is observed in the AMDFB transmission spectra at C = 0.09. We can observe the EIT-like peaks at C = 0.24, and the Q-factor of the peaks increases as C increases. EIT-like peak with the high Q-factor on the order of $4.5x10^4$ is observed at C = 0.51. The numerically simulated and experimentally measured spectra show good agreement. The AMDFB structure shows promise for applications as optical filters in wavelength division multiplexing (WDM) and as optical sensors in optical diagnostics.

3.6.1 Design and Fabrication

For the design and simulation of the AMDFB structures, we used photonic software package Mode (Lumerical Solutions Inc.) for optimizing the straight and bend waveguide parameters, FDTD (Lumerical Solutions Inc.) to obtain the s-parameters of the straight waveguide, bend waveguides, and DCs. The individual components s-parameters are then imported and assembled in Interconnect (Lumerical Solutions Inc.) to observe the response of the complete structure, and obtain the transmission spectra. The optimized AMDFB structures are then transferred to a layout package (KLayout) for control of the semiconductor processing equipment.

Structure under study is called asymmetric as input and output have odd reflection symmetry. The input is provided from the lower left side and the output is detected from the upper right side of the structure, as shown in Figure 1(a). The scanning electron microscope (SEM) image is shown in Figure 1(b). The structure is drawn using a single TE mode SOI waveguide, which couples to itself at four DC points. There are four identical directional couplers (DCs), with identical coupling constants, C, in the structure. The naming nomenclature has been adopted to specify the structures, i.e., AMDFB10 means the AMDFB structure, where every DC length is R = 10 μm. Radius 'R' of the bends is 10 μm in every design, even if the DC length changes. The gap 'g' between the two waveguides in the coupling region is g = 200 nm. DC's (C1 and C4) are connected to the input and output waveguide, respectively and DC's C2 and C3 are in the middle of the structure. As we change the DC coupling length Lc, the coupling constant C changes as well. The coupling constant C values are provided in Table 1.

Table 3-4 Directional couplers (DC) coupling constants C for for the AMDFB of Figure 1(a) at 1550 nm.

DC coupling length Lc (μm)	DC coupling constant C
5	0.09
10	0.24
14	0.39
15	0.43
20	0.63
25	0.81
30	0.94
35	0.99

The design of our structures is based on the previously analyzed model of the AMDFB structure [107]. The MLM is the base structure of the AMDFB and the

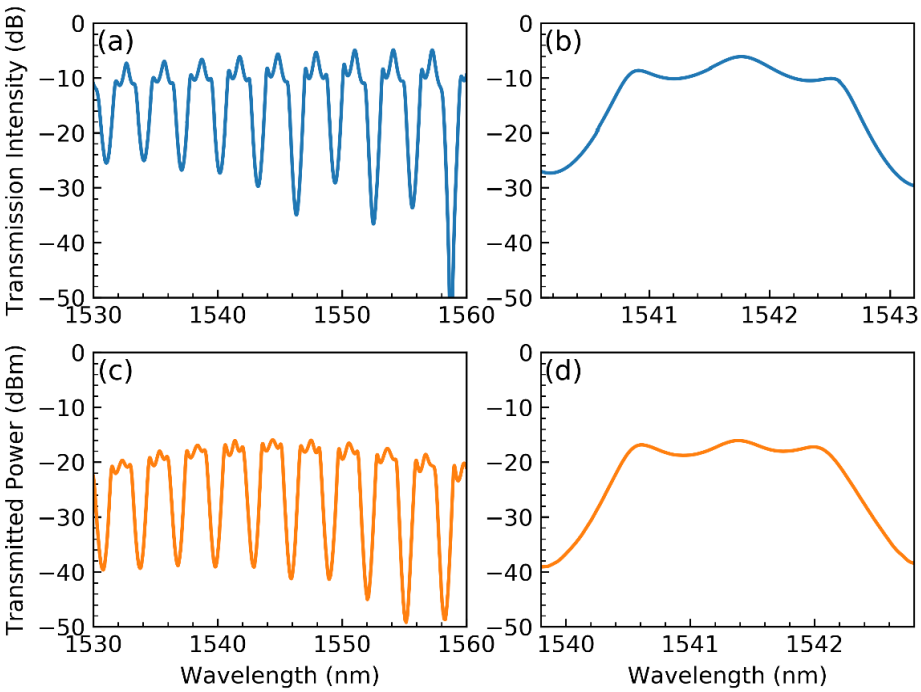

Figure 3-22 : (a), (c) Simulated and (b), (d) measured spectrum of an AMDFB structure with same coupling ratios for a coupling length of 5 micrometers around 1530 -1560, and 1541 nm, respectively. The transmission spectra show a Rabi split of the resonances.

transmittance of the AMDFB varies with the change in the coupling constant C. The MLM has maximum transmittance, when C = 0 or C = 1 and minimum transmittance (maximum reflectance) when C = 0.5. MLM output varies between 0% and 100% for other C values.

For a waveguide with a cross-section of 500 nm x 220 nm, a bending waveguide of 10 µm radius can provide a relatively low bending loss for TE mode, but not for TM mode. In order to obtain the same bending loss for the TM mode as the one of the TE mode, the necessary bending radius for the TM mode should be much larger than

10 μm [108]. However, since we are only using the TE mode, and not the TM mode, we designed our SMDFB structures only for the TE mode.

3.6.2 Numerical Simulations, Experimental Measurements, and Discussion

We present AMDFB spectral response for DC coupling lengths L_c of 5, 11, 14 and 17 μm, which correspond to coupling constants C varying from 0.09 to 0.51. These designs with coupling lengths L_c = 5, 11, 14 and 17 μm and total loop lengths of 187 μm, 211 μm, 223 μm, and 235 μm, with a group index of 4.2, results in free spectral ranges (FSRs) of $\Delta\lambda = \lambda^2/n_gL$ of 3.06 nm, 2.71nm, 2.57 nm, and 2.43 nm, which correlate well with the numerically calculated and experimentally measured transmission spectra.

The best numerically calculated and experimentally measured insertion loss for the TE polarized grating couplers are respectively -2.2 dB and -4.1 dB per a pair of input and output grating couplers connected with a TE polarized single mode waveguide [63]. For our case, a typical numerically calculated and experimentally measured insertion loss for the de-embedded structure, with just the input and the output TE polarized grating couplers, connected with a TE polarized single mode waveguide, the minimum insertion loss is respectively -5 dB, and -15 dBm (not shown). The discrepancy between the numerically calculated and experimentally measured values may be due to optical misalignment of the input and output fibers, as well as fabrication tolerances.

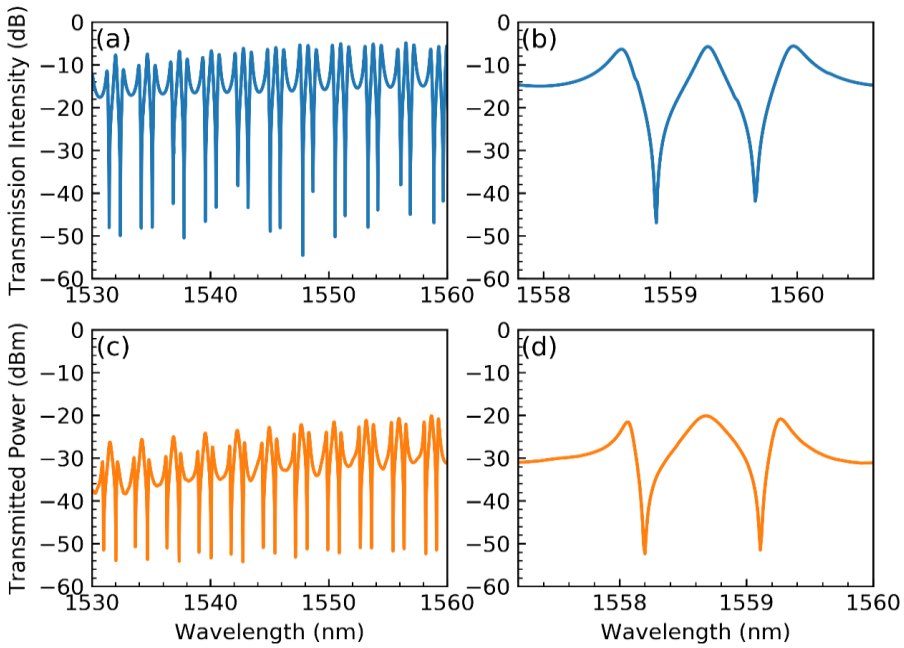

Figure 3-23(a), (c) Simulated and (b), (d) measured spectrum of an AMDFB structure with same coupling ratios for a coupling length of 11 micrometers around 1530 -1560, and 1558 nm, respectively. EIT-like peaks are present in both numerically simulated and experimentally measured results.

The numerically calculated and experimentally measured transmission of the AMDFB5 (with a coupling length of Lc = 5 μm) in the 1530 – 1560 nm region is plotted in Fig. 3.22 (a) and (b). The numerically simulated and experimentally measured spectra show mode splitting. This spectral response can be useful in filtering application. Single FSR of numerically simulated and experimentally measured spectra is plotted in Fig. 3.22(c) and (d), respectively. We can observe ER of 29 dB in simulated spectra, whereas, ER of 25 dB is observed for experimentally measured data. The transmission spectra show a Rabi split of the resonances. The numerically calculated and experimentally measured insertion loss for the AMDFB structure with

coupling length L_c = 5 µm are respectively -5 dB and -16 dBm, as shown in Figure 3.22(a) to Figure 3.22(b). The discrepancy, between the numerically calculated and experimentally measured values for the AMDFB structure, correlate well with the values of the above described de-embedded structure.

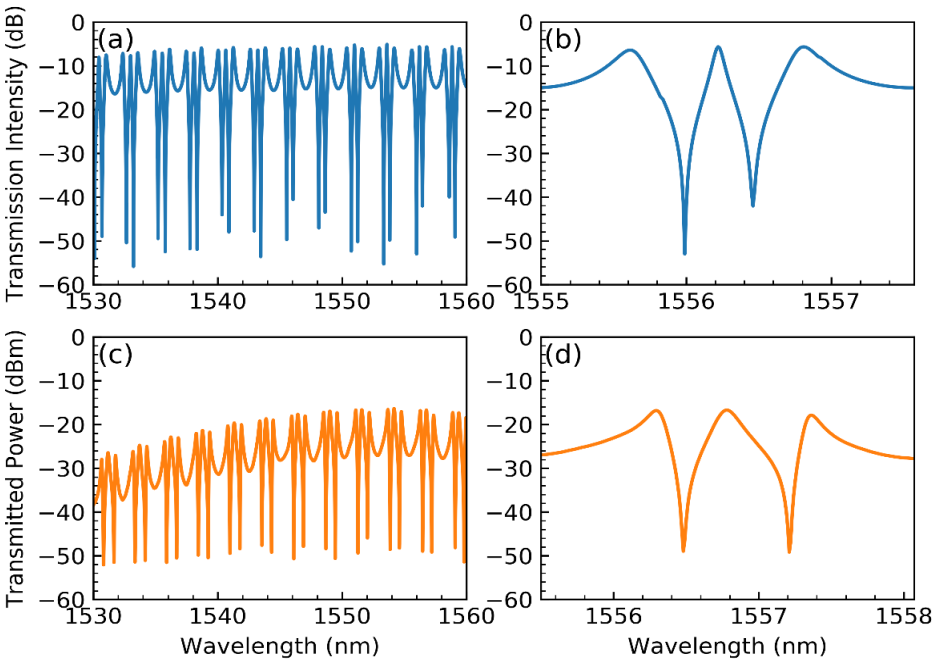

Figure 3-24 (a), (c) Simulated and (b), (d) measured spectrum of an AMDFB structure with same coupling ratios for a coupling length of 14 micrometers around 1530 - 1560, and 1557 nm, respectively.

The numerically calculated and experimentally measured transmission of the AMDFB11 (with a coupling length of L_c = 11 µm) in the 1530 – 1560 nm region is plotted in Fig. 3.23 (a) and (b). The coupling constant C increases from 0.09 to 0.27 by increasing L_c from 5 µm to 11 µm. We can observe EIT-like peaks in both numerically simulated and experimentally measured results. The numerically simulated and experimentally measured single FSR around 1559 nm is plotted in

Fig. 3.23(c) and (d), respectively. The simulated EIT-like peak in Fig.3.23(c) shows ER of 33 dB and linewidth of 0.15 nm which corresponds to Q-factor of $1x10^4$. The experimentally measured EIT-like peak in Fig.3.23(d) shows ER of 32 dB and linewidth of 0.23 nm which corresponds to Q-factor of $7x10^3$. The numerically calculated and experimentally measured insertion loss for the AMDFB structure with coupling length L_c = 11 μm are respectively -5 dB and -20 dBm, as shown in Figure 3.23(a) to Figure 3(b). The discrepancy, between the numerically calculated and experimentally measured values for the AMDFB structure, correlate well with the values of the above described de-embedded structure.

The numerically calculated and experimentally measured transmission of the AMDFB14 (with a coupling length of L_c = 14 μm) in the 1530 – 1560 nm region is plotted in Fig. 3.24 (a) and (b). The coupling constant C = 0.39 at all directional couplers with L_c =14 μm. We can observe EIT-like peaks Q-factor increase with increasing C in both numerically simulated and experimentally measured results. The numerically simulated and experimentally measured single FSR around 1554 nm is plotted in Fig. 3.24(c) and (d), respectively. The simulated EIT-like peak in Fig.3.24(c) shows ER of 36 dB and linewidth of 0.1 nm which corresponds to Q-factor of $1.5x10^4$. The experimentally measured EIT-like peak in Fig.3.25(d) shows ER of 32 dB and linewidth of 0.16 nm, which corresponds to Q-factor of $1x10^4$. The numerically calculated and experimentally measured insertion loss for the AMDFB structure with coupling length L_c = 14 μm are respectively -5 dB and -16 dBm, as shown in Figure 3.24(a) to Figure 3.24(d). The discrepancy, between the numerically

calculated and experimentally measured values for the AMDFB structure, correlate well with the values of the above described de-embedded structure.

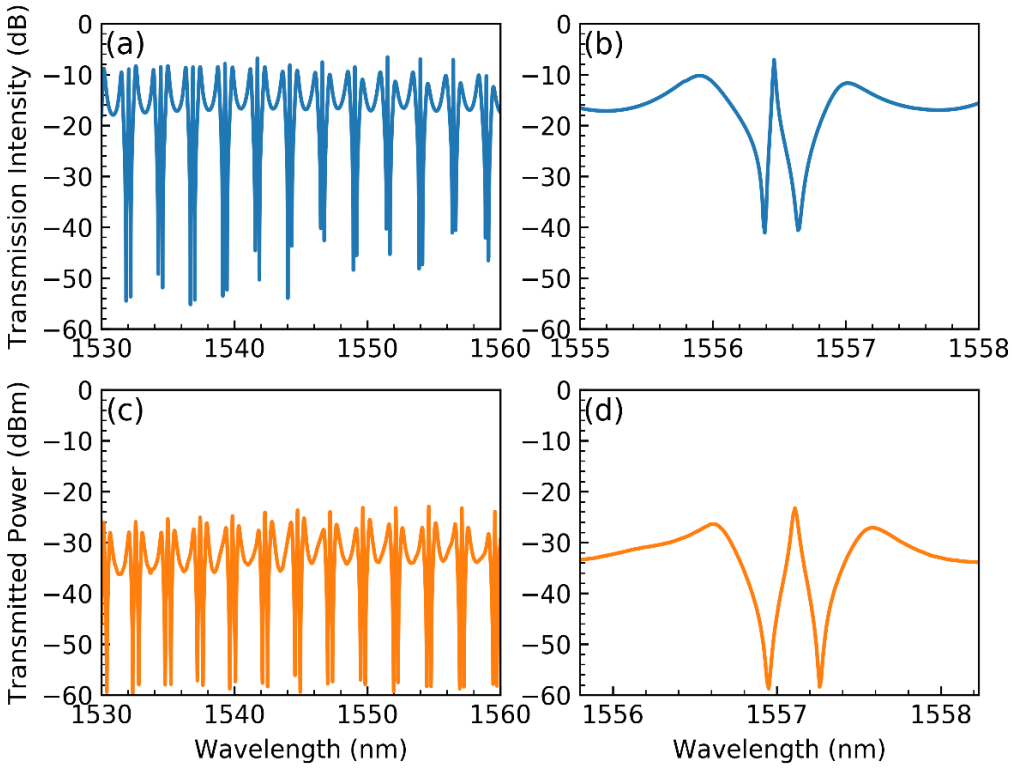

Figure 3-25 (a), (c) Simulated and (b), (d) measured spectrum of an AMDFB structure with same coupling ratios for a coupling length of 17 micrometers around 1530 - 1560, and 1557 nm, respectively.

The numerically calculated and experimentally measured transmission of the AMDFB17 (with a coupling length of L_c = 17 μm) in the 1530 – 1560 nm region is plotted in Fig. 3.25 (a) and (b). The coupling constant C = 0.51 at all coupling regions with L_c =17 μm. The EIT-like peaks get narrower by increasing C in both numerically simulated and experimentally measured results. The numerically simulated and experimentally measured single FSR around 1557 nm is plotted in Fig. 3.25(c) and (d), respectively. The simulated EIT-like peak in Fig.3.25(c) shows ER of 33 dB and

linewidth of 0.023 nm which corresponds to Q-factor of $6.8x10^4$. The experimentally measured EIT-like peak in Fig.3.25(d) shows ER of 33 dB and linewidth of 0.035 nm which corresponds to Q-factor of $4.5x10^4$. The numerically calculated and experimentally measured insertion loss for the AMDFB structure with coupling length Lc = 17 μm are respectively -7 dB and -23 dBm. The discrepancy, between the numerically calculated and experimentally measured values for the AMDFB structure, correlate well with the values of the above described de-embedded structure.

In Figures 3.22-3.25 (c-d), we can observe the tuning of EIT-like peak by changing the L_c from 11 μm to 17 μm, which results in DC coupling constants C ranging from 0.27 to 0.51. The EIT-like spectral response is broader in Figure 2(c-d), however the Q-factor of the EIT-like peak increases with increasing L_c. When L_c = 17 μm, the EIT-like peak has an ER of 33 dB, with a FWHM of 35 pm, resulting in a Q-factor on the order of 5×10^4.

The EIT-like peak is more asymmetric for short coupling lengths both in the simulations and experimental spectra. The possible reason for the asymmetry of the EIT-like peak might be due to the phase imbalance of the AMDFB structure [109]. EIT-like peak could be affected by the slight detuning of the coupled resonators because of radius differences [110]. As a result, the asymmetry of the EIT-like peak could be controlled through fabrication process optimization and engineering the coupled resonator geometries. For example, EIT-like spectral asymmetry can be achieved by detuning coupled resonators [110].

In this section, we have presented and discussed the numerically simulated and experimentally measured transmission spectra for the AMDFB structures with four DCs. The coupling constant C is changed by changing the DC coupling length Lc. In the AMDFB design, the coupling is identical at all the DCs, which results in a clean spectral response with clearly identifiable FSRs.

For coupling constant $0.24 < C < 0.51$, EIT-like peaks are observed, and adjusted by varying the DC length Lc. Mode splitting spectral behavior shows an extinction ratio of 25 dB for the experimental measurements for a DC with a length of Lc = 17 μm. We studied the spectral response of structures with coupling constants values of $0.09 < C < 0.51$. The C value is adjusted by changing the directional coupler length L_c. Mode splitting is observed in the structures' transmission spectra at C = 0.09. We observe EIT-like peaks at C = 0.24, and the Q-factor of the peaks increases as C increases. The numerically calculated and experimentally measured insertion loss for the structures' with coupling length L_c = 14 μm are respectively -5 dB and -16 dBm, including the grating couplers. EIT-like peaks show an extinction ratio of more than 33 dB. Electro-magnetically induced transparency-like peaks show a Q-factor of $4.5x10^4$ at C = 0.51.

All in all, AMDFB structures with mode splitting and EIT-like peaks spectral responses can find applications as optical filters and optical switches in WDM and data networks, as well as optical sensors in optical diagnostics.

3.7 Symmetric Meandering Distributed Feedback Lightwave Circuits

In this section, we present a TE polarized SOI based DMW structure, which has five directional couplers (DCs) with optimized Fano lineshape and EIT-like spectral responses. Three MLM units are joined and coupled together to form the SMDFB structure. In the regular meandering distributed feedback (MDFB) structure, there are MLMs stacked and coupled to each other only from the bottom [111]. The SMDFB structure is different from the MDFB in the sense that, MLMs are stacked and coupled to each other from the top, as well as the bottom. There are n DCs for n MLMs in the MDFB, whereas there are 2n-1 DCs for n MLMs in the SMDFB. In the design, the coupling constant C is controlled by varying the coupling length Lc of the DCs. We can observe and optimize Fano lineshapes, and EIT-like lineshapes by varying the coupling length Lc in the SMDFB structure, as analyzed previously, using the transfer matrix method (TMM) [111].

In meandering waveguide integrated silicon photonics structures clockwise (CW) and counterclockwise (CCW) propagation of light happens, when DC coupling constant C value is between 0 and 1. A resonator can be made by coupling two MLM's together, which will consist of two DC's. Further resonator types can be achieved by coupling more resonators together, which will increase the number of DC's in the structure. When we increase the DC's in the structure, the number of coupled resonators also increase, and if resonators with similar modes are coupled, these modes split, and we can observe this splitting in the transmission. Mode splitting in meandering waveguide structures consisting of more than two MLM's has been presented previously [112].

By controlling the DC coupling parameters, we can adjust the Fano resonances and control EIT-like peaks [113].

Fano lineshapes and the EIT-like lineshapes are studied in a DMW structure with five DCs. We first discuss the design parameters of the SMDFB structure, and the SOI fabrication process. Then, the transmission spectra, obtained by the numerical simulations, are compared with the experimental measurements.

Fano lineshapes with mode splitting is observed at coupling constant **C** of 0.24. For coupling constant **C** ~ 0.78, EIT-like peaks are observed, and adjusted by changing the coupling length Lc. Fano lineshapes have extinction ratios (ERs) of more than 26 dB and slope ratio (SR) of 368 dB/nm. EIT-like peaks have a quality factor (Q-factor) on the order of 5×10^4. The experimentally measured and the numerically calculated spectra show good agreement. The numerically calculated and experimentally measured insertion loss for the SMDFB structure with coupling length Lc = 10μm are respectively -5 dB and -17 dBm, including the grating couplers. The SOI based TE polarized SMDFB structure shows promise for applications as optical switches, and optical filters in wavelength division multiplexing (WDM) and optical switching, as well as optical sensors in optical diagnostics using silicon photonics.

3.7.1 Structural Design

Figure 3.26 (a) shows the schematic diagram of SMDFB structure. A scanning electron microscope (SEM) image of the SMDFB is shown in Figure 3.26 (b). The SMDFB structure can be divided in two parts, i.e., the top and the bottom.

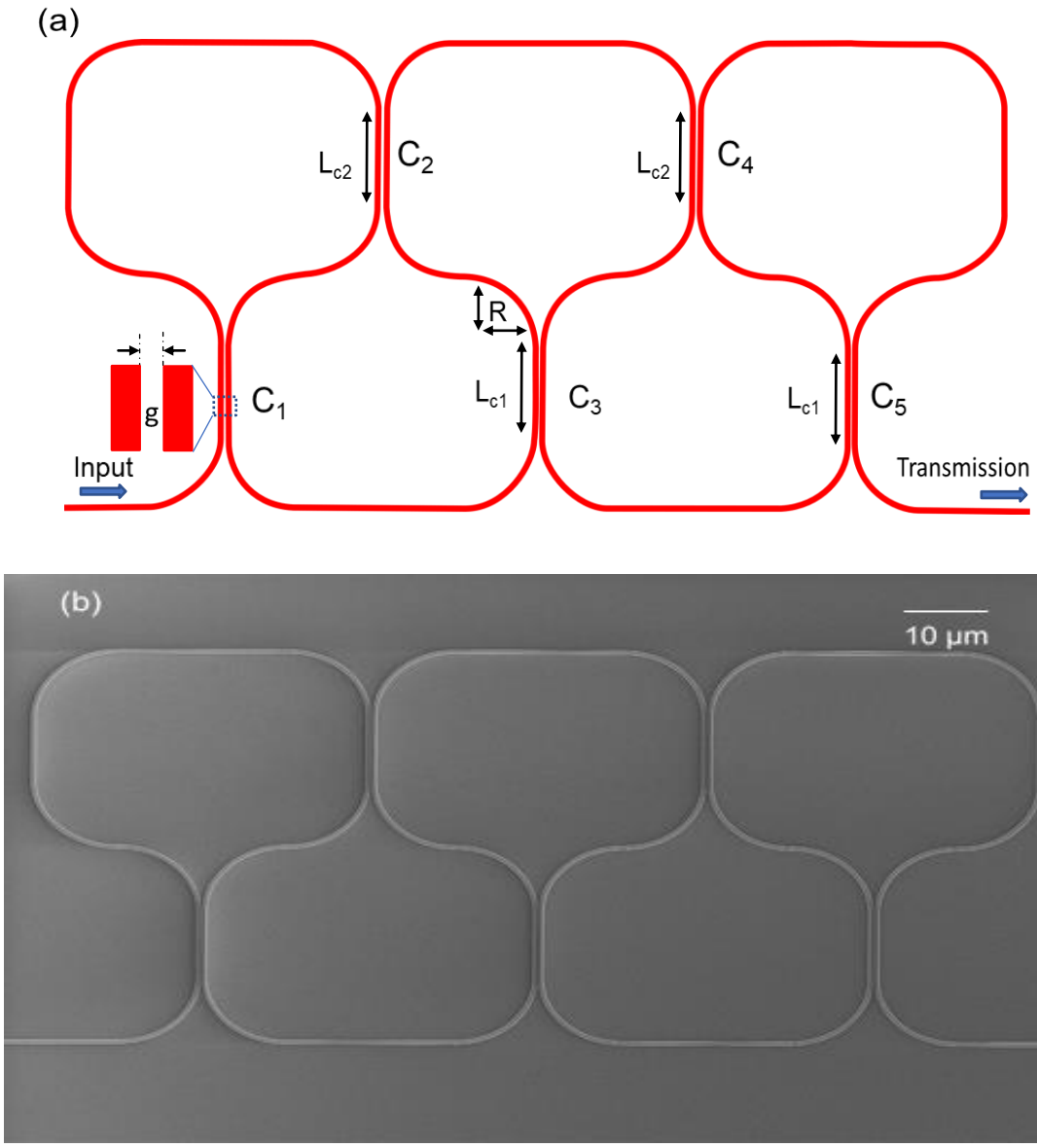

Figure 3-26 (a) The schematic, and (b) the SEM of the SMDFB structure with identical coupling constants.

The bottom has three DCs with coupling constants C1, C3, and C5, with coupling lengths L_{c1}, and the top has two DCs with coupling constants C2 and C4, with coupling lengths $L_{c2,}$ respectively. The DC lengths L_{c1} and L_{c2} are kept identical in this work, i.e., $L_{c1} = L_{c2}$ and are varied from 10 to 30 µm for a design adjustable spectral

response in the near-infrared (near-IR) telecommunication band from 1500 to 1600 nm.

3.7.2 Simulations, Measurements, and Discussion

The schematic and the SEM images of the SMDFB structure are shown in Figure 3.26(a) and Figure 3.26(b), respectively. The SMDFB structure has uniform DC coupling constants. The SMDFB with L_c = 10 μm simulated and experimental spectral transmittance from 1540 - 1560 nm is plotted in Figure 3.27 (a) and (b), respectively. The transmission spectra show a split of the Fano lineshape resonances. The free spectral range (FSR) of the SMDFB can be calculated using the geometric loop length L and the group index n_g of the TE mode SOI waveguide, as the following $\Delta\lambda_{FSR} = \lambda^2 / Ln_g$. The SMDFB with L_c = 10 μm has a total geometric loop length of L = 207 μm and with a group index of n_g = 4.2 result in an FSR of 2.76 nm, which correlates well with the numerically simulated and experimentally measured transmittance spectra.

In Figure 3.28, we can observe that, SMDFB simulated [Figure 3.29 (a, b, c, d)] and measured [Figure 3.29 (e, f, g, h)] spectral responses for L_c = 24, 25, 26, and 30 μm, with total geometric loop lengths L = 263, 267, 271, and 287 μm and a group index of n_g = 4.2 result in FSRs of 2.17, 2.14, 2.11, and 1.99 nm, which correlates well with the numerically simulated and experimentally measured transmittance spectra. There are two EIT-like peaks on the sides of the passband in the middle of the FSR.

The best numerically calculated and experimentally measured insertion loss for the TE polarized grating couplers are respectively -2.2 dB and -4.1 dB per a pair of input and

output grating couplers connected with a TE polarized single mode waveguide [63]. For our case, a typical numerically calculated and experimentally measured insertion loss for the de-embedded structure, with just the input and the output TE polarized grating couplers, connected with a TE polarized single mode waveguide, the minimum insertion loss are respectively -5 dB, and -15 dBm (not shown). The discrepancy between the numerically calculated and experimentally measured values may be due to optical misalignment of the input and output fibers, as well as fabrication tolerances.

The numerically calculated and experimentally measured insertion loss for the SMDFB structure with coupling length $L_c = 10\mu m$ are respectively -5 dB and -17 dBm, as shown in Figure 3.27(a) and (b). Also the numerically calculated and experimentally measured insertion losses for the SMDFB structure with coupling length $L_c = 24\mu m$, $25\mu m$, $26\mu m$, and 30 μm are - 5 dB, and varies between -15 dBm to -20 dBm, as shown in Figure 3.28 (a-d) and Figure 3.28 (e-h). The discrepancy, between the numerically calculated and experimentally measured values for the SMDFB structure, correlate well with the values of the above described de-embedded structure.

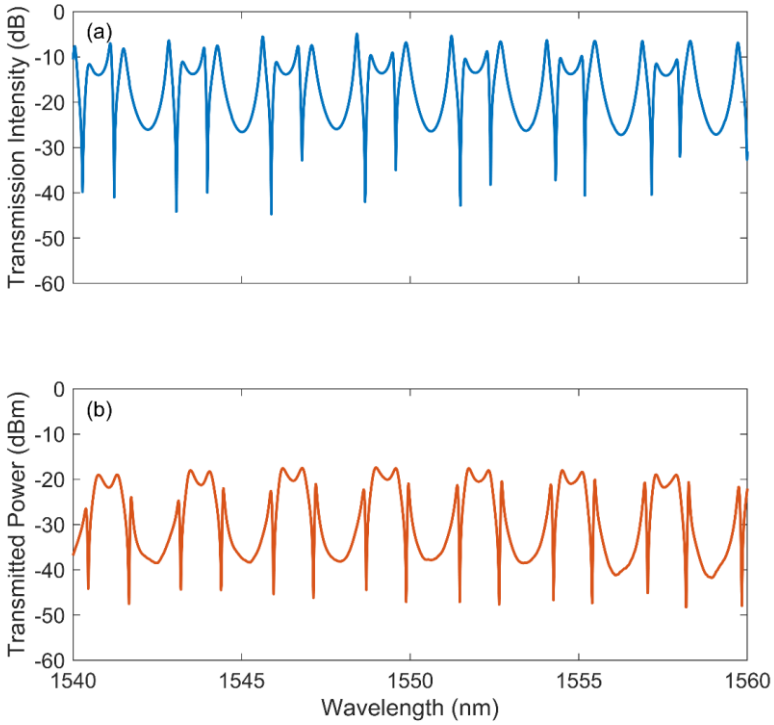

Figure 3-27 (a) Numerically simulated, and (b) experimentally measured transmission spectrum of an SMDFB structure for a DC coupling length of 10 µm. The transmission spectra show a split of the Fano lineshape resonances.

In Figure 3.28(i, j, k, and l), we can observe the tuning of EIT-like peak by changing the L_c from 24 µm to 30 µm, which results in DC coupling constants C ranging from 0.78 to 0.94. The EIT-like spectral response is broader in Figure 3.28 (c), however the Q-factor of the EIT-like peak increases with increasing L_c. When L_c = 30 µm, the EIT-like peak has an ER of 19 dB, with a FWHM of 27 pm, resulting in a Q-factor of 5 x 10^4. The EIT-like peak is more asymmetric for short coupling lengths both in the simulations and experimental spectra. The possible reason for the asymmetry of the EIT-like peak might be due to the phase imbalance of the SMDFB structure [114].

EIT-like peak could be affected by the slight detuning of the coupled resonators

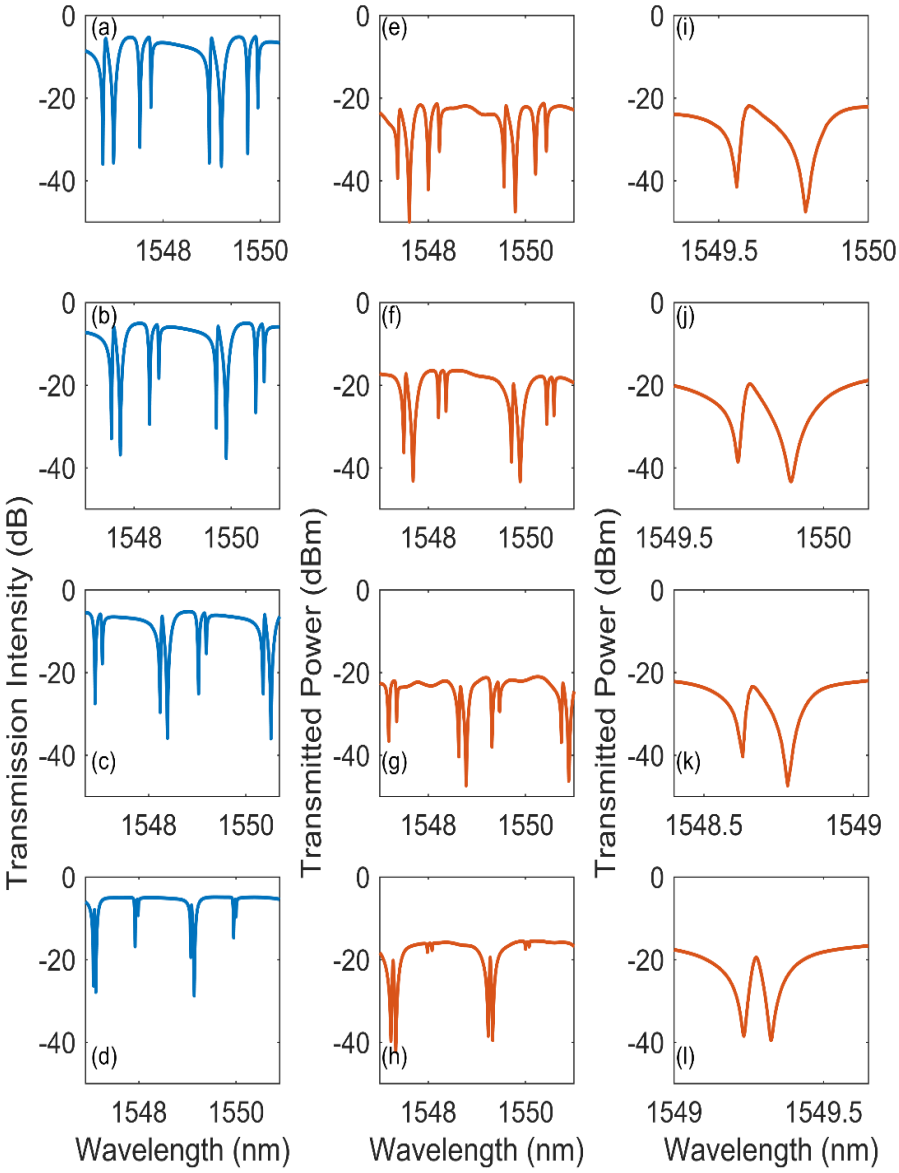

Figure 3-28: (a), (b), (c), (d) Numerically simulated and (e), (f), (g), (h) experimentally measured transmission spectra of the SMDFB structure for a coupling length of 24, 25, 26, and 30 μm. (i), (j), (k), (l) Experimentally measured transmission spectrum of EIT-like peak development around 1549 nm with increasing DC coupling constant. The Q-factor of these EIT-like peaks increases as C increases to 0.94.

because of radius differences [115].

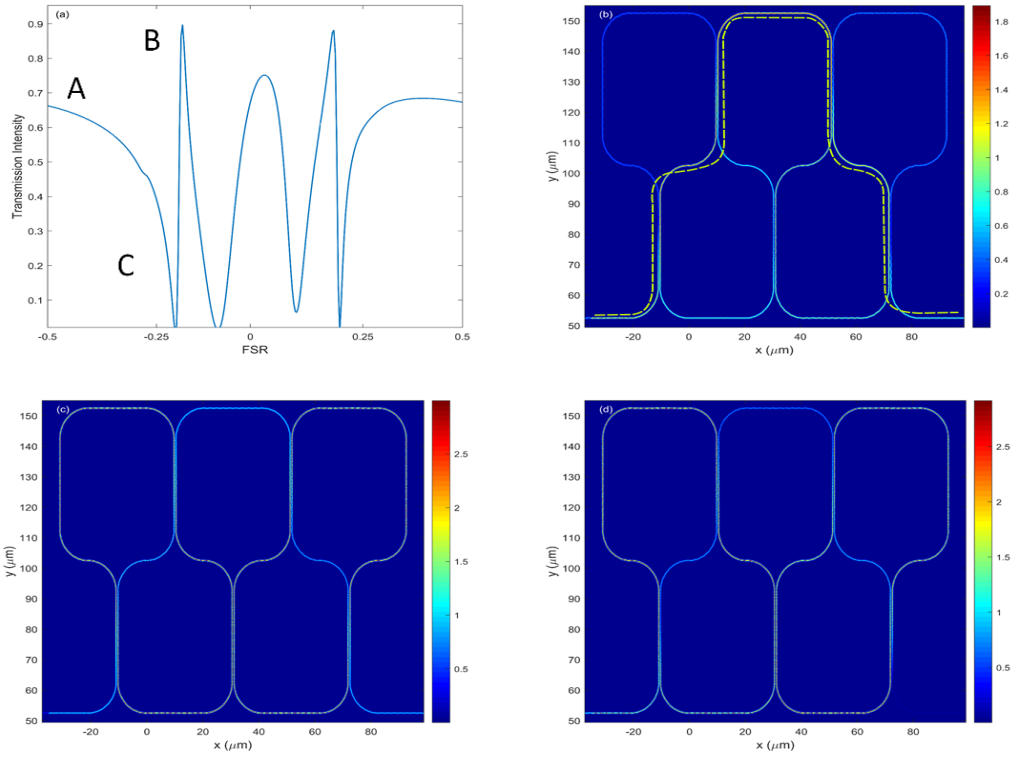

Figure 3-29 (a) 2D FDTD simulated single FSR spectral response of SMDFB structure with L_c = 30 μm, which shows two EIT-like peaks and (b) electric field distribution in SMDFB structure corresponding to non-resonance point A. We can observe dotted path along which electric field is stronger (c) electric field distribution in SMDFB structure corresponding to resonance point B. We can observe electric field is stronger in rest of the structure as compared to figure (b) and (d) electric field distribution in SMDFB structure corresponding to minimum transmission point C.

As a result, the asymmetry of the EIT-like peak could be controlled through fabrication process optimization and engineering the coupled resonator geometries. For example, EIT-like spectral asymmetry can be achieved by detuning coupled resonators [110].In this section, we discussed the numerically simulated and the experimentally measured transmission spectra for the SMDFB structures with five DCs. The coupling constant C is changed by changing the DC coupling length L_c. In

the SMDFB design, the coupling is identical at all the DCs, which results in a clean spectral response with clearly identifiable FSRs.

Chapter 4 : Study of silicon meandering distributed feedback structures as a model system for biological ligands

This chapter discusses the application of the integrated structures discussed in previous chapter as refractive index biosensing structures. Some definitions and FOMs were introduced in Chapter 1.

We have performed the bulk sensing simulations for the AMR, the MR , the MDFB, and the SMR structures. The cladding is water (H_2O) in all the simulations (previous simulations and experimental results have SiO_2 as cladding) and refractive index of cladding is changed from 1.33 to 1.34. The silicon waveguide type is rectangular with 500 nm x 220 nm dimensions.

The spectral responses of the AMR, the MR , the MDFB, and the SMR structures with change in cladding refractive are plotted in Figure 4.1, 4.2, 4.3, and 4.4 respectively. The spectral response shifts to the higher wavelength, which corresponds to sensitivity of 54 nm/RIU. The sensitivity depends on the interaction of the biomolecule layer with the light in the cladding, which can be increased by designing structures with slot and SWG waveguides. In order to use integrated photonics structures for biosensing applications, we need to integrate microfluidics channels over the structures. If we want to study specific biological ligand, we need to perform surface biofunctionalization of the waveguides to bind and study wavelength shifts due to the specific ligand.

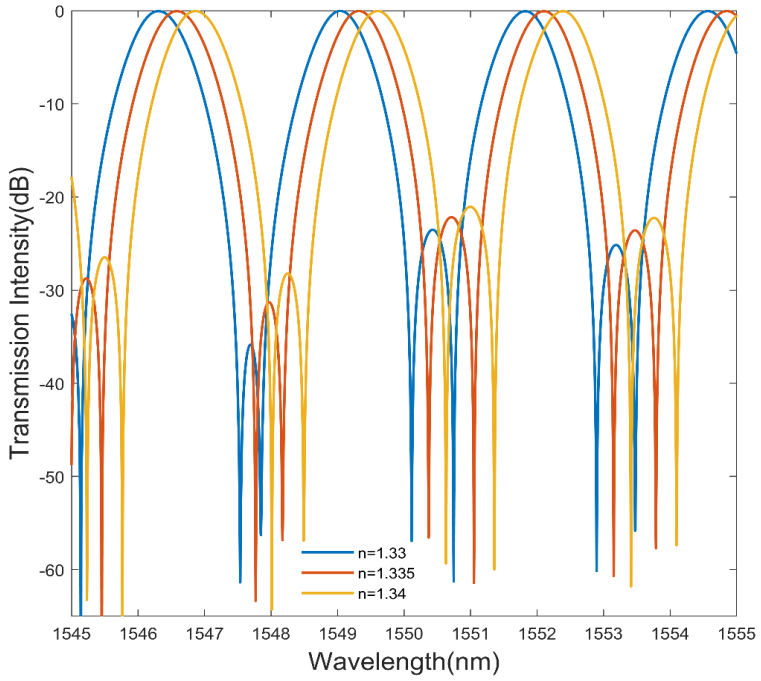

Figure 4-1 The AMR structure peaks shifts as the cladding refractive changes from 1.33 to 1.34. The simulations are performed for L_c= 10µm.

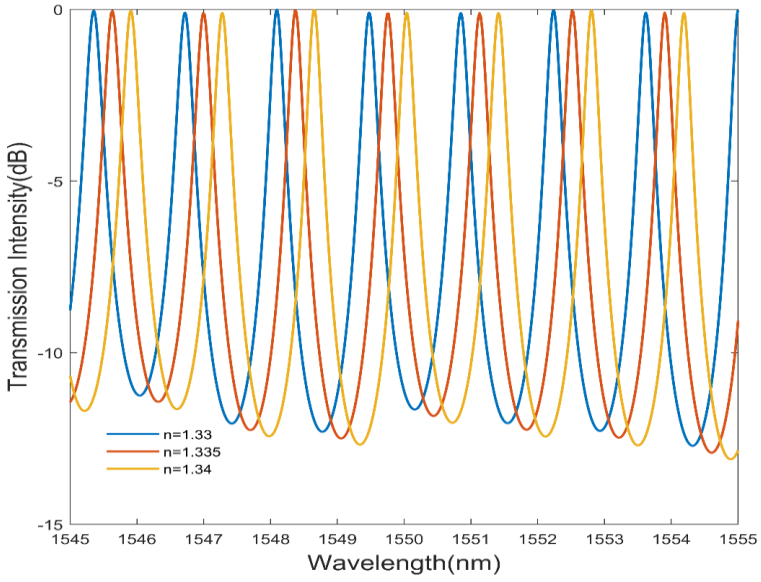

Figure 4-2 The MR structure Lorentzian peaks shifts as the cladding refractive changes from 1.33 to 1.34. The simulations are performed for L_c= 10µm.

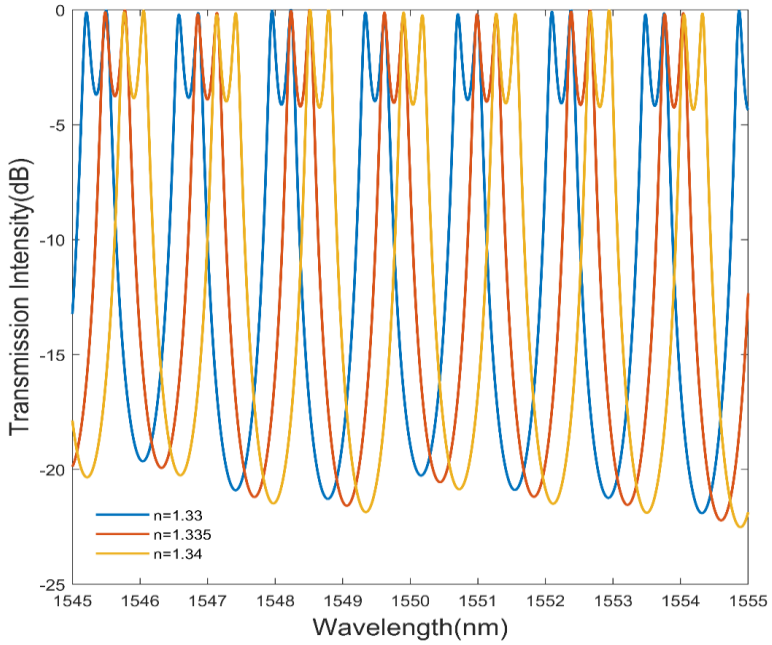

Figure 4-3 The MDFB structure mode splitting spectral response shifts as the cladding refractive changes from 1.33 to 1.34. The simulations are performed for L_c= 10µm.

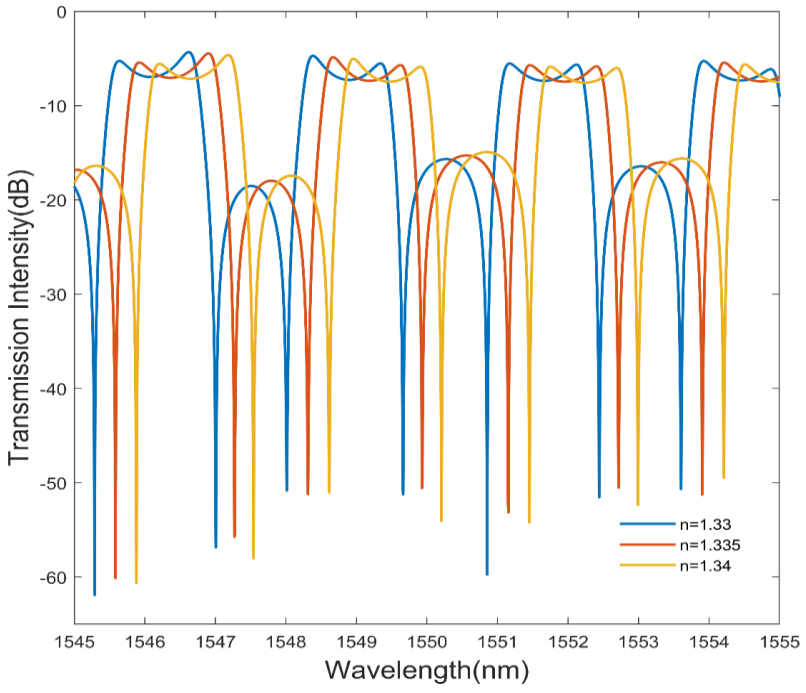

Figure 4-4 The SMR structure Fano lineshape with mode splitting shifts as the cladding refractive changes from 1.33 to 1.34. The simulations are performed for L_c = 10µm.

The layout of bulk sensing with microchannels above the sensors is shown in Figure 4.5. Microfluidics system is built on top of the silicon photonics chip using polydimethylsiloxane (PDMS) channels. Cells of one type or different types can be cultured inside the microfluidic channels [116]. In integrated photonics biosensors, amorphous fluoropolymer is also used as a cladding material [117].

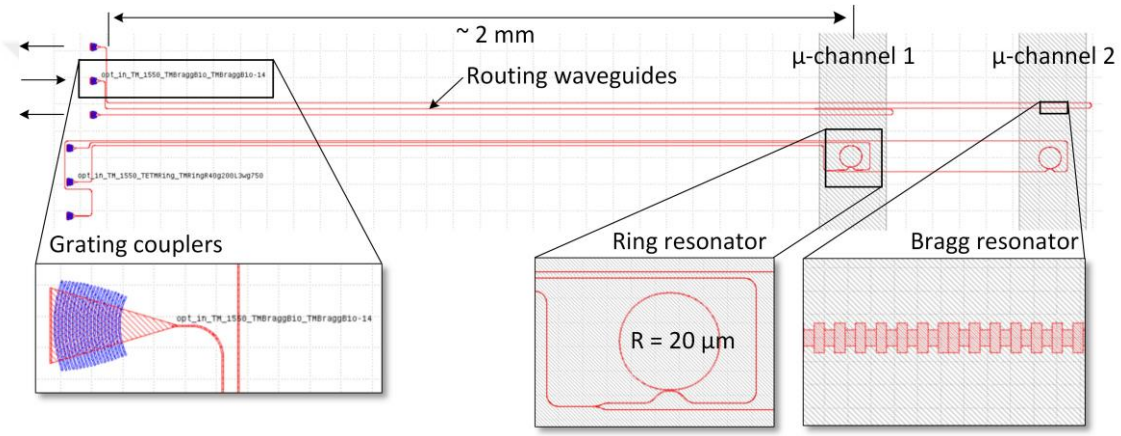

Figure 4-5 Layout of silicon photonics ring and Bragg resonator with microfluidic channels. The input and output GC's are 2 mm away from the sensors. Courtesy [118].

To make surface of waveguide respond to certain biological ligands, different methods are employed, i.e., physical adsorption, bioaffinity, and covalent attachments using functional groups, as shown in Figure 4.6.

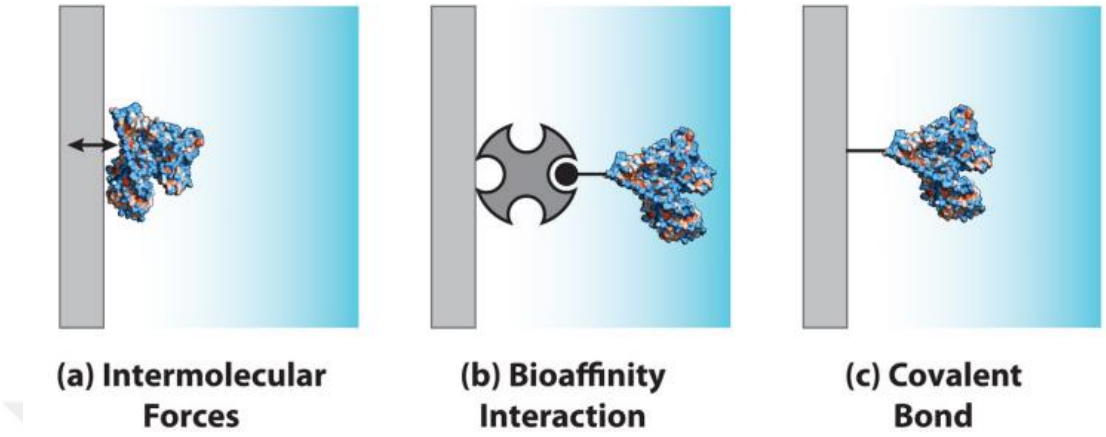

Figure 4-6 Schematic of immobilization mechanisms (a) physical adsorption, (b) bioaffinity interaction, and (c) covalent bond. Courtesy [119].

Physical adsorption or physisorption method involves transport of protein to the surface, binding to the surface because of hydrophobic and electrostatic interactions and relaxation on the surface [120].

Bioaffinity process results in stronger and highly specification protein immobilization interactions [121]. Bioaffinity interactions are ligand-receptor pairing, and are not irreversible in nature. They can be reversed by increasing temperature or chemical treatments [122].

Covalent bonds are the most frequently employed mechanism for immobilization in microfluidic assays. The functionalization of silicon ring resonator surface using covalent bonding has already been demonstrated [123].

In a similar manner, our novel MDFB silicon photonic structures can also function as biological ligands sensors, in addition to being able to function as bulk refractive index sensors.

Chapter 5 Conclusions

The aim of this thesis is to introduce new integrated photonics structures for biomedical sensing applications. For that purpose, we designed, simulated, had manufactured and measured, and analyzed three novel meandering distributed feedback (MDFB) photonic structures.

In section 3.5, we have presented numerically simulated and experimentally measured transmittance spectra of a monolithic TE mode SOI MDFB structure waveguide, which have temperature sensitivities of S= 69 pm·K^{-1}. The MDFB structure consisting of three identical cascaded MLMs connected with Si waveguides of length L1 = 5 μm, and exhibiting spectral mode splitting, when compared with its corresponding MR, consisting of two identical MLMs. MDFB's MLMs' DCs' coupling constants are varied by changing the coupling length Lc = 10, 11, 12, 13, 14, and 15 μm. MDFB structures have shown higher Q-factors and better ERs than their corresponding MRs. For a sensitivity of S = 69 pm.K^{-1}, an operating wavelength of λ = 1550 nm, and quality factors Q = $4x10^4$ for MR and Q = $5x10^4$ MDFB with Lc = 15 μm (from Table 2), we can observe improvement in LOD from 0.7 K to 0.5 K. The meandering distributed feedback structure shows promise as an ambient temperature sensor, and the spectrally split resonance peaks have Q-factors on the order of 10^4, can also find applications in biomedical diagnostics.

In section 3.6, we reported on the design, simulation, manufacturing, spectral measurement, and spectral analysis of TE polarized SOI based AMDFB structure composed of four interlaced identical MLMs with four identical DCs. To obtain the desired spectral responses, C is adjusted between $0.09 < C < 0.51$ by changing L_c between $5\ \mu m < L_c < 17\ \mu m$. Spectral mode splitting, an insertion loss of -16 dBm, an ER of 20 dBm is observed for C = 0.09 and Lc = 5 μm. For coupling constant $0.27 < C < 0.51$, EIT-like peaks are observed, and adjusted by varying the DC length $11\ \mu m < L_c < 17\ \mu m$. The Q-factor of EIT-like peaks increase as C is increased across all DCs. An insertion loss of -16 dBm, and an ER of 32dBm are observed for C = 0.39 and $L_c = 14\ \mu m$. EIT-like peaks show a Q-factor on the order of $5x10^4$ at C = 0.51 and $L_c = 17\ \mu m$,

In section 3.7, . We have discussed, simulated, and experimentally measured spectral response of the TE polarized SOI SMDFB structure with MW coupling at five DCs. The SMDFB structure has the same coupling constants in all the MLM's. The numerically simulated and the experimentally measured transmittance spectra show good agreement with each other. The numerically calculated and experimentally measured insertion loss for the SMDFB structure with coupling length **Lc** = 10μm are respectively -5 dB and -17 dBm, including the grating couplers. Fano lineshapes with mode splitting is observed at DC coupling constant value **C** = 0.24. For coupling constant **C ~** 0.78, EIT-like peaks are observed, and adjusted by varying the DC coupling length. Fano lineshapes show an extinction ratio of more than 26 dB and slope ratio of 368 dB/nm. The SMDFB structure can have various spectral responses, i.e., Fano lineshapes, and EIT-like peaks. The EIT-like peak has a Q-factor of 5×10^4,

when **Lc** = 30 μm. The SOI based TE polarized SMDFB structures with their Fano lineshapes, and EIT-like peaks, can find application as optical sensors in optical diagnostics using silicon photonics.

We have discussed the designing, fabrication, simulation and analysis of novel integrated photonic structures in Chapter 3. The simulations in Chapter 4 show their application as bulk refractive index sensor. In addition, methods discussed in chapter 4 for immobilization of biological ligands on the sensor surface can be employed to practically use these structures for biological ligands detection. In addition to the existing integrated photonics structures, such as ring resonators and Mach Zehnder interferometers (MZIs), our novel monolithic SOI based MDFB photonic structures show promise for biosensing applications.

Appendix A Maxwell equations in a homogeneous medium

Maxwell equations in a lossless and homogeneous medium in terms of electric field E and magnetic field H can be written as:

$$\nabla \times E(r,t) = -\frac{\partial}{\partial t} B(r,t) \quad \text{(A.1)},$$

$$\nabla \times H(r,t) = \frac{\partial}{\partial t} D(r,t) \quad \text{(A.2)}.$$

where *D* represents the electrical displacement, and *B* the magnetic induction. The relationships between D, E and B, H are written as:

$$B = \mu_0 H \quad \text{(A.3)},$$

$$D = \varepsilon_o \varepsilon(r) E \quad \text{(A.4)}.$$

In (A.4), $\mu_0 = 4\pi \times 10^{-7}$ [H/m] is the vacuum permeability and $\varepsilon_o = 8.854 \times 10^{-7}$ [F/m] is the vacuum permittivity. Taking the curl of both sides of (A.1), (A.2) and solving for E and H gives:

$$\frac{1}{\varepsilon(r)} \nabla \times [\nabla \times E(r,t)] = -\frac{1}{c^2} \frac{\partial^2}{\partial t^2} E(r,t) \quad \text{(A.5)}.$$

and,

$$\nabla \times \left[\frac{1}{\varepsilon(r)} \nabla \times H(r,t)\right] = -\frac{1}{c^2}\frac{\partial^2}{\partial t^2} H(r,t) \qquad \text{(A.6)}.$$

where,

$$c = 1/\sqrt{\mu_0 \varepsilon_0}.$$

Appendix B Buried channel waveguide

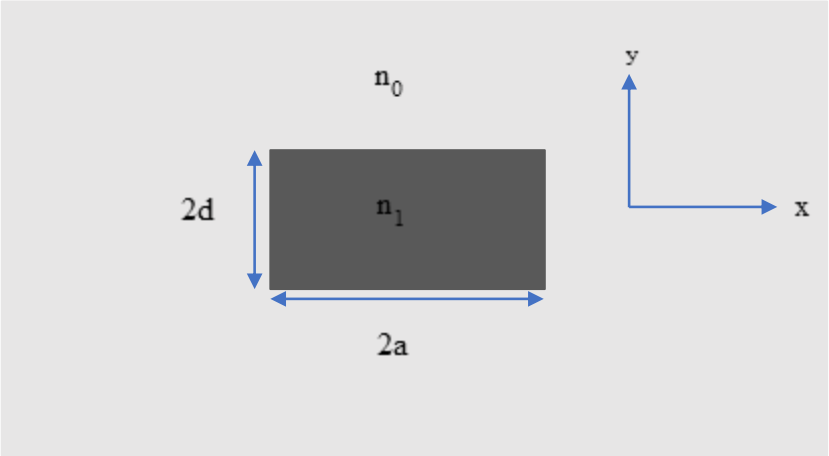

Figure B.1: Cross section of buried channel waveguide.

The modal fields in variable separable form can be written as:

$$\boldsymbol{H} = H(x,y)e^{i(\omega t-\beta z)}$$

$$\boldsymbol{E} = E(x,y)e^{i(\omega t-\beta z)} \qquad (B.1).$$

putting these expressions in Maxwell equations, we can write wave equation as,

$$\left(\frac{\partial^2}{\partial x^2}+\frac{\partial^2}{\partial y^2}\right)\boldsymbol{E} + (k^2n^2 - \beta^2)\boldsymbol{E} = 0 \qquad (B.2).$$

The propagation constant β can be expressed as

$$k_o.n_{eff} = \beta = \sqrt{k_o^2n_1^2 - (k_x^2+k_y^2)} \qquad (B.3).$$

$$n_{eff} = \beta/k_o = \frac{1}{k_o}.\sqrt{k_o^2n_1^2 - (k_x^2+k_y^2)}$$

$$n_{eff} = \beta/k_o = \sqrt{n_1^2 - [(k_x^2+k_y^2)/k_o^2]}$$

VITA

Muhammad Rehan Chaudhry attended the Crescent Model Higher Secondary School, Lahore from 1991 to 2001 for his secondary school studies. He passed the higher Secondary School Exam in Pre-Engineering studies from the Forman Christian College, Lahore in 2003. Later, he completed his Bachelor studies in Electrical Engineering at oldest and one of the prestigious engineering university of Pakistan, the University of Engineering and Technology, Lahore in 2007.

In 2013, he received a Higher Education Commission (HEC) of Pakistan Scholarship and chose Koç University, Istanbul for his graduate studies after getting accepted in M.Sc. Optoelectronics and Photonics Engineering program as a teaching and research assistant. In 2015 he received his M.Sc. Optoelectronics and Photonics Engineering from Koç University. The same year he got accepted to the Ph.D. in Biomedical Sciences and Engineering program as a teaching and research assistant at Koç University.

During his studies in Koç University Microphotonics Research Laboratory, he worked on elastic light scattering of a CO_2 laser from microspheres, and of microwaves from photonic crystals, and integrated photonics in silicon on insulator waveguides.

BIBLIOGRAPHY

[1] Technavio, “Global Point of Care (POC) Diagnostics Market 2019-2023,” (2019).

[2] L. Clark, “Monitor and control of blood and tissue oxygen tensions,” Trans. Am. Soc. Artif. Internal Organs 2, 41–46 (1956).

[3] C. C. Leland and C. Lyons, “Electrode systems for continuous monitoring in cardiovascular surgery," Annals of the New York Academy of sciences, 102(1):29–45, 1962.

[4] A. P. F. Turner, “Biosensors: sense and sensibility,” Chemical Society Reviews, 42(8):3184–3196, 2013

[5] A. Syahir, K. Usui, K. Y. Tomizaki, K. Kajikawa, H, Mihara, “Label and label-free detection techniques for protein microarrays,” Microarrays 4, 228–244 (2015).

[6] D. Thomson, A. Zilkie, J. E. Bowers, T. Komljenovic, G. T. Reed, L. Vivien, D. Marris-Morini, E. Cassan, L. Virot, J.-M. Fédéli, J.-M. Hartmann, J. H. Schmid, D.-X. Xu, F. Boeuf, P. O’Brien, G. Z. Mashanovich, and M. Nedeljkovic, "Roadmap on silicon photonics," Journal of Optics, vol. 18, no. 7, p. 073003, June 2016.

[7] D. Celo, D. J. Goodwill, J. Jiang, P. Dumais, M. Li, and E. Bernier, "Thermo-optic silicon photonics with low power and extreme resilience to over-drive," in 2016 IEEE Optical Interconnects Conference (OI) (IEEE May 2016), pp. 26–27.

[8] Y. Vlasov, "Silicon CMOS-integrated nano-photonics for computer and data communications beyond 100G," IEEE Communications Magazine 50, s67–s72 (2012).

[9] E. Ryckeboer, R. Bockstaele, M. Vanslembrouck, and R. Baets, "Glucose sensing by waveguide-based absorption spectroscopy on a silicon chip," Biomedical Optics Express 5, 1636 (2014).

[10] T. Horikawa, D. Shimura, and T. Mogami, "Low-loss silicon wire waveguides for optical integrated circuits," MRS Communications, vol. 6, no. 1, pp. 9–15, March 2016.

[11] C. Ciminelli, F. Dell’Olio, D. Conteduca, C. M. Campanella, and M. N. Armenise, "High performance SOI microring resonator for biochemical sensing," Optics & Laser Technology, vol. 59, pp. 60–67, July (2014).

[12] Z. Su, E. S. Hosseini, E. Timurdogan, J. Sun, G. Leake, D. D. Coolbaugh, and M. R. Watts, "Reduced Wafer-Scale Frequency Variation in Adiabatic Microring Resonators," in Optical Fiber Communication Conference (OSA March, 2014), pp. 1-3.

[13] L. Liu, T. Yang, and J.-J. Dong, "Microwave photonic filter with a continuously tunable central frequency using an SOI high-Q microdisk resonator," Chinese Physics B, vol. 23, no. 9, p. 093201, July 2014.

[14] X. Wang, S. Grist, J. Flueckiger, N. A. F. Jaeger, and L. Chrostowski, "Silicon photonic slot waveguide Bragg gratings and resonators," Optics Express, vol. 21, no. 16, pp. 19029-19039, August 2013.

[15] Q. Quan, P. B. Deotare, and M. Loncar, "Photonic crystal nanobeam cavity strongly coupled to the feeding waveguide," Applied Physics Letters, vol. 96, no. 20, pp. 203102-203102-3, May 2010.

[16] A. Biberman, M. J. Shaw, E. Timurdogan, J. B. Wright, and M. R. Watts, “Ultralow-Loss Silicon Ring Resonators.” Optics Letters, vol. 37, no. 20, pp. 4236–38, October 2012.

[17] S. M. Grist, S. A. Schmidt, J. Flueckiger, V. Donzella, W. Shi, S. Talebi Fard, J. T. Kirk, D. M. Ratner, K. C. Cheung, and L. Chrostowski, "Silicon photonic micro-disk resonators for label-free biosensing," Optics Express, vol. 21, no. 7, pp. 7994-8006, April 2013.

[18] T. Hu, P. Yu, C. Qiu, H. Qiu, F. Wang, M. Yang, X. Jiang, H. Yu, and J. Yang, "Tunable Fano resonances based on two-beam interference in microring resonator," Applied Physics Letters, vol. 102, no. 1, p. 011112, January 2013.

[19] F. Peng, Z. Wang, G. Yuan, L. Guan, and Z. Peng, "High-Sensitivity Refractive Index Sensing Based on Fano resonances in a Photonic Crystal Cavity-Coupled Microring Resonator," IEEE Photonics Journal, vol. 10, no. 2, p. 6600808, April 2018.

[20] G. Dong, Y. Wang, and X. Zhang, "High-contrast and low-power all-optical switch using Fano resonance based on a silicon nanobeam cavity," Optics Letters, vol. 43, no. 24, pp. 5977-5980, December 2018.

[21] U. Fano, "Effects of Configuration Interaction on Intensities and Phase Shifts," Physical Review, vol. 124, no. 6, pp. 1866–1878, December 1961.

[22] J. Göres, D. Goldhaber-Gordon, S. Heemeyer, M. A. Kastner, H. Shtrikman, D. Mahalu, and U. Meirav, "Fano resonances in electronic transport through a single-electron transistor," Physical Review B, vol. 62, no. 3, pp. 2188–2194, July 2000.

[23] D. D. Smith, H. Chang, K. A. Fuller, A. T. Rosenberger, and R. W. Boyd, "Coupled-resonator-induced transparency," Physical Review A, vol. 69, no. 6, p. 063804, June 2004.

[24] S. Chin, M. Gonzalez-Herraez, and L. Thévenaz, "Zero-gain slow & fast light propagation in an optical fiber," Optics Express 14, 10684 (2006).

[25] S. X. Chew, X. Yi, S. Song, L. Li, P. Bian, L. Nguyen, and R. A. Minasian, "Silicon-on-Insulator Dual-Ring Notch Filter for Optical Sideband Suppression and Spectral Characterization," Journal of Lightwave Technology 34, 4705–4714 (2016).

[26] L. Ma, O. Slattery, and X. Tang, "Optical quantum memory based on electromagnetically induced transparency," Journal of Optics 19, 043001 (2017).

[27] R. G. Beausoleil, W. J. Munro, D. A. Rodrigues, and T. P. Spiller, "Applications of electromagnetically induced transparency to quantum information processing," Journal of Modern Optics, vol. 51, no. 16-18, pp. 2441–2448, November 2004.

[28] X.-J. He, L. Wang, J.-M. Wang, X.-H. Tian, J.-X. Jiang, and Z.-X. Geng, "Electromagnetically induced transparency in planar complementary metamaterial for refractive index sensing applications," Journal of Physics D: Applied Physics 46, 365302 (2013).

[29] X. Zhou, L. Zhang, A. M. Armani, R. G. Beausoleil, A. E. Willner, and W. Pang, "Power enhancement and phase regimes in embedded microring resonators in analogy with electromagnetically induced transparency," Optics Express 21, 20179 (2013).

[30] K.-J. Boller, A. Imamoğlu, and S. E. Harris, "Observation of electromagnetically induced transparency," Physical Review Letters 66, 2593–2596 (1991).

[31] M. D. Lukin and A. Imamoğlu, "Controlling photons using electromagnetically induced transparency," Nature 413, 273–276 (2001).

[32] J. P. Marangos, "Electromagnetically induced transparency," Journal of Modern Optics 45, 471–503 (1998).

[33] A. B. Matsko, A. A. Savchenkov, D. Strekalov, V. S. Ilchenko, and L. Maleki, "Interference effects in lossy resonator chains," Journal of Modern Optics 51, 2515–2522 (2004).

[34] Q. Xu, S. Sandhu, M. L. Povinelli, J. Shakya, S. Fan, and M. Lipson, "Experimental Realization of an On-Chip All-Optical Analogue to Electromagnetically Induced Transparency," Physical Review Letters 96, 123901, (2006).

[35] A. Naweed, G. Farca, S. I. Shopova, and A. T. Rosenberger, "Induced transparency and absorption in coupled whispering-gallery microresonators," Physical Review A 71, 043804, (2005).

[36] Y. Yang, S. Saurabh, J. Ward, and S. N. Chormaic, "Coupled-mode-induced transparency in aerostatically tuned microbubble whispering-gallery resonators," Optics Letters 40, 1834 (2015).

[37] J. Pan, Y. Huo, S. Sandhu, N. Stuhrmann, M. L. Povinelli, J. S. Harris, M. M. Fejer, and S. Fan, "Tuning the coherent interaction in an on-chip photonic-crystal waveguide-resonator system," Applied Physics Letters 97, 101102 (2010).

[38] X. Yang, M. Yu, D.-L. Kwong, and C. W. Wong, "All-Optical Analog to Electromagnetically Induced Transparency in Multiple Coupled Photonic Crystal Cavities," Physical Review Letters 102, 173902 (2009).

[39] S. khazaee and N. Granpayeh, "Tunable multiple plasmon induced transparencies in parallel graphene sheets and its applications," Optics Communications 406, 199–204 (2018).

[40] P. Tassin, L. Zhang, R. Zhao, A. Jain, T. Koschny, and C. M. Soukoulis, "Electromagnetically Induced Transparency and Absorption in Metamaterials: The Radiating Two-Oscillator Model and Its Experimental Confirmation," Physical Review Letters 109, 187401 (2012).

[41] W. Bogaerts, P. De Heyn, T. Van Vaerenbergh, K. De Vos, S. Kumar Selvaraja, T. Claes, P. Dumon, P. Bienstman, D. Van Thourhout, and R. Baets, "Silicon microring resonators," Laser & Photonics Reviews, vol. 6, no. 1, pp. 47–73, January 2012.

[42] A. Morand, Y. Zhang, B. Martin, K. Phan Huy, D. Amans, P. Benech, J. Verbert, E. Hadji, and J.-M. Fédéli, "Ultra-compact microdisk resonator filters on SOI substrate," Optics Express, vol. 14, no. 26, pp. 12814-21, December 2006.

[43] G. Zhao, T. Zhao, H. Xiao, Z. Liu, G. Liu, J. Yang, Z. Ren, J. Bai, and Y. Tian, "Tunable Fano resonances based on microring resonator with feedback coupled waveguide," Optics Express, vol. 24, no. 18, pp. 20187-95, September 2016.

[44] Z. Zhang, G. I. Ng, T. Hu, H. Qiu, X. Guo, W. Wang, M. S. Rouifed, C. Liu, J. Sia, J. Zhou, C. G. Littlejohns, M. Nedeljkovic, G. T. Reed, and H. Wang, "Experimental Demonstration of Thermally Tunable Fano and EIT Resonances in Coupled Resonant System on SOI Platform," IEEE Photonics Journal, vol. 10, no. 3, p. 6601108, May 2018.

[45] Q. Huang, Z. Shu, G. Song, J. Chen, J. Xia, and J. Yu, "Electromagnetically induced transparency-like effect in a two-bus waveguides coupled microdisk resonator," Optics Express, vol. 22, no. 3, pp. 3219-3227, February 2014.

[46] S. Izadshenas, A. Zakery, and Z. Vafapour, "Tunable Slow Light in Graphene Metamaterial in a Broad Terahertz Range," Plasmonics, vol. 13, no. 1, pp. 63–70, February 2018.

[47] X. Sun, L. Zhou, J. Xie, Z. Zou, L. Lu, H. Zhu, X. Li, and J. Chen, "Tunable silicon Fabry–Perot comb filters formed by Sagnac loop mirrors," Optics Letters, vol. 38, no. 4, pp. 567-569, February 2013.

[48] L. Zhou, T. Ye, and J. Chen, "Coherent interference induced transparency in self-coupled optical waveguide-based resonators," Optics Letters, vol. 36, no. 1, pp. 13-15, January 2011.

[49] H. Tang, L. Zhou, J. Xie, L. Lu, and J. Chen, "Electromagnetically Induced Transparency in a Silicon Self-Coupled Optical Waveguide," Journal of Lightwave Technology, vol. 36, no. 11, pp. 2188–2195, June 2018.

[50] T. Yoshie, L. Tang, and S.-Y. Su, "Optical Microcavity: Sensing down to Single Molecules and Atoms," Sensors 11, 1972–1991 (2011).

[51] Lukas Chrostowski, Samantha Grist, Jonas Flueckiger, Wei Shi, Xu Wang, Eric Ouellet, Han Yun, Mitch Webb, Ben Nie, and Zhen Liang. Silicon photonic resonator sensors and devices. In SPIE LASE, pages 823620–823620. International Society for Optics and Photonics, 2012.

[52] Q. Liu, Y. Shin, J. S. Kee, K. W. Kim, S. R. Mohamed Rafei, A. P. Perera, X. Tu, G.-Q. Lo, E. Ricci, M. Colombel, E. Chiong, J. P. Thiery, and M. K. Park, "Mach–Zehnder interferometer (MZI) point-of-care system for rapid multiplexed detection of microRNAs in human urine specimens," Biosensors and Bioelectronics 71, 365–372 (2015).

[53] J.-W. Hoste, S. Werquin, T. Claes, and P. Bienstman, "Conformational analysis of proteins with a dual polarisation silicon microring," Optics Express 22, 2807 (2014).

[54] K. De Vos, I. Bartolozzi, E. Schacht, P. Bienstman, and R. Baets, "Silicon-on-Insulator microring resonator for sensitive and label-free biosensing," Optics Express 15, 7610 (2007).

[55] G. A. Rodriguez, S. Hu, and S. M. Weiss, "Porous silicon ring resonator for compact, high sensitivity biosensing applications," Optics Express 23, 7111 (2015).

[56] T. Claes, J. G. Molera, K. De Vos, E. Schacht, R. Baets, and P. Bienstman, "Label-Free Biosensing With a Slot-Waveguide-Based Ring Resonator in Silicon on Insulator," IEEE Photonics Journal 1, 197–204 (2009).

[57] S. TalebiFard, S. Schmidt, W. Shi, W. Wu, N. A. F. Jaeger, E. Kwok, D. M. Ratner, and L. Chrostowski, "Optimized sensitivity of Silicon-on-Insulator (SOI) strip waveguide resonator sensor," Biomedical Optics Express 8, 500 (2017).

[58] J. Flueckiger, S. Schmidt, V. Donzella, A. Sherwali, D. M. Ratner, L. Chrostowski, and K. C. Cheung, "Sub-wavelength grating for enhanced ring resonator biosensor," Optics Express 24, 15672 (2016).

[59] Lukas Chrostowski, Samantha Grist, Jonas Flueckiger, Wei Shi, Xu Wang, Eric Ouellet, Han Yun, Mitch Webb, Ben Nie, and Zhen Liang. Silicon photonic resonator sensors and devices. In SPIE LASE, pp. 823620–823620. International Society for Optics and Photonics, (2012).

[60] Maple Leaf Photonics. (2019, June 1). Available: http://mapleleafphotonics.com

[61] M. Caverley (2019, June 1). Python code. Available: https://siepic.ubc.ca/probestation

[62] PLC Connections. (2019, June 1). Available: www.plcconnections.com

[63] Y. Wang, X. Wang, J. Flueckiger, H. Yun, W. Shi, R. Bojko, N. A. F. Jaeger, and L. Chrostowski, "Focusing sub-wavelength grating couplers with low back reflections for rapid prototyping of silicon photonic circuits," Optics Express, vol. 22, no. 17, pp. 20652-20662, (2014).

[64] R. J. Bojko, J. Li, L. He, T. Baehr-Jones, M. Hochberg, and Y. Aida, "Electron beam lithography writing strategies for low loss, high confinement silicon optical waveguides," Journal of Vacuum Science & Technology B, Nanotechnology and Microelectronics: Materials, Processing, Measurement, and Phenomena vol. 29, no. 6, p. 06F309 November (2011).

[65] Applied Nanotools Inc. (2019, June 1). Available: https://www.appliednt.com/nanosoi/

[66] Genisys GmbH. (2019, June 1). Available: https://genisys-gmbh.com/beamer.html.

[67] J. Flueckiger, S. Schmidt, V. Donzella, A. Sherwali, D. M. Ratner, L. Chrostowski, and K. C. Cheung, "Sub-wavelength grating for enhanced ring resonator biosensor," Optics Express, vol. 24, no. 14, pp. 15672-86, July 2016.

[68] H. van de Stadt and J. M. Muller, "Multimirror Fabry–Perot interferometers," Journal of the Optical Society of America A 2, 1363 (1985).

[69] J. Martin and J. Capmany, "Transfer functions of double- and multiple-cavity Fabry–Perot filters driven by Lorentzian sources," Applied Optics 35, 7108 (1996).

[70] S. J. Hogeveen and H. van de Stadt, "Fabry-Perot interferometers with three mirrors," Applied Optics 25, 4181 (1986).

[71] Z. Zhang, M. Dainese, L. Wosinski, and M. Qiu, "Resonance-splitting and enhanced notch depth in SOI ring resonators with mutual mode coupling," Optics Express 16, 4621 (2008).

[72] W. Chen, H. Xiao, Z. Liu, X. Han, M. Liao, T. Zhao, and Y. Tian, "Experimental realization of mode-splitting resonance using microring resonator with a feedback coupled waveguide," Applied Physics Express 11, 092201 (2018).

[73] L. Zhang, M. Song, T. Wu, L. Zou, R. G. Beausoleil, and A. E. Willner, "Embedded ring resonators for microphotonic applications," Optics Letters 33, 1978 (2008).

[74] M. C. M. M. Souza, G. F. M. Rezende, L. A. M. Barea, A. A. G. von Zuben, G. S. Wiederhecker, and N. C. Frateschi, "Spectral engineering with coupled microcavities: active control of resonant mode-splitting," Optics Letters 40, 3332 (2015).

[75] H. Flayac, D. Gerace, and V. Savona, "An all-silicon single-photon source by unconventional photon blockade," Scientific Reports 5, 11223 (2015).

[76] Y. Sato, Y. Tanaka, J. Upham, Y. Takahashi, T. Asano, and S. Noda, "Strong coupling between distant photonic nanocavities and its dynamic control," Nature Photonics 6, 56–61 (2012).

[77] C. M. Campanella, M. Dunai, L. Calabrese, and C. E. Campanella, "Design guidelines for nanoparticle chemical sensors based on mode-splitting silicon-on-insulator planar microcavities," Journal of the Optical Society of America B 33, 2383 (2016).

[78] J. Wu, T. Moein, X. Xu, and D. J. Moss, "Advanced photonic filters based on cascaded Sagnac loop reflector resonators in silicon-on-insulator nanowires," APL Photonics 3, 046102 (2018).

[79] X. Sun, L. Zhou, J. Xie, Z. Zou, L. Lu, H. Zhu, X. Li, and J. Chen, "Tunable silicon Fabry–Perot comb filters formed by Sagnac loop mirrors," Optics Letters 38, 567 (2013).

[80] F. Xia, L. Sekaric, M. O'Boyle, and Y. Vlasov, "Coupled resonator optical waveguides based on silicon-on-insulator photonic wires," Applied Physics Letters 89, 041122 (2006).

[81] L. A. M. Barea, F. Vallini, P. F. Jarschel, and N. C. Frateschi, "Silicon technology compatible photonic molecules for compact optical signal processing," Applied Physics Letters 103, 201102 (2013).

[82] G. Cocorullo and I. Rendina, "Thermo-optical modulation at 1.5μm in silicon etalon," Electronics Letters 28, 83–85 (1992).

[83] R. L. Espinola, M. C. Tsai, J. T. Yardley, and R. M. Osgood, "Fast and low-power thermooptic switch on thin silicon-on-insulator," IEEE Photonics Technology Letters 15, 1366–1368 (2003).

[84] K. Padmaraju, J. Chan, L. Chen, M. Lipson, and K. Bergman, "Thermal stabilization of a microring modulator using feedback control," Optics Express 20, 27999 (2012).

[85] K. Padmaraju and K. Bergman, "Resolving the thermal challenges for silicon microring resonator devices," Nanophotonics 3, 269-281 (2014).

[86] H. Xu, M. Hafezi, J. Fan, J. M. Taylor, G. F. Strouse, and Z. Ahmed, "Ultra-sensitive chip-based photonic temperature sensor using ring resonator structures," Optics Express 22, 3098 (2014).

[87] P. Alipour, E. S. Hosseini, A. A. Eftekhar, B. Momeni, and A. Adibi, "Athermal performance in high-Q polymer-clad silicon microdisk resonators," Optics Letters 35, 3462 (2010).

[88] H.-T. Kim and M. Yu, "Cascaded ring resonator-based temperature sensor with simultaneously enhanced sensitivity and range," Optics Express 24, 9501 (2016).

[89] S. Chin, M. Gonzalez-Herraez, and L. Thévenaz, "Zero-gain slow & fast light propagation in an optical fiber," Optics Express 14, 10684 (2006).

[90] S. X. Chew, X. Yi, S. Song, L. Li, P. Bian, L. Nguyen, and R. A. Minasian, "Silicon-on-Insulator Dual-Ring Notch Filter for Optical Sideband Suppression and Spectral Characterization," Journal of Lightwave Technology 34, 4705–4714 (2016).

[91] L. Ma, O. Slattery, and X. Tang, "Optical quantum memory based on electromagnetically induced transparency," Journal of Optics 19, 043001 (2017).

[92] X.-J. He, L. Wang, J.-M. Wang, X.-H. Tian, J.-X. Jiang, and Z.-X. Geng, "Electromagnetically induced transparency in planar complementary metamaterial for refractive index sensing applications," Journal of Physics D: Applied Physics 46, 365302 (2013).

[93] X. Zhou, L. Zhang, A. M. Armani, R. G. Beausoleil, A. E. Willner, and W. Pang, "Power enhancement and phase regimes in embedded microring resonators in analogy with electromagnetically induced transparency," Optics Express 21, 20179 (2013).

[94] K.-J. Boller, A. Imamoğlu, and S. E. Harris, "Observation of electromagnetically induced transparency," Physical Review Letters 66, 2593–2596 (1991).

[95] M. D. Lukin and A. Imamoğlu, "Controlling photons using electromagnetically induced transparency," Nature 413, 273–276 (2001).

[96] J. P. Marangos, "Electromagnetically induced transparency," Journal of Modern Optics 45, 471–503 (1998).

[97] A. B. Matsko, A. A. Savchenkov, D. Strekalov, V. S. Ilchenko, and L. Maleki, "Interference effects in lossy resonator chains," Journal of Modern Optics 51, 2515–2522 (2004).

[98] Q. Xu, S. Sandhu, M. L. Povinelli, J. Shakya, S. Fan, and M. Lipson, "Experimental Realization of an On-Chip All-Optical Analogue to Electromagnetically Induced Transparency," Physical Review Letters 96, 123901, (2006).

[99] A. Naweed, G. Farca, S. I. Shopova, and A. T. Rosenberger, "Induced transparency and absorption in coupled whispering-gallery microresonators," Physical Review A 71, 043804, (2005).

[100] Y. Yang, S. Saurabh, J. Ward, and S. N. Chormaic, "Coupled-mode-induced transparency in aerostatically tuned microbubble whispering-gallery resonators," Optics Letters 40, 1834 (2015).

[101] J. Pan, Y. Huo, S. Sandhu, N. Stuhrmann, M. L. Povinelli, J. S. Harris, M. M. Fejer, and S. Fan, "Tuning the coherent interaction in an on-chip photonic-crystal waveguide-resonator system," Applied Physics Letters 97, 101102 (2010).

[102] X. Yang, M. Yu, D.-L. Kwong, and C. W. Wong, "All-Optical Analog to Electromagnetically Induced Transparency in Multiple Coupled Photonic Crystal Cavities," Physical Review Letters 102, 173902 (2009).

[103] P. Tassin, L. Zhang, R. Zhao, A. Jain, T. Koschny, and C. M. Soukoulis, "Electromagnetically Induced Transparency and Absorption in Metamaterials: The Radiating Two-Oscillator Model and Its Experimental Confirmation," Physical Review Letters 109, 187401 (2012).

[104] H. Tang, L. Zhou, J. Xie, L. Lu, and J. Chen, "Electromagnetically Induced Transparency in a Silicon Self-Coupled Optical Waveguide," Journal of Lightwave Technology 36, 2188–2195 (2018).

[105] Z. Zou, L. Zhou, X. Sun, J. Xie, H. Zhu, L. Lu, X. Li, and J. Chen, "Tunable two-stage self-coupled optical waveguide resonators," Optics Letters 38, 1215 (2013).

[106] C. B. Dağ, M. A. Anıl, and A. Serpengüzel, “Novel Distributed Feedback Lightwave Circuit Elements.” in Proceedings of the SPIE on Smart Photonic and Optoelectronic Integrated Circuits XVII, L. A. Eldada, E.-H. Lee, and S. He, Eds. 9366:93660A, (2015).

[107] C. B. Dağ, M. A. Anıl, and A. Serpengüzel, "Meandering Waveguide Distributed Feedback Lightwave Circuits," Journal of Lightwave Technology 33, 1691–1702 (2015).

[108] A. G. Rickman and G. T. Reed, "Silicon-on-insulator optical rib waveguides: loss, mode characteristics, bends and y-junctions," IEE Proceedings - Optoelectronics 141, no. 6, pp. 391–393, December 1994.

[109] S. Darmawan, L. Y. M. Tobing, and D. H. Zhang, “Experimental Demonstration of Coupled-Resonator-Induced-Transparency in Silicon-on-Insulator Based Ring-Bus-Ring Geometry,” Optics Express, vol. 19, no. 18, pp. 17813-17819, August 2011.

[110] M. Popovic, C. Manolatou, and M. Watts, “Coupling-Induced Resonance Frequency Shifts in Coupled Dielectric Multi-Cavity Filters,” Optics Express, vol. 14, no. 3, pp. 1208-1222, February 2006.

[111] C. B. Dağ, M. A. Anıl, and A. Serpengüzel, "Meandering Waveguide Distributed Feedback Lightwave Circuits," Journal of Lightwave Technology, vol. 33, no. 9, pp. 1691–1702, January 2015.

[112] J. Wu, T. Moein, X. Xu, and D. J. Moss, "Advanced photonic filters based on cascaded Sagnac loop reflector resonators in silicon-on-insulator nanowires," APL Photonics, vol. 3, no. 4, p. 046102, April 2018.

[113] Q. Li, T. Wang, Y. Su, M. Yan, and M. Qiu, "Coupled mode theory analysis of mode-splitting in coupled cavity system," Optics Express, vol. 18, no. 8, pp. 8367-82, April 2010.

[114] S. Darmawan, L. Y. M. Tobing, and D. H. Zhang, "Experimental Demonstration of Coupled-Resonator-Induced-Transparency in Silicon-on-Insulator Based Ring-Bus-Ring Geometry," Optics Express, vol. 19, no. 18, pp. 17813-17819, August 2011.

[115] M. Popovic, C. Manolatou, and M. Watts, "Coupling-Induced Resonance Frequency Shifts in Coupled Dielectric Multi-Cavity Filters," Optics Express, vol. 14, no. 3, pp. 1208-1222, February 2006.

[116] S. N. Bhatia and D. E. Ingber, "Microfluidic organs-on-chips," Nature Biotechnology 32, 760–772 (2014).

[117] K. Leosson and B. Agnarsson, "Integrated Biophotonics with CYTOP," Micromachines 3, 114–125 (2012).

[118] J. Flueckiger, "Enhancing the performance of silicon photonics biosensors," Ph.D. Thesis, University of British Columbia, 2017.

[119] D. Kim and A. E. Herr, "Protein immobilization techniques for microfluidic assays," Biomicrofluidics 7, 041501 (2013).

[120] J. Vörös, "The Density and Refractive Index of Adsorbing Protein Layers," Biophysical Journal 87, 553–561 (2004).

[121] K. Nakanishi, T. Sakiyama, Y. Kumada, K. Imamura, and H. Imanaka, "Recent Advances in Controlled Immobilization of Proteins onto the Surface of the Solid Substrate and Its Possible Application to Proteomics," Current Proteomics 5, 161–175 (2008).

[122] M. C. Coen, R. Lehmann, P. Gröning, M. Bielmann, C. Galli, and L. Schlapbach, "Adsorption and Bioactivity of Protein A on Silicon Surfaces Studied by AFM and XPS," Journal of Colloid and Interface Science 233, 180–189 (2001).

[123] J. Shang, F. Cheng, M. Dubey, J. M. Kaplan, M. Rawal, X. Jiang, D. S. Newburg, P. A. Sullivan, R. B. Andrade, and D. M. Ratner, "An Organophosphonate Strategy for Functionalizing Silicon Photonic Biosensors," Langmuir 28, 3338–3344 (2012).